1.0 Introduction

This report describes the GE Vallecitos Nuclear Center Libra Finite Element Analysis Program verification. The Libra verification consists of three items: the original verification report, Reference 1, the verification program Libra_Verification.Exe and associated verification problem files, and this report. A Libra verification can be performed at any time by executing the program Libra_Verification. This program executes all of the verification problem files, and tabulates the results in the text file Verificatian.txt. The Libra_Verification program and problem files are installed on the Libra Application Directory as part of the Libra installation. The output file, Verification.txt, is also located on the Libra Application Directory.

The original verification report, Reference 1, documents a number of the verification problems, including all of the thermal verification problems. The thermal verification problems in Reference 1 were updated in Reference la. This report encompasses both References 1 and la. All of the verification problems executed by Libra_Verification are described in this report, however the theoretical solutions of the original verification problems are given in Reference 1, and are not contained in this report. The theoretical solutions for all verification problems not in Reference 1 are given in this report.

The verification program, Libra_Verification, executes 24 problem files. These problems cover a wide spectrum of Libra capabilities, and include all significant types of analyses and elements used at the GE Vallecitos facility. The program compiles the results in two ways. For each verification problem, the program presents a table comparing the Libra solution values with the theoretical values. In addition, since the Libra and theoretical values are not necessarily the same, the program generates a table comparing the current verification results with the expected values. The expected values are not theoretical values, but Libra values from a certified verification.

The structure of the Libra program is such that no permanent executable exists. Rather, a new executable is formed whenever the solution or element type changes from the preceding application. To establish the program status, the verification program generates a list of all of Libra subroutines on the file Verification.txt. The verification status of any Libra subroutine can then be established comparing it with the listing in Verification.txt.

This report is structured around the verification problems. Each problem is presented in a separate section. Each section specifies the problem input data file, and the Libra solution and element types used in the problem. In addition, each section contains a description of the problem, a description of the Libra model, and the theoretical or comparative solution.

Additional Problem

Main23, Element 10. Sample problem in Last-A-Foam Manual, "Rigid Polyurethane Foam for Impact and Thermal Protection," pgs. 2-3. 30 ft drop of 700 lb cylinder onto 5 in thick Last-A-Foam disk. Quarter disk modeled by STIF10 elements. From curve on pg. 3, for 3712 foam,

g = impact force / weight = 2820*78.5/700 = 316.2

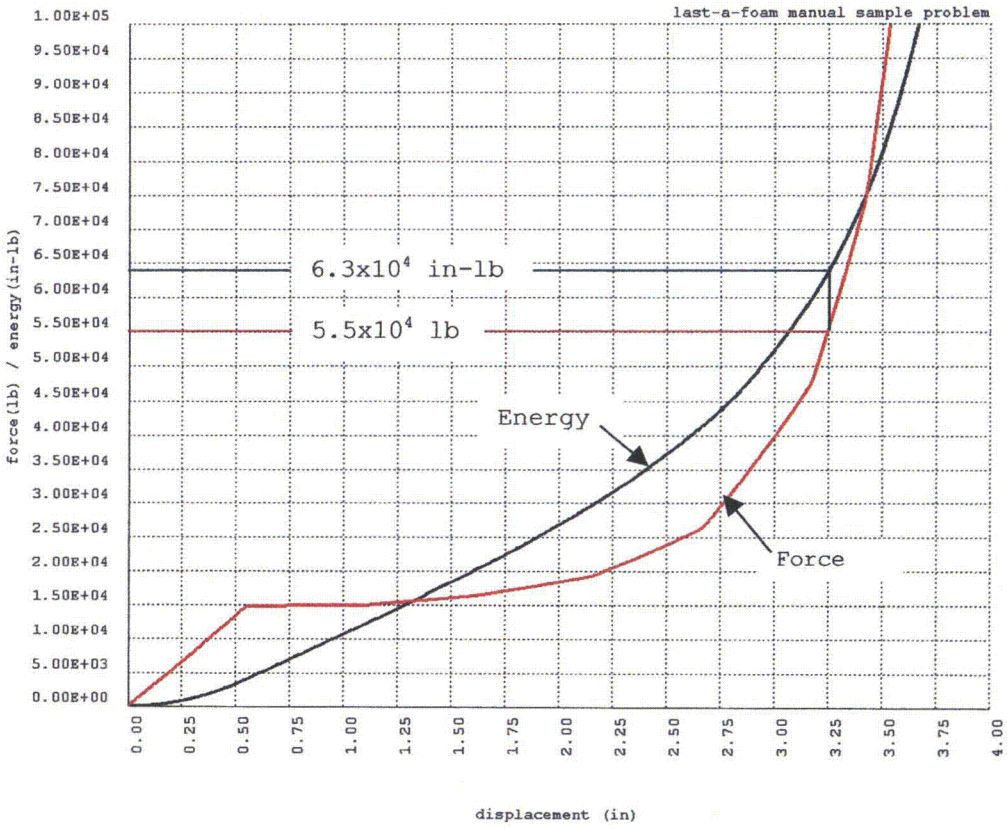

From Libra force and energy curves for 1/4 model,

U = 700x30x12/4 = $6.3x10^4$ in-lb
P = $5.5x10^4$ lb.
g = $4x5.5x10^4/700$ = 314.3

Difference = 100x(316.2-314.3)/314.3 = 0.6%

Problem 1

Input Data File: VER_PROB.1

Libra Routines: Solution Type12, Elements 32 & 34

Description of Problem

A 0.03 m long carbon resistor is comprised of a 0.001 m radius graphite core, and a micanite thermal conductor with inside radius 0.001m and outside radius .00588 m. 0.4 watt heat through conductor is convected to surrounding air at 310° K. Determine steady-state temperature at outside of graphite core.

$k(\text{graphite}) = 0.1\ W/m^2/K°$
$k(\text{conductor}) = 0.1\ W/m^2/K°$
$h(\text{air}) = 17.0 W/m/\ K°$
$Q = 0.4\ W$

Description of Model

Axisymmetric model of both resistor and conductor. Heat input through resistor elements.

Theoretical Solution

The theoretical solution is presented in Reference 1.

Problem 2

Input Data File: VER_PROB.2

Libra Routines: Solution Type 12, Elements 32 & 34

Description of Problem

A 0.03 m long carbon resistor is comprised of a 0.001 m radius graphite core, and a micanite thermal conductor with inside radius 0.001m and outside radius .00588 m. 0.4 watt heat through conductor is convected to surrounding air at 310° K. Determine steady-state temperature at outside of graphite core.

$k(\text{graphite}) = 0.1\ W/m^2/K°$
$k(\text{conductor}) = 0.1\ W/m^2/K°$
$h(\text{air})=17.0 W/m/K°$
$Q=0.4\ W$

Description of Model

Axisymmetric model of conductor only. Heat input by convection at inside of conductor.

Theoretical Solution

The theoretical solution is presented in Reference 1.

Problem 3

Input Data File: VER_PROB.3

Libra Routines: Solution Type 12, Elements 32 & 34

Description of Problem

A 0.03 m long carbon resistor is comprised of a 0.001 m radius graphite core, and a micanite thema1 conductor with inside radius 0.001m and outside radius .00588 m. 0.4 watt heat through conductor is convected to surrounding air at 310° K. Determine steady-state temperature at outside of graphite core.

$$k(\text{graphite}) = 0.1\ W/m^2/K°$$
$$k(\text{conductor}) = 0.1\ W/m^2/K°$$
$$h(\text{air})=17.0W/m/\ K°$$
$$Q=0.4\ W$$

Description of Model

Axisymmetric model of conductor only. Heat input by thermal loads at inside of conductor.

Theoretical Solution

The theoretical solution is presented in Reference 1.

Problem 4

Input Data File: VER_PROB.4

Libra Routines: Solution Type 12, Elements 32 & 34

Description of Problem

A 0.03 m long carbon resistor is comprised of a thermal conductor with inside radius 0.001m and outside radius .00588 m. 0.4 watt heat through conductor is convected to surrounding air at 310° K. Determine steady-state temperature at inside of conductor.

$$k \text{ (conductor)} = 0.1 \text{ W/m}^2/\text{K}^\circ$$
$$h(\text{air}) = 17.0 \text{W/m/ K}^\circ$$
$$Q = 0.4 \text{ W}$$

Description of Model

Axisymmetric model of resistor. Heat applied to elements. Convection elements at surface.

Theoretical Solution

The theoretical solution is presented in Reference 1.

Problem 5

Input Data File: VER_PROB.5

Libra Routines: Solution Type 12, Elements 32 & 34

Description of Problem

Determine transient response of 1/32 in copper wire at 300°F immerse in water at 100°

$$h_{water} = 15.0 \text{ Btu/hr/ft}^2/°F$$
$$k_{copper} = 216.0 \text{ Btu/hr-in-°F}$$
$$\rho_{copper} = 0.091 \text{ lb/in}^3$$
$$c_{copper} = 558.0 \text{ Btu/lbm-°F}$$

Description of Model

Axisymmetric model of wire, with convection elements at surface.

Theoretical Solution

The theoretical solution is presented in Reference 1.

Problem 6

Input Data File: VER_PROB.6

Libra Routines: Solution Type 12, Elements 32 & 34

Description of Problem

Determine transient response of 1/32 in copper wire at 300°F immerse in air at 100°

$$h_{air} = 2.0 \text{ Btu/hr/ft}^2/°F$$
$$k_{copper} = 216.0 \text{ Btu/hr-in-°F}$$
$$\rho_{copper} = 0.091 \text{ lb/in}^3$$
$$c_{copper} = 558.0 \text{ Btu/lbm-°F}$$

Description of Model

Axisymmetric model of wire, with convection elements at surface.

Theoretical Solution

The theoretical solution is presented in Reference 1.

Problem 7

Input Data File: VER_PROB.7

Libra Routines: Solution Type 12, Elements 32 & 34

Description of Problem

Concrete wall initially at 100° F has one side exposed to hot gas at 1600° and other side insulated. Find temperature distribution through wall when temperature at insulated side reaches 500°F. Heat transfer coefficient at xposed side is, h = 5.0 Btu/hr/ft^2/°F.

Description of Model

Two dimensional model of wall, with a convective element at one surface.

Theoretical Solution

The theoretical solution is presented in Reference 1.

Problem 8

Input Data File: VER_PROB.8

Libra Routines: Solution Type 12, Elements 32 & 34

Description of Problem

Steady-state heat conduction. A furnace has a two layer wall, with k_1=0.8 Btu/hr/ft^2/°F and k_2=0.8 Btu/hr/ft^2/°F. The temperature inside the furnace is 3000°F. The surface conduction at the outside wall is h = 2.0 Btu/hr/ft^2/°F. Find steady-state temperatures through wall.

Description of Model

Two dimensional model of wall, with a convective element at one surface.

Theoretical Solution

The theoretical solution is presented in Reference 1.

Problem 9

Input Data File: VER_PROB.9

Libra Routines: Solution Type 1, Element 9

Description of Problem

Long cylinder under internal pressure. Determine radial displacement and hoop stress.

Description of Model

Axisymmetric model of cylinder using 8-node quads.

Theoretical Solution

The theoretical solution is presented in Reference 1.

Problem 10

Input Data File: VER_PROB.10

Libra Routines: Solution Type 1, Element 9

Description of Problem

Long, cylindrical tube with axisymmetric, radial pinch at center. Find maximum longitudinal bending stress at pinch.

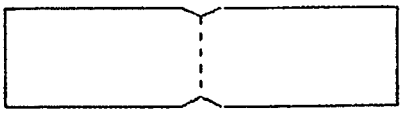

Description of Model

Axisymmetric model of cylinder using 8-node quads. Half of structure (and load) modeled with symmetric boundary conditions in longitudinal direction.

Theoretical Solution

The theoretical solution is presented in Reference 1.

Problem 11

Input Data File: VER_PROB.11

Libra Routines: Solution Type 23, Element 3

Description of Problem

Collapse of a cylindrical ring, 1 in long, 2.485 in outside diameter, 0.185 in wall thickness. Cylinder compressed between two unyielding surfaces.

$$E = 29.5 \times 10^6 \text{ psi}$$
$$E_p = 1.0 \times 10^6 \text{ psi}$$
$$v = 0.3$$
$$\sigma_y = 45000 \text{ psi}$$

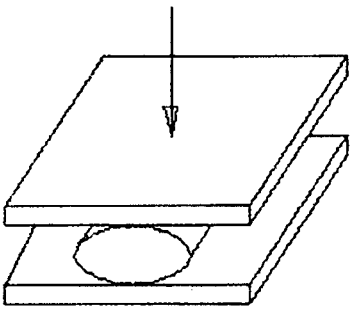

Description of Model

3D model composed of triangular shell elements. Half of cylinder modeled with symmetric boundary conditions.

Theoretical Solution

No theoretical solution is available for this problem. FEA solution is checked against test results given in Reference 1.

Problem 12

Input Data File: VER_PROB.12

Libra Routines: Solution Type 8, Element 16

Description of Problem

Elastic bending of a 10 in radius, cantilever tube, 1 in wall thickness, 200 in long with a 100 lb concentrated load at free end. Find deflection at load and stress 3 in from fixed end.

$E = 28.0 \times 10^6$ psi
$r = 10.0$ in
$t = 1.0$ in
$L = 100.0$ in

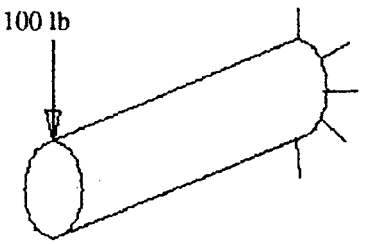

Description of Model

Tube bending is analyzed as an axisymmetric structure with nonsymmetric loading. 8-node, solid elements are used to model the tube, and only the first cosine mode used in the analysis. In this analysis, the load at node i for mode n is given by,

$$P_i = \int_0^{360} p_i(\theta) \cdot \cos(n\theta) \cdot r d\theta$$

where $p_i(\theta)$ is the circumferential load at node I. For a concentrated load Q at $\theta = 0$, and Δ_0 the Dirac-delta function at $\theta = 0$,

$$P_i = \int_0^{360} Q \cdot \Delta_0 \cdot \cos(n\theta) \cdot r d\theta = Q$$

Problem 12

Input Data File: VER_PROB.12

Libra Routines: Solution Type 8, Element 16

Description of Problem

Elastic bending of a 10 in radius, cantilever tube, 1 in wall thickness, 200 in long with a 100 lb concentrated load at free end. Find deflection at load and stress 3 in from fixed end.

$$E = 28.0 \times 10^6 \text{ psi}$$
$$r = 10.0 \text{ in}$$
$$t = 1.0 \text{ in}$$
$$L = 100.0 \text{ in}$$

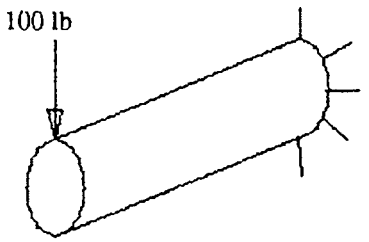

Description of Model

Tube bending is analyzed as an axisymmetric structure with nonsymmetric loading. 8-node, solid elements are used to model the tube, and only the first cosine mode used in the analysis. In this analysis, the load at node i for mode n is given by,

$$P_i = \int_0^{360} p_i(\theta) \cdot \cos(n\theta) \cdot r d\theta$$

where $p_i(\theta)$ is the circumferential load at node I. For a concentrated load Q at $\theta = 0$, and Δ_0 the Dirac-delta function at $\theta = 0$,

$$P_i = \int_0^{360} Q \cdot \Delta_0 \cdot \cos(n\theta) \cdot r d\theta = Q$$

Problem 12 – Cont'd

Theoretical Solution

Assuming the deflection shear correction for a cylindrical cross-section is the same as for a rectangle, from Reference 2, pg. 175, and Reference 3, Page 72, Table I, Case 11,

$$\delta = (P \cdot L^3 / 3EI) \cdot (1 + 0.98 \cdot D^2/L^2)$$

$$I = \pi \cdot r^3 \cdot t = 3141.59$$

$$P = 1000 \text{ lb}$$

$$L = 200 \text{ in}$$

$$E = 28.0 \text{ psi}$$

$$r = 10.0 \text{ in}$$

$$\delta = 0.030315 \cdot 1.01 = 0.030618 \text{ in}$$

$$\sigma = M \cdot c / I = 1000 \cdot 197 \cdot 10 / 3141.59 = 627.07 \text{ psi}$$

Problem 13

Input Data File: VER_PROB.13

Libra Routines: Solution Type 1, Element 7

Description of Problem

Elastic deflection of a 5 in radius, 0.025 in wall tickness tube, 50 in long by a distributed radial load of 15.9 lb/in (total load 500 lb). Determine deflection and hoop stress under load.

$$E = 28.0 \times 10^6 \text{ psi}$$
$$\nu = 0.3$$
$$r = 5.0$$
$$t = 0.025$$
$$p = 15.916 \text{ lb/in}$$

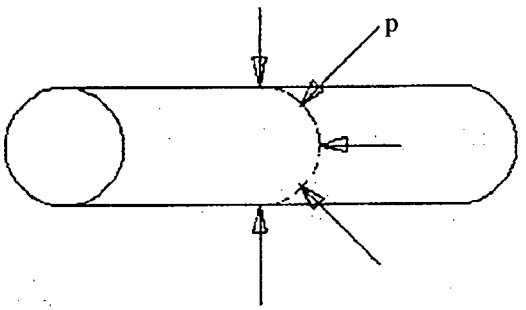

Description of Model

Tube bending is analyzed as an axisymmetric structure with symmetric loading. 2-node, shell elements are used to model the tube. In this analysis, the load at node i is given by,

$$P_i = \int_0^{360} p_i(\theta) \cdot r d\theta$$

Half of structure (and load) is modeled with symmetric boundary conditions.

Problem 13 – Cont'd

Theoretical Solution

The solution is given in Reference 3, pg.170.

$$\lambda = \sqrt[4]{3(1-\nu^2) / r^2 \cdot t^2} = 3.63538 \text{ in}$$
$$\delta = p \cdot r^2 \cdot \lambda / 2E \cdot t = 0.0010333$$
$$\sigma_H = p \cdot r \cdot \lambda / 2t = 5786.4 \text{ psi}$$

Problem 14

Input Data File: VER_PROB.14

Libra Routines: Solution Type 2, Element 9

Description of Problem

Inelastic deflection of a thick, cylindrical shell under internal pressure. Determine deflection at inside of cylinder for 16 dN/mm^2 and 18 dN/mm^2.

$E = 2.1 \times 10^4$ dN/mm^2
$\nu = 0.3$
$E_p = 0.0$
$\sigma_y = 24.0$ dN/mm^2
r(inside) = 100.0 mm
r(outside) = 200.0 mm

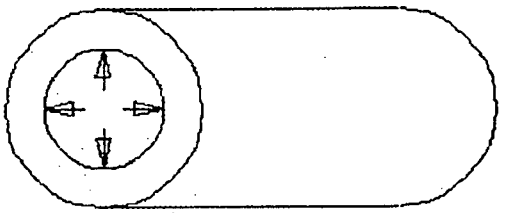

Description of Model

Cylinder modeled with 8-node plane strain elements. 90° cylinder segment modeled with symmetry boundary conditions at both ends.

Theoretical Solution

A solution for this problem is given in Reference 4, pgs.262-263 in graphic form. From Figure 7.12, pg. 262,

for p= 16 dN/mm^2, $\delta = 0.185$ mm
for p= 18 dN/mm^2, $\delta = 0.265$ mm

Problem 15

Input Data File: VER_PROB.15

Libra Routines: Solution Type 9, Element 9

Description of Problem

Elastic response of a spherical cap shell with simple supports under instantaneously applied external pressure. Determine the maximum and minimum deflections, and times of occurrence during period 0 - 0.0007 sec.

$$E = 10.5 \times 10^6 \text{ psi}$$
$$\nu = 0.3$$
$$\rho = 2.45 \times 10^{-4} \text{ lb-sec}^2/\text{in}^4$$
$$r(\text{inside}) = 22.27 \text{ in}$$
$$t = 0.41 \text{ in}$$
$$\alpha = 26.67°$$
$$p = 600 \text{ psi}$$

Description of Model

Spherical cap modeled with 8-node axisymmetric elements.

Theoretical Solution

A solution for this problem is given in Reference 4, pgs. 421-422, in graphic form. From Figure 10.4a, pg. 422,

$$@\ t = 0.00037 \text{ sec}, \quad \delta = 0.090 \text{ sec}$$
$$@\ t = 0.00055 \text{ sec}, \quad \delta = -0.050 \text{ sec}$$

Problem 16

Input Data File: VER_PROB.16

Libra Routines: Solution Type 4, Element 9

Description of Problem

Find fundamental period of a spherical cap shell simply-supported at base.

$E = 10.5 \times 10^6$ psi
$\nu = 0.3$
$\rho = 2.45 \times 10^{-4}$ lb-sec^2/in^4
r(inside) = 22.27 in
t = 0.41 in
$\alpha = 26.67°$

Description of Model

Spherical cap modeled with 8-node axisymmetric elements. Eigen pairs determined by the Lanzcos method.

Theoretical Solution

The first period is given in Reference 4, pg. 421,

$$T = 0.55 \times 10^{-3} \text{ sec}$$

Problem 17

Input Data File: VER_PROB.17

Libra Routines: Solution Type 2, Element 3

Description of Problem

Inelastic bending of an elastic - perfectly plastic, simply-supported, square plate under uniform lateral pressure. Find load corresponding to a displacement of 0.06 in at center of plate.

$$E = 10.92 \times 10^6 \text{ psi}$$
$$\nu = 0.3$$
$$E_p = 0.0$$
$$\sigma_y = 1600.0 \text{ psi}$$
$$L = 10.0 \text{ in}$$

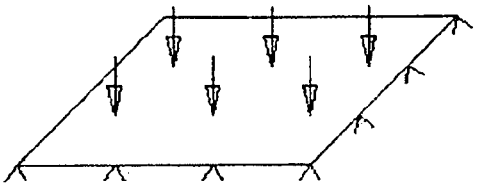

Description of Model

Plate modeled with triangular shell elements. Solution interpolated from displacements at two load steps.

Theoretical Solution

A solution for this problem is given in Reference 4, pgs. 370-371 in graphic form. From Figure 9.8, pg. 371,

$$D = E \cdot t^3 / 12(1-\nu^2) = 1000 \text{ psi}$$
$$M_p = \sigma_y \cdot t^2/4 = 4.0 \text{ in-lb}$$
$$w = 0.06 \text{ in}$$
$$100 \cdot w \cdot D/M_p \cdot L^2 = 15$$

From Figure 9.8: $q \cdot L^2/M_p = 22.5$, $q = 0.90$ psi

Problem 18

Input Data File: VER_PROB.18

Libra Routines: Solution Type 2, Element 13

Description of Problem

Inelastic bending of an elastic - perfectly plastic, simply-supported, square plate under uniform lateral pressure. Find load corresponding to a displacement of 0.06 in at center of plate.

$$E = 10.92 \times 10^6 \text{ psi}$$
$$\nu = 0.3$$
$$E_p = 0.0$$
$$\sigma_y = 1600.0 \text{ psi}$$
$$L = 10.0 \text{ in}$$

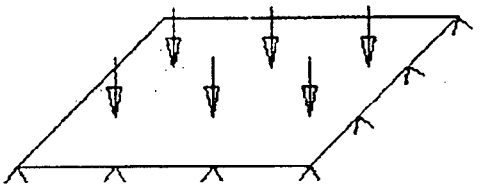

Description of Model

Plate modeled with quad shell elements. Solution interpolated from displacements at two load steps.

Theoretical Solution

A solution for this problem is given in Reference 4, pgs. 370-371 in graphic form. From Figure 9.8, pg. 371,

$$D = E \cdot t^3 / 12(1-\nu^2) = 1000 \text{ psi}$$
$$M_p = \sigma_y \cdot t^2/4 = 4.0 \text{ in-lb}$$
$$w = 0.06 \text{ in}$$
$$100 \cdot w \cdot D/M_p \cdot L^2 = 15$$

from Figure 9.8: $q \cdot L^2/M_p = 22.5$ $q = 0.90$ psi

Problem 19

Input Data File: VER_PROB.19

Libra Routines: Solution Type 5, Element 4

Description of Problem

Modal analysis of cantilever steel beam, S-5x10, 20 ft long, 50 lb/ft weight. Determine first three frequencies.

$$E = 28.0 \times 10^6 \text{ psi}$$
$$L = 240.0 \text{ in}$$
$$I_{zz} = 12.3 \text{ in}^4$$
$$I_{yy} = 1.22 \text{ in}^4$$
$$J = 0.114 \text{ in}^4$$
$$A = 2.94 \text{ in}^2$$
$$w = 50.0 \text{ lb/ft}$$
$$\rho = 50.0 / (12 \cdot 2.94 \cdot 386.4) = 0.0108 \text{ lb-sec}^2/\text{in}$$

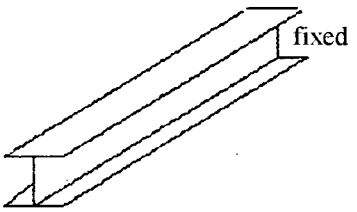

Description of Model

Beam modeled with 20 STIF4 elements. Z-displacements fixed along entire beam. Eigen-pairs determined by Sub-space iteration.

Theoretical Solution

From Reference 5, pg. 313, Figure E18-2,

$$\omega_1 = (1.875)^2 \cdot \sqrt{EI / \rho L^4} = 10.899 \text{ rad/sec}$$

$$\omega_2 = (4.694)^2 \cdot \sqrt{EI / \rho L^4} = 68.020 \text{ rad/sec}$$

$$\omega_3 = (7.855)^2 \cdot \sqrt{EI / \rho L^4} = 191.29 \text{ rad/sec}$$

Problem 20

Input Data File: VER_PROB.20

Libra Routines: Solution Type 3, Element 3

Description of Problem

Modal analysis of thin, square plate, two adjacent edges fixed, other two edges free. Determine first three frequencies.

$$E = 28.0 \times 10^6 \text{ psi}$$
$$\nu = 0.3$$
$$t = 0.025 \text{ in}$$
$$D = E \cdot t^3 / 12(1-\nu^2) = 40.064 \text{ in-lb}$$
$$L = 10.0 \text{ in}$$
$$\rho = 0.000725 \text{ lb-sec}^2/\text{in}$$

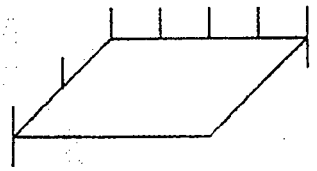

Description of Model

Beam modeled with triangular shell elements. Eigen-pairs determined by vector iteration.

Theoretical Solution

From Reference 6, pg. 61-23, Table 61.3,

$$\omega_1 = 6.96 \cdot \sqrt{D/\rho L^4} = 16.45 \text{ hz}$$

$$\omega_2 = 24.1 \cdot \sqrt{D/\rho L^4} = 56.65 \text{ hz}$$

$$\omega_3 = 26.8 \cdot \sqrt{D/\rho L^4} = 63.00 \text{ hz}$$

Problem 21

Input Data File: VER_PROB.21

Libra Routines: Solution Type 2, Elements 1 & 8

Description of Problem

Determine contact force between a steel sphere and the bottom flat surface of a steel cylinder due to a displacement at the top of the cylinder. The cylinder radius is 0.0060084 in, and height is 0.006 in. The sphere radius is 0.125 in. The specified displacement is 5.0×10^{-5} in, $E = 28.0 \times 10^{6}$ psi and $\nu = 0.3$ for both cylinder and sphere.

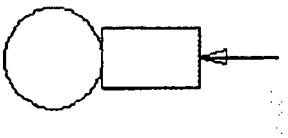

Description of Model

The cylinder and sphere are modeled separately with STIF8 axisymmetric elements, and are connected with gap spring elements. In this way, the contact area between the cylinder and sphere is determined in the solution. A special node and element generator is used to model the sphere in order to assure proper alignment between the nodes on the cylinder and sphere.

Theoretical Solution

This problem is a form of the Hertz contact problem. A theoretical solution is given in Reference 7, on pg. 376. Solving equation 222 for P,

$$\delta = 1.23 \cdot \sqrt[3]{P^2/E^2 \cdot R}, \quad P = E \cdot \sqrt{R \cdot (\delta/1.23)^3}$$

$E = 28.0 \times 10^{6}$ psi
$R = 0.125$ in,
$\delta = 5.0 \times 10^{-5}$ in,
$P = 2.5657$ lb.

Problem 22

Input Data File: VER_PROB.22

Libra Routines: Solution Type 11, Element 13

Description of Problem

Elastic buckling of thin, square plate under uniform edge compression load, p_0. Plate simply-supported on three sides, free on forth side.

$$E = 28 \cdot 10^6 \text{ psi}$$
$$\nu = 0.25$$
$$L = 10.0 \text{ in}$$
$$t = 0.025 \text{ in}$$
$$p_0 = 2.5 \text{ lb/in}$$

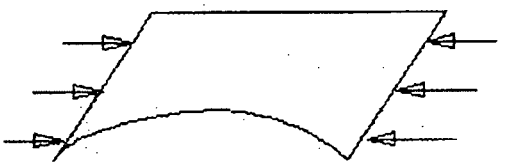

Description of Model

The plate is modeled by quad shell element. The entire plate is modeled with equal and opposite compression load along edges x=0, and x=10. Edges x=0, x=10, and y=0 are fixed in z-direction, edge y=10 is free. The Libra solution gives the problem eigenvalue, λ, and the buckling load is given by, $\sigma_{cr} = \lambda \cdot p_0 / t$.

Theoretical Solution

The theoretical solution for this problem is given in Reference 8, pgs. 360-362. From Equation (j) and Table 9-2 on page 362,

$$\sigma_{cr} = k \cdot \pi^2 \cdot D / b^2 \cdot t$$
$$k = 1.440 \text{ (a/b = 1)}$$
$$D = E \cdot t^3 / (1-\nu^2) = 3.8382 \text{ lb-in}$$
$$b = 10.0 \text{ in}$$
$$t = 0.025 \text{ in}$$
$$\sigma_{cr} = 221.0 \text{ psi}$$

Problem 23

Input Data Files: VER_PROB.23a, VER_PROB.23

Libra Routines: Solution Types 3 &14, Element 1

Description of Problem

RMS response of a two degree of freedom, spring-mass system to a PSD acceleration spectra. Problem given in Reference 9. Determine the 1σ, RMS force at the base.

$m_1 = 2.0$ lb
$k_1 = 50000$ lb/in
$m_2 = 1.0$ lb
$k_2 = 180000$ lb
@ 10 hz, $G^2/hz = 0.020$
@ 100 hz, $G^2/hz = 0.200$
@ 300 hz $G^2/hz = 0.200$
@ 2000 hz, $G^2/hz = 0.005$

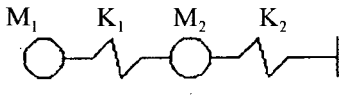

Description of Model

The Libra model consists of three nodes, and two spring elements in series. The mass is specified for nodes 1 and 2, and node 3 is fixed. The two system modes are determined using MAIN3 with the file VER_PROB.23a. The combined response is determined using MAIN14 with the file VER_PROB.23.

Modal damping values, ξ, used in the combined response solution are determined from the problem data in Reference 9, pgs 53-54, and the approximation for the maximum complex frequency response given in Reference 10, pg. 44, Equation 2-17.

$$Q = 1/2\xi$$
$Q_1 = 28.8$ g, $\xi_1 = 0.01736$
$Q_2 = 43.2$ g, $\xi_2 = 0.01157$

Theoretical Solution

From Reference 9, pg. 56b, $P_{rms} = 109.3$ lb

Problem 24

Input Data File: VER_PROB.24

Libra Routines: Solution Type 19, Element 9

Description of Problem

Determine the viscoplastic deflection of a thick, cylindrical shell under internal pressure. Find the radial deflection at inside of cylinder after 1, 2, 3, 5 and 7 days. The shell behavior is that of a Maxwell fluid with n = 0, and fluidity parameter γ=0.001/day.

$E = 2.1 \times 10^4$ dN/mm^2
$\nu = 0.3$
$E_p = 0.0$
$\sigma_y = 24.0$ dN/mm^2
$p_0 = 14$ dN/mm^2
r(inside) = 100.0 mm
r(outside) = 200.0 mm

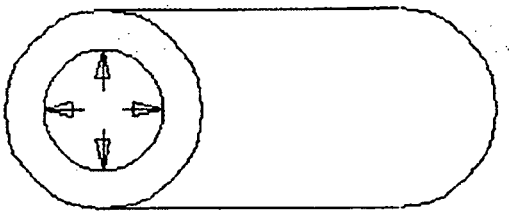

Description of Model

Cylinder modeled with 8-node plane strain elements. 90° cylinder segment modeled with symmetry boundary conditions at both ends.

Theoretical Solution

A solution for this problem is given in Reference 4, pgs.312-313 in graphic form. From Figure 8.11, pg. 313,

@ 1 day, $\delta = 0.132$ mm
@ 2 days, $\delta = 0.135$ mm
@ 3 days, $\delta = 0.137$ mm
@ 5 days, $\delta = 0.139$ mm
@ 7 days, $\delta = 0.140$ mm

Additional Problem

Main23, Element 10. Sample problem in Last-A-Foam Manual, "Rigid Polyurethane Foam for Impact and Thermal Protection", pgs. 2-3. 30 ft drop of 700 lb cylinder onto 5 in thick Last-A-Foam disk. Quarter disk modeled by STIF10 elements. From curve on pg. 3, for 3712 foam,

g = impact force / weight = 2820*78.5/700 = 316.2

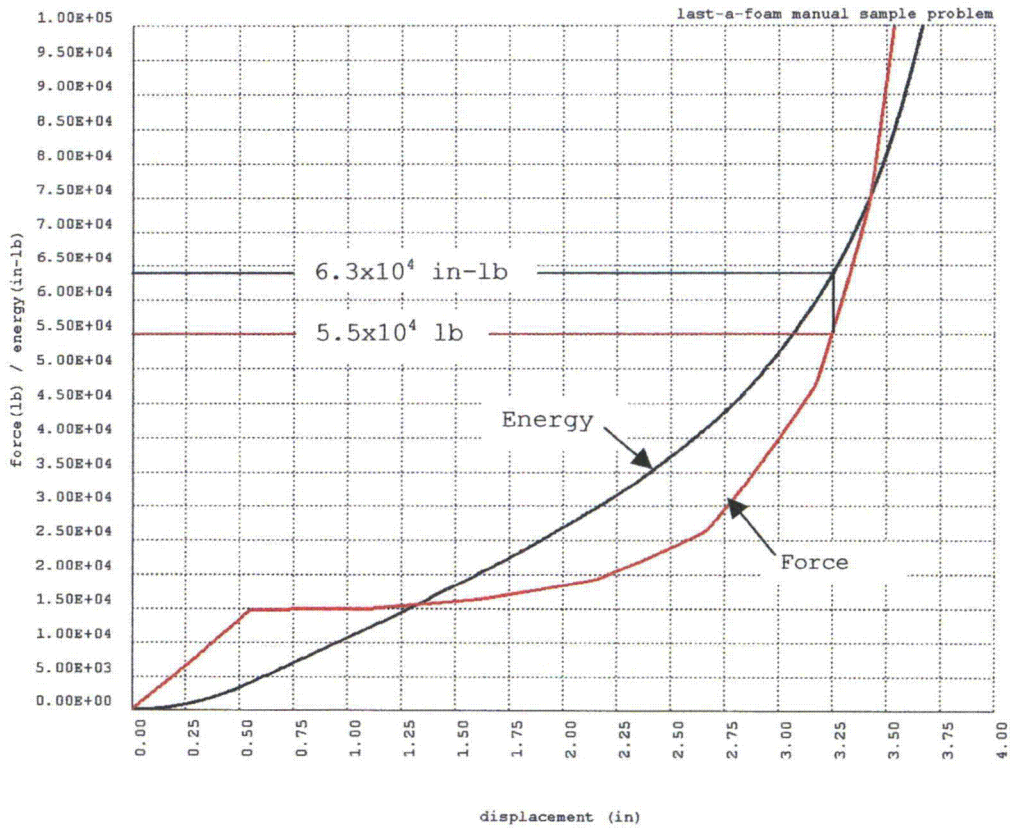

From Libra force and energy curves for 1/4 model,

$U = 700x30x12/4 = 6.3x10^4$ in-lb
$P = 5.5x10^4$ lb.
$g = 4x5.5x10^4/700 = 314.3$

Difference = 100x(316.2-314.3)/314.3 = 0.6%

References

1. Libra Verification Problems, GE Nuclear, Vallecitos, 1993.
1a. Update of Libra Thermal Verification Problems, GE Nuclear, Vallecitos, June, 2000.
2. S. Timoshenko, Strength of Materials, Part I, 3rd Edition, McGraw-Hill, 1955.
3. R. J. Roark, Formulas for Stress and Strain, 3rd Edition, 1954.
4. D. Owen, E. Hinton, Finite Elements in Plasticity, Pineridge Press, 1980.
5. R. W. Clough, J. Penzien, Dynamics of Structures, McGraw-Hill, 1975.
6. W. Flugge (Editor), Handbook of Engineering Mechanics, McGraw-Hill, 1962.
7. S. Timoshenko, J Goodier, Theory of Elasticity, 2nd Edition, McGraw-Hill, 1951.
8. S. Timoshenko, J. Gere, Theory of Elastic Stability, 2nd Edition, McGraw-Hill, 1961.
9. D. Stienberg, Notes on Random Vibration Analysis for Electronic Equipment, 1979.
10. L. Meirovitch, Elements of Vibration Analysis, McGraw-Hill, 1975.

2.12.4 Description of LIBRA Files and Post-Processors: AOS Safety Analysis Report

THIS PAGE INTENTIONALLY LEFT BLANK

Description of Libra Files and Post-Processors:

AOS Safety Analysis Report

Prepared for: GE-Hitachi Nuclear Energy
PO No. 431004505
May 3, 2007

Prepared by: Structural Mechanics Analysis, Inc.
P.O. Box 700910
San Jose, CA 95170-0910

0.1 Table of Contents

0.2 List of Figures

1.0 Introduction

The Alpha-Omega Services (AOS) Safety Analysis Report (SAR) applies to four radioactive materials Type B cask configurations. These four cask configurations are designated by their relative size as AOS-025, AOS-050, AOS-100, and AOS-165. Configuration AOS-025 is approximately 25% the size of configuration AOS-100, configuration AOS-050 approximately 50%, and configuration AOS-165 approximately 165% in comparison to the AOS-100 model. The following provides a description of the Libra post-processors used to perform the structural and thermal analyses to support the preparation of the SAR for the four AOS cask models.

Notwithstanding the scaled nature of the four configurations, the thermal and stress analyses for the four models are not scalable. Rather, an independent set of analyses is required for each model. While the analyses are not scalable, the finite element models used in the analyses are largely scaled, although there are significant differences between models, particularly between model AOS-165 and the others.

Almost all of the thermal and stress analyses in the SAR are based on application of the Structural Mechanical Analysis, Inc. (SMA) Libra finite element program. The Libra program has been used by GE-Hitachi Nuclear Energy Americas, LLC ("GEH") for a number of years, and was used in the licensing of the Model 2000 Type B transport packaging. SMA has proprietorship of the Libra program, as a result, SMA was able to develop sophisticated post-processing tools integrated with the Libra program, that facilitated the AOS analyses.

The majority of the SAR analyses permit use of axisymmetric, finite element models, since for the majority of load cases the cask, loading, and boundary conditions are axisymmetric. As a result, four axisymmetric models were developed corresponding to the four cask configurations, and these models are the cornerstones of all the finite element analyses in the SAR. For load cases such as drop and transport, where assumptions of axisymmetric loading and boundary conditions are not applicable, 3D finite element models are used. These 3D models are generated from the axisymmetric models by rotation of the model. In this way, there is a well-defined relationship between elements in the axisymmetric and 3D models, and this relationship allows combining stress resultants from the two models.

The two U.S. Nuclear Regulatory Commission (NRC) documents that govern the analyses included in the SAR are Regulatory Guides 7.6 and 7.8. Reg. Guide 7.6 defines the allowable stresses for nuclear shipping casks, while Reg. Guide 7.8 defines the required loading conditions and load combinations. Further, Reg. Guide 7.6 specifies allowable stresses in terms of membrane and bending stresses, or more generally stress resultants. Stress resultants are not a direct output of finite element analyses. For the detailed models used in the AOS analyses, forming stress resultants involves identifying and integrating element stresses across a number selected cask cross-sections. This is an arduous and time consuming task. In addition, NRC Reg. Guide 7.8, which defines the load combinations that must be meet, presents additional difficult tasks for analyses based on the finite element method.

1.0 Introduction - Cont'd

Two major post-processing programs were developed to facilitate evaluation of stress resultants and stress combinations required by NRC Reg. Guides 7.6 and 7.8. The first, PmPb, forms the stress resultants required by Reg. Guide 7.6, while the second, CmbLds, forms the load combinations required by Reg. Guide 7.8. The methodology and application of these programs are described in detail in this report. The solution process for all of the four cask configurations involves first finding stresses corresponding to a set of basic load conditions, and then finding the stress combinations. For thermal loading conditions, one or more thermal solutions must be found before solving for stresses. After determining load case stresses, stress resultants are formed by application of the PmPb post-processing program. The PmPb program generates files containing stress resultants for the basic loading conditions. After all of the loading conditions have been run, and corresponding files of stress resultants generated by PmPb, The CmbLds program is executed. The CmbLds program reads the files generated by PmPb, forms the required combinations, and compares the combined stresses to the allowables in Reg. Guide 7.6. This entire process is automated by a Windows Command program, Run_AOS. A section of the Run_AOS batch program is shown in Appendix F.

2.0 PmPb Post Processor Program

The PmPb program forms the stress resultants referenced by Reg. Guide 7.6. The PmPb is a suite of three programs: PmPbData, PmPb, and PmPb3D. Each of these thee programs is described below. All three programs use the input file PmPb.in, which lists the elements at each model cross-section where stress resultants are evaluated. A sample PmPb.in file is shown in Appendix A.

The cross-sections on which PmPb operates are shown in Figures 1 and 2. Figure 1 shows the cross-sections for model 165, and Figure 2 shows the cross-section for models 025, 050, and 100. Model 165 has 25 stress cross-sections, while models 025,050, and 100 have 22 stress cross-sections. The larger number of cross-sections for model 165 is due to the split outer shell. The elements comprising the cross-sections shown in Figures 1 and 2 are defined on the respective input data file PmPb.dat. The 165 cask axisymmetric, and three dimensional finite element models are shown in Figures 3 and 4, respectively.

2.1 AOS Input Load Case designations

AOS Libra input data files all have designations starting with LCnnn, where nnn is a three digit load case number; and ending with suffix mmm, where mmm is a three digit model number. For example, the input file for thermal load case 101, model 025 is, LC101.025. Additional file description is entered following the load case number, with a hyphen preceding the entry. For example LC101-2500-UPDATE.025 is the designation for input file for thermal load case 101, 2500 watts, updated.

AOS load case numbers define the type of loading involved in the load case. Load cases numbered 101-199 are thermal loadings. Load cases 201-299 are pressure or other axisymmetric normal loadings. Load cases 301-399 are accident condition loadings. The load case types are used by the CmbLds program to determine allowable stress for load combinations.

2.2 PmPbData Program

PmPbData program determines the geometry data for the PmPb program, and stores this data on the file PmPb.dat. This geometry function is separated from the PmPb program for efficiency, as it needs to be performed only once for each model. PmPbData must be executed immediately following an execution of the Libra program, as it uses Libra output. The program reads Libra model geometry data from binary file Tape9, and generates the geometric data required to form membrane and moment stress resultants for each stress cross-section. This data is written to the file PmPb.dat, and is utilized by both PmPb and PmPb3D.

2.3 PmPb Program

The PmPb program generates files of membrane and bending stress resultants for axisymmetric loading conditions. The program utilizes the geometry data on the file PmPb.dat, the cross-section elements defined on PmPb.in, and Libra stress data on the binary file Tape8. PmPb generates output files labeled LOAD_CASE.nnn, where nnn is the load case number. For each LCnnn file there is a corresponding LOAD_CASE.nnn file. A typical output file generated by PmPb is shown in Appendix B. Output files list maximum principal stress, and membrane and bending stress for each cross-section. The PmPb program must be executed immediately following execution of a Libra stress run.

2.4 PmPb3D Program

The PmPb3D program generates files containing membrane and moment stress resultants for 3D loading conditions. The program utilizes the geometry data on the file PmPb.dat, cross-section element data on the file PmPb.in, and Libra stress output on the binary file Tape8. All AOS 3D models are generated from axisymmetric models. As a result, each element along a meridian corresponds to a element in the corresponding axisymmetric model. PmPb3D finds the stress resultants for each element along a meridian, and outputs maximum values on the LOAD_CASE file. Stress combinations involving axisymmetric and 3D load cases conservatively combine maximum meridian 3D values with axisymmetric values. The output of PmPb3D is the same as PmPb, and a typical file shown in Appendix B.

2.5 GroupAllow Program

The GroupAllow program finds maximum temperatures at cross-sections where stress resultants are evaluated, and interpolates temperature-dependent, allowable stress data to find the allowable cross-section stress corresponding to these maximum temperatures. This program is executed only for thermal load cases, and is executed after a Libra thermal solution. The GroupAllow program generates files ALLOWABLES.nnn, where nnn is load case number, and the file is subsequently used by the CmbLds program. A typical GroupAllow output file is shown in Appendix C.

3.0 CmbLds Program

As described in Section 2.3, The PmPb program generates stress resultant files LOAD_CASE.nnn, where nnn is the load case number. The CmbLds program forms load combinations using these files, and also determines the allowable stresses against which the combined stresses are compared. A typical CmbLds.in file is shown in Appendix D.

The load case number nnn in the file name LOAD_CASE.nnn defines the type of loading, as described in Section 2.1. LOAD_CASE.nnn files list both membrane and bending stress for each stress cross-section. The ALLOWABES.nnn files, described in Section 2.5, specify allowable stresses for thermal loadings. Based on all this information, the CmbLds program determines the maximum combined stress, the minimum allowable stress, and the minimum margin of safety at all stress cross-sections. The maximum stresses and minimum allowables are output on the file CmbLds.out. A typical output section generated by CmbLds is shown in Appendix E. The table in Appendix E lists the combined stress, allowable stress, and minimum margins of safety for each cross-section. The overall minimum margin of safety is listed at the end of the table.

4.0 AOS Files

The AOS input and output data files, PMPB verification files, and Libra Program files are contained on a single CD. The folders on this disk are listed below, and the following sections describe the contents of these folders.

aos-25	Input data files for AOS cask Model 025
aos-50	Input data files for AOS cask Model 050
aos-100	Input data files for AOS cask Model 100
aos-165	Input data files for AOS cask Model 165
aos-165-2500	Input data files for AOS cask Model 165, 2500 watts
PMPB_Verification	Verification report for post-processors
Source	Post-processors source code
aos-25-out	Output files for AOS cask Model 025
aos-50-out	Output files for AOS cask Model 050
aos-100-out	Output files for AOS cask Model 100
aos-165-out	Output files for AOS cask Model 165
aos-165-2500-out	Output files for AOS cask Model 165, 2500 watts
drop-25	Files for AOS cask Model 025 30' drop analyses
drop-50	Files for AOS cask Model 050 30' drop analyses
drop-100	Files for AOS cask Model 100 30' drop analyses
drop-165	Files for AOS cask Model 165 30' drop analyses

4.1 Input Data Files

The five input data folders, aos-25 ... aos-165-2500, contain all files required to run the Libra stress and thermal analyses for the five cask models. After establishing the Libra program (see Section 4.5), there is a two step process for executing Libra analyses and post-processing programs for a cask model: 1) copy the entire contents of an input data folder onto the Libra.app, or Libra.app sub-folder, directory; 2) execute the batch program RUN_AOS.

All input data is in English units. For thermal problems temperatures are in degrees F, energy in Btu, and length in inches. For structural problems loads are in lb, moduli in lb/in^2, and length in inches.

Libra executions may take several hours. Output from the Libra runs and post-processors consist of a series of text files labeled Load_Case.nnn, where nnn represents the load case number, and a file labeled Cmb_Loads.out. The Load_Case.nnn files contain the Pm and Pb stress measures at the monitored cask cross-sections for the individual load cases. The Cmb_Loads.out file contains the load combination results, including margins of safety for all combined load cases.

4.2 PMPB Verification Files

The PMPB_Verification folder contains both a report and a verification problem for PMPB and Cmb_Loads post-processors. The verification problem is a simple flat-top cylindrical shell under pressure and thermal loads. The stress resultants as two shell cross-sections are determined analytically, and by the PMPB and Cmb_Loads post processors. The two sets of results are shown to compare well.

A folder containing a set of verification problems for the Libra program, with emphasis on the AOS problem types, is established with installation of the Libra program (see Section 4.5). The Source folder contains the Fortran source codes for the six post processing programs used in the AOS Libra analyses.

4.3 Output Data Files

The AOS-25-out ... AOS-165-2500-out folders contain selected output from the individual Libra load case analyses (see Section 2.1). Each folder contains the LOAD_CASE file (see Section 2.4), The ALLOWABLES file (see Section 2.5), and the Libra output file (TAPE6) for each input data file. The extensions on LOAD_CASE, ALLOWABLES, and TAPE6 files are the same as the input file extension.

4.4 Files for 30' Drop Analyses

The four drop analysis folders, drop-25 ... drop-165, contain input and selected output files for the 30' head-on, side and cg/corner drop analyses. Each folder contains files for a single model, and for the three drop analyses. The output files are plot files for force-energy curves, model displacement, and model stress. The file names have -force,- disp, or -stress to indicate content. File names containing -cold are plots for -40° F thermal conditions, all other files are for 75° F.

The same Libra input data file can be used for all three drop orientations, with non-applicable orientation data commented out by an asterisk in column 1. All of the plot files are BMP format files, and may be viewed by means of the MS Paint program. The displacement and stress files are for displacement fields close to, but not necessarily at maximum values.

The drop-165 folder also contains the Libra input data file slap-down.t5 for slap-down analysis. This file is specifically for AOS model 165 cask, but is easily adapted to other cask models by changing the model structure dimensions and contact stiffness values. Contact stiffness values are taken from the 30' side-drop analyses.

5.0 Libra Installation

Libra installation files are contained in the Libra64 folder. The Libra Program is installed by executing the SETTUP program on the Libra64 folder. The SETUP program will request names for Libra Program and Application directories. Libra program files reside on the Program directory, and problems are executed from the Application directory or sub-directories. Default folder names are Libra64 for the program directory, and Libra.app for the application directory. The SETUP program will also prompt for installation of the 64-bit version of Libra. The 64-bit version should be installed only if the host operating system is 64 bits.

On Vista operating systems it may be necessary to set permission for running Script files before executing the Libra SETUP program. The following steps establish permission:

go to Control Panel
click on User Accounts
click on Turn user control on or off
uncheck user account control

After the Libra SETUP program is completed, the Libra program can be executed from the Start menu, or from the Command line in the Libra application folder. The AOS files are organized to run from the Libra Command line. To access the Libra Command line, left click on the Libra Desktop icon. To then execute a Libra input file, at the Command prompt enter,

Libra input_file output_file

If output_file is omitted, the default file name is TAPE6. After a Libra execution, the model can be viewed by entering HPLOT at the command prompt, and stresses viewed by entering STRSPP. Both HPLOT and STRSPP are menu driven.

To execute a set of AOS analyses on the distribution disk, say \aos-25, read the entire contents of \aos-25 onto the application directory (or sub-directory), then enter run_aos at the Command prompt. This executes the batch program run_aos, which executes all of the files and post-processors for AOS Model 025. Output will be contained on a set of files labeled Load_Case.nnn, and on the file Cmb_Loads.out (see Sections 2.3 and 3.0).

Libra installation establishes a folder labeled Verification. This folder contains a number of verification problems for Libra elements and solution procedures. The thermal problems, and several of the structural problems are directly applicable to AOS analyses. In total, the verification problems in this folder encompass all of the Libra elements and solution procedures applied in the AOS analyses. The verification files described in Section 4.2 address the post-processors used in the AOS analyses, and are an adjunct to these Libra verification problems.

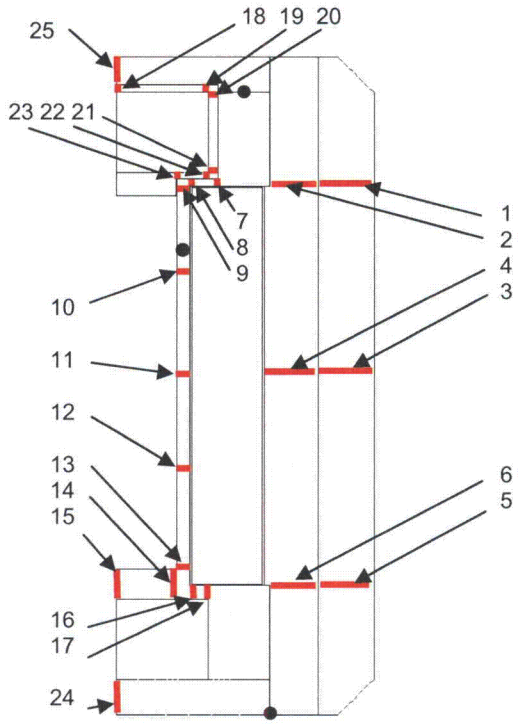

Figure 1. Model 165 PmPb Cross-Sections

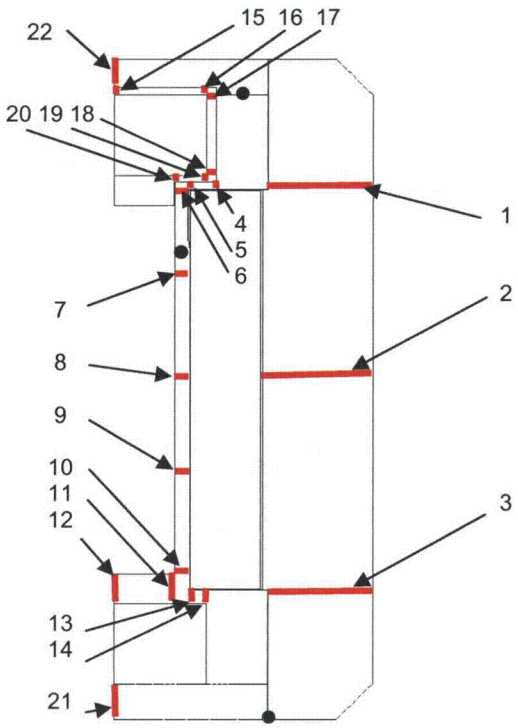

Figure 2. Models 025, 050 and 100 PmPb Cross-Sections

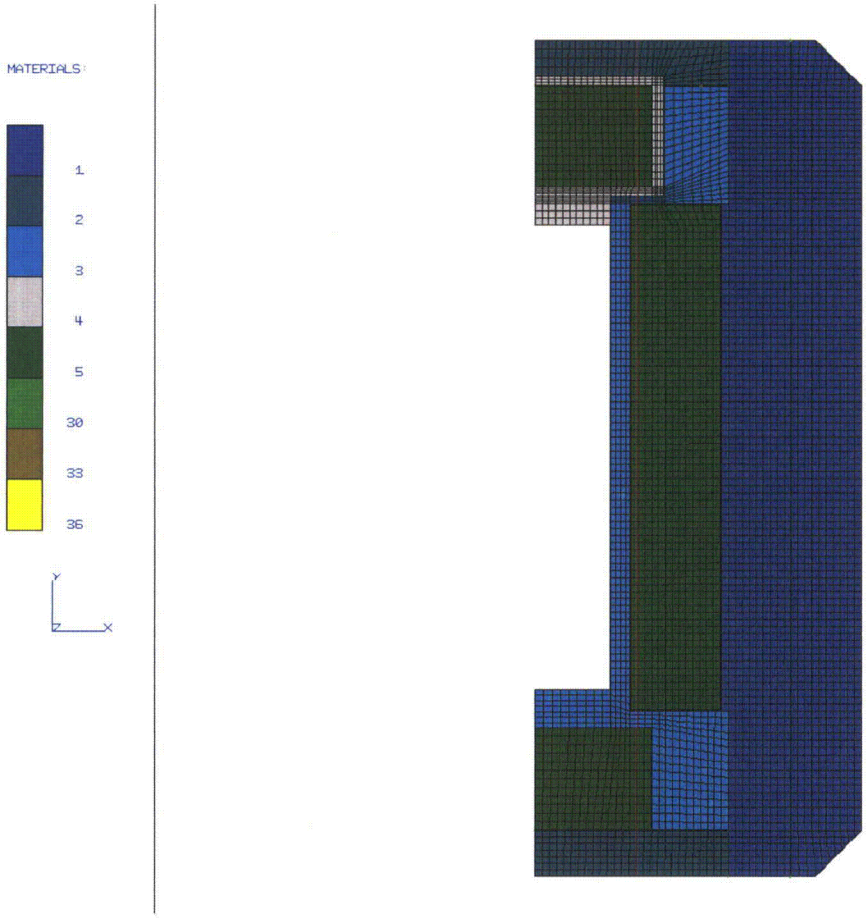

Figure 3. Axisymmetric FEA Model of 165 Cask

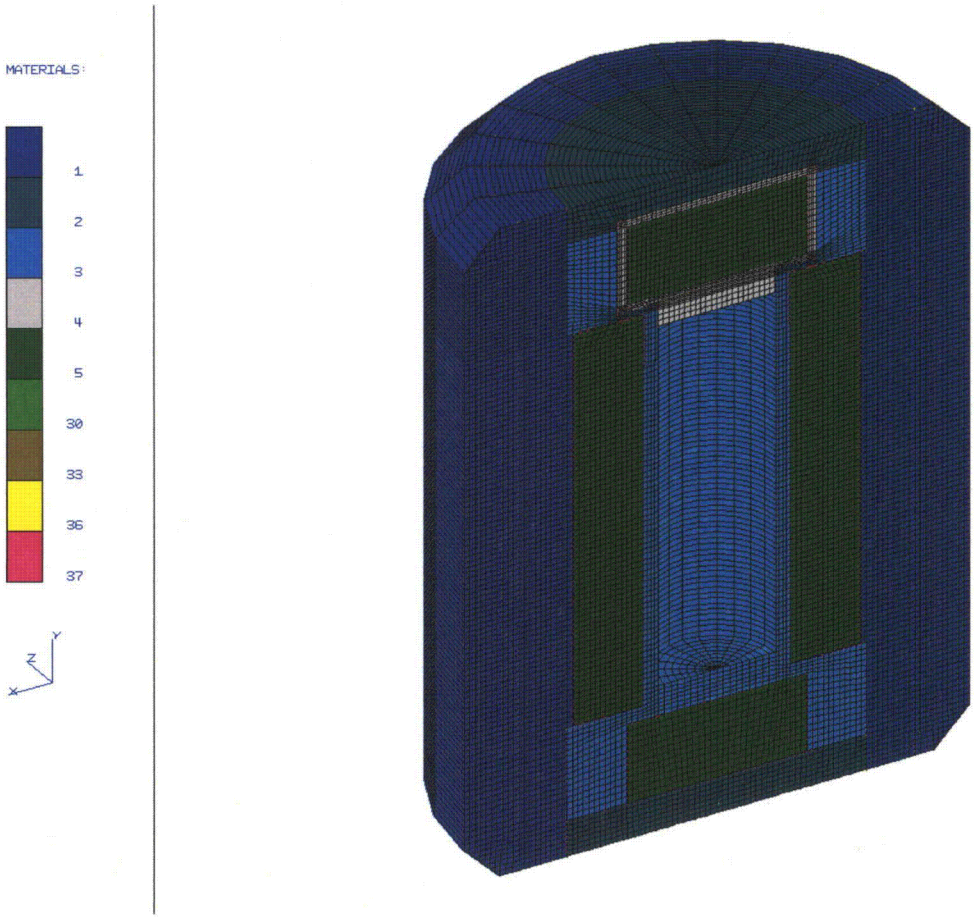

Figure 4. Three Dimensional FEA Model of 165 Cask

Appendix A. Typical PmPb.in File

The following is a typical PmPb.in file listing elements at each stress cross-section. For ease of viewing, cross-section entries are not confined to one line, and blank lines separate entries. In the actual file all section entries are on one line, and there are no blank lines.

```
1957,1958,1959,1960,1961,1962,1963,1964,1965,2146,2147,2148,2149,2150,
2151,2152,2153,2154,2155

552,904,905,906,907,908,909,910,911,912,1587,1588,1589,1590,1591,1592,
1593,1594,1595,1596

348,349,350,351,352,353,354,355,356,507,508,509,510,511,512,513,514,515,
516

4587,4591,4595,4599

4572,4575,4578,4581

552,4553,4554,4555

4476,4477,4478,4479

4408,4409,4410,4411

4344,4345,4346,4347

4280,4281,4282,4283

4141,4150,4159,4168,4177,4186,4195

4133,4142,4151,4160,4169,4178,4187

4212,4215,4218,4221

4214,4217,4220,4223

5218,5236,5254

5235,5253,5271

5214,5215,5216,5217

5166,5167,5168,5169

5140,5143,5146,5149

5122,5126,5130,5134

3001,3017,3033,3049,3065,3081,3097

3190,3208,3226,3244
```

Appendix B. PmPb output file, LOAD_CASE.101

The following is the PmPb output file for load case LC101.025. The file lists maximum principal stresses, and calculated membrane and bending stress at each section analyzed. Stresses are listed in both English and metric units.

Load Case_101 - 100F Ambient, Max Decay Heat

Stress (psi/MPa)

Location	Sigma_1	Sigma_2	Sigma_3	Pm	Pb
1	1.2232E+01	-2.5191E+01	-1.8387E+00	3.7423E+01	5.8177E+01
	8.4340E-02	-1.7369E-01	-1.2677E-02	2.5803E-01	4.0111E-01
2	1.6225E+01	-3.2962E+01	-6.5255E+00	4.9187E+01	1.0016E+02
	1.1187E-01	-2.2727E-01	-4.4992E-02	3.3913E-01	6.9059E-01
3	1.0870E+01	-2.3382E+01	-1.1174E+00	3.4252E+01	5.3526E+01
	7.4943E-02	-1.6122E-01	-7.7043E-03	2.3616E-01	3.6905E-01
4	6.2382E+01	-2.3843E+02	-4.1530E+01	3.0081E+02	5.9563E+02
	4.3011E-01	-1.6439E+00	-2.8634E-01	2.0740E+00	4.1067E+00
5	6.1432E+01	-2.6905E+02	-1.2242E+02	3.3048E+02	5.2038E+02
	4.2356E-01	-1.8550E+00	-8.4406E-01	2.2786E+00	3.5879E+00
6	6.4534E+00	-1.3381E+02	-1.5795E+02	1.4026E+02	1.6725E+02
	4.4494E-02	-9.2256E-01	-1.0890E+00	9.6705E-01	1.1532E+00
7	-1.9752E+00	-4.9672E+01	2.5928E+00	4.7697E+01	4.3899E+01
	-1.3619E-02	-3.4248E-01	1.7877E-02	3.2886E-01	3.0267E-01
8	-2.0037E+00	-4.9648E+01	1.9949E-03	4.7644E+01	4.3457E+01
	-1.3815E-02	-3.4231E-01	1.3755E-05	3.2850E-01	2.9962E-01
9	-1.9811E+00	-4.9582E+01	-5.2273E-01	4.7600E+01	4.1764E+01
	-1.3659E-02	-3.4185E-01	-3.6041E-03	3.2819E-01	2.8795E-01
10	-7.5888E+00	-6.6970E+01	1.0700E+01	5.9381E+01	1.2009E+02
	-5.2323E-02	-4.6174E-01	7.3772E-02	4.0942E-01	8.2802E-01
11	-1.6114E+01	-1.0104E+02	-5.3150E+01	8.4930E+01	7.0193E+00
	-1.1110E-01	-6.9668E-01	-3.6645E-01	5.8557E-01	4.8396E-02
12	4.9440E+00	-1.1870E+02	-1.1938E+02	1.2364E+02	7.5796E+00
	3.4087E-02	-8.1839E-01	-8.2311E-01	8.5248E-01	5.2260E-02

13	-1.3346E+01	-1.7829E+02	-2.9776E+01	1.6495E+02	8.7679E+01
	-9.2016E-02	-1.2293E+00	-2.0530E-01	1.1373E+00	6.0452E-01
14	-1.2832E+01	-1.5680E+02	3.6799E+00	1.4396E+02	9.5911E+01
	-8.8473E-02	-1.0811E+00	2.5372E-02	9.9259E-01	6.6128E-01
15	3.4752E+02	-3.2306E+02	-3.0278E+01	6.7058E+02	1.1250E+03
	2.3960E+00	-2.2274E+00	-2.0876E-01	4.6235E+00	7.7568E+00
16	1.2110E+02	-2.3963E+02	-7.8259E+01	3.6074E+02	5.8708E+02
	8.3498E-01	-1.6522E+00	-5.3958E-01	2.4872E+00	4.0478E+00
17	5.3313E+01	-1.6483E+02	7.7898E+00	2.1815E+02	3.7767E+02
	3.6758E-01	-1.1365E+00	5.3709E-02	1.5041E+00	2.6039E+00
18	1.3652E+01	-8.6978E+01	1.2149E+02	1.0063E+02	1.5144E+02
	9.4130E-02	-5.9969E-01	8.3767E-01	6.9382E-01	1.0442E+00
19	3.7352E+01	-1.4759E+02	9.9594E+01	1.8495E+02	3.1090E+02
	2.5754E-01	-1.0176E+00	6.8668E-01	1.2752E+00	2.1436E+00
20	2.5189E+01	-1.9576E+02	9.1481E+00	2.2095E+02	4.1088E+02
	1.7367E-01	-1.3497E+00	6.3074E-02	1.5234E+00	2.8329E+00
21	6.6491E+00	-2.2294E+00	-1.0467E+00	8.8785E+00	6.0550E+00
	4.5844E-02	-1.5371E-02	-7.2168E-03	6.1215E-02	4.1748E-02
22	2.7655E+00	-1.5235E+01	-3.0961E+00	1.8000E+01	4.4221E+01
	1.9068E-02	-1.0504E-01	-2.1347E-02	1.2411E-01	3.0489E-01

Appendix C. GroupAllow Program Output File

The following is the GroupAllow program output file for load case LC101.025. This file lists maximum and average temperatures at each stress section, and the allowable membrane, yield, and ultimate stress at these sections.

Allowable Stress for Load Case 101

LOC	Tmax (deg_F)	Tave (deg_F)	Sm (ksi)	Sy (ksi)	Su (ksi)
1	138.91	138.74	20.00	30.00	70.00
2	138.94	138.59	20.00	30.00	70.00
3	138.62	138.37	20.00	30.00	70.00
4	139.15	139.13	20.00	30.00	70.00
5	139.61	139.54	20.00	30.00	70.00
6	139.79	139.72	20.00	30.00	70.00
7	140.04	139.89	20.00	30.00	70.00
8	139.99	139.85	20.00	30.00	70.00
9	139.92	139.77	20.00	30.00	70.00
10	139.78	139.64	20.00	30.00	70.00
11	139.92	139.66	20.00	30.00	70.00
12	140.39	140.09	20.00	30.00	70.00
13	139.33	139.20	20.00	30.00	70.00
14	139.04	138.97	20.00	30.00	70.00
15	139.08	139.03	20.00	30.00	70.00
16	139.19	139.14	20.00	30.00	70.00
17	139.22	139.19	20.00	30.00	70.00
18	139.37	139.34	20.00	30.00	70.00
19	139.50	139.44	20.00	30.00	70.00
20	140.26	140.14	20.00	30.00	70.00
21	138.43	138.36	20.00	30.00	70.00
22	138.82	138.76	20.00	30.00	70.00

Appendix D. Typical CmbLds.in File

The following is a typical PmPb.in file. The first entry is the number of stress cross-sections. The next set of entries is the load case numbers, and this set is terminated with a -1. The second and last set of entries are the load combination numbers, and the combination load cases. Text following entries is descriptive, and not used by the program

```
22
101       ; 100F Ambient, Max Decay Heat
102       ; 100F Ambient, Max Decay Heat, Max Insolation
103       ; -20F Ambient, Zero Decay Heat, Zero Insolation
104       ; -40F Ambient, Zero Decay Heat, Zero Insolation
105       ; -40F Ambient, Max Decay Heat
111       ; Fire @ 30 Min, 1475F Ambient, Max Decay Heat
112       ; Fire @60 Min, 100F, Max Decay Heat,Max Insolation
113       ; Fire @90 Min, 100F, Max Decay heat,Max Insolation
114       ; Fire @120 Min, 100F, Max Decay Heat,Max Insolation
115       ; Fire @150 Min, 100F, Max Decay Heat,Max Insolation
116       ; Fire @180 Min, 100F, Max Decay Heat,Max Insolation
201       ; Maximum Internal Pressure, 30 psi
202       ; Minimum External Pressure, 3.5 psia
203       ; Maximum Increased Pressure, 20 psia
204       ; Additional Increased External Pressure, 290 psi
211       ; Fabrication Stress
215       ; Compression Load
216       ; Rod Drop
221       ; Forward 5g Vibration Inertia Load
222       ; Lateral 5g Vibration Inertia Load
223       ; Vertical 10g Vibration Inertia Load
231       ; 4 ft head-on drop
232       ; 30 ft head-on drop, normal conditions
301       ; 30 ft Head-on drop
302       ; 30 ft Side drop + slap-down
303       ; CG/Corner Drop
304       ; 30 ft Head-on drop, low temp
305       ; 30 ft Side drop + slap-down, low temp
306       ; CG/Corner Drop, low temp
311       ; 3 ft drop onto rod
-1
101, 101,201,211          ; hot environment
102, 104,201,211          ; cold environment
103, 103,201,211          ; increaded ex pres
104, 101,201,202,211      ; min ex pres
105, 105,201,202,211      ; cold environment
106, 101,201,203,211      ; max pres, hot environment
107, 105,201,203,211      ; max pres, cold environment
215, 215,101,201,211      ; compression load
216, 216,101,201,211      ; rod drop
217, 216,104,201,211      ; rod drop cold environment
221, 221,101,201,211      ; fwd vibration
222, 222,101,201,211      ; lateral vibration
```

```
223, 223,101,201,211     ; vertical vibration
231, 231,102,201,211     ; 4 ft head-on drop, normal conditions
232, 232,102,201,211     ; 30 ft head-on drop, normal conditions
301, 301,102,201,211     ; head-on drop
302, 302,102,201,211     ; side drop
303, 303,102,201,211     ; cg/corner drop
304, 304,105,202,211     ; head-on drop, cold environment
305, 305,105,202,211     ; side drop, cold environment
306, 306,105,202,211     ; cg/corner drop, cold environment
310, 204,101,211         ; add ext pres (290 psi)
311, 311,101,201,211     ; 3 ft drop onto rod
312, 311,104,201,211     ; 3 ftdrop onto rod, cold environment
350, 111,201,211         ; fire @ 30 min
351, 112,201,211         ; fire @ 60 min
352, 113,201,211         ; fire @ 90 min
353, 114,201,211         ; fire @ 120 min
354, 115,201,211         ; fire @ 150 min
355, 116,201,211         ; fire @ 180 min
-1
```

Appendix E. Typical Output from CmbLds Program

The following is a typical output file from the CmbLds program. The load combination is listed at the top of the table. The file lists maximum membrane and bending stress, and minimum allowables at each section analyzed. Stresses are listed in both English and metric units. Minimum MS and associated values are listed at the end of the table.

```
Normal Load Combination  101
----------------------------
Load Cases: 101 201 211
100F Ambient, Max Decay Heat
Maximum Internal Pressure - 30 Psia
Fabrication Stress
```

	Stress (ksi/MPa)							
Loc	Pm	Pb	Q	Pm+Pb	Pm+Pb+Q	Sm	Su	MS
1	0.75	1.10	0.04	1.85	1.89	20.00	70.00	>10
	5.16	7.60	0.26	12.75	13.01	137.90	482.63	
2	0.14	0.20	0.05	0.34	0.38	20.00	70.00	>10
	0.96	1.35	0.34	2.31	2.65	137.90	482.63	
3	0.08	0.08	0.03	0.16	0.20	20.00	70.00	>10
	0.58	0.54	0.24	1.12	1.36	137.90	482.63	
4	1.16	1.78	0.30	2.94	3.24	20.00	70.00	9.20
	8.00	12.28	2.07	20.28	22.35	137.90	482.63	
5	1.18	1.00	0.33	2.18	2.51	20.00	70.00	>10
	8.17	6.88	2.28	15.05	17.32	137.90	482.63	
6	0.78	1.17	0.14	1.95	2.09	20.00	70.00	>10
	5.40	8.05	0.97	13.44	14.41	137.90	482.63	
7	0.34	0.07	0.05	0.40	0.45	20.00	70.00	>10
	2.34	0.45	0.33	2.79	3.12	137.90	482.63	
8	0.32	0.04	0.05	0.36	0.41	20.00	70.00	>10
	2.21	0.27	0.33	2.48	2.81	137.90	482.63	
9	0.36	0.07	0.05	0.43	0.48	20.00	70.00	>10
	2.48	0.48	0.33	2.97	3.29	137.90	482.63	
10	1.23	0.15	0.06	1.38	1.44	20.00	70.00	>10
	8.49	1.03	0.41	9.52	9.93	137.90	482.63	

11	0.93	1.23	0.08	2.17	2.25	20.00	70.00	>10
	6.44	8.51	0.59	14.95	15.53	137.90	482.63	
12	1.01	1.49	0.12	2.50	2.62	20.00	70.00	>10
	6.95	10.27	0.85	17.23	18.08	137.90	482.63	
13	1.19	1.05	0.16	2.24	2.40	20.00	70.00	>10
	8.21	7.23	1.14	15.44	16.58	137.90	482.63	
14	1.21	1.54	0.14	2.75	2.89	20.00	70.00	9.91
	8.36	10.61	0.99	18.97	19.96	137.90	482.63	
15	1.70	1.94	0.67	3.64	4.31	20.00	70.00	7.25
	11.69	13.38	4.62	25.07	29.70	137.90	482.63	
16	1.70	2.69	0.36	4.39	4.75	20.00	70.00	5.83
	11.72	18.55	2.49	30.27	32.75	137.90	482.63	
17	1.12	1.79	0.22	2.90	3.12	20.00	70.00	9.33
	7.71	12.31	1.50	20.02	21.52	137.90	482.63	
18	0.87	1.40	0.10	2.27	2.37	20.00	70.00	>10
	5.99	9.65	0.69	15.64	16.33	137.90	482.63	
19	1.46	2.17	0.18	3.63	3.82	20.00	70.00	7.26
	10.09	14.96	1.28	25.05	26.33	137.90	482.63	
20	1.82	2.90	0.22	4.72	4.95	20.00	70.00	5.35
	12.58	19.99	1.52	32.57	34.09	137.90	482.63	
21	0.32	0.44	0.01	0.76	0.77	20.00	70.00	>10
	2.24	3.00	0.06	5.24	5.30	137.90	482.63	
22	0.46	0.47	0.02	0.93	0.95	20.00	70.00	>10
	3.20	3.23	0.12	6.43	6.55	137.90	482.63	

Min MS: 5.350, Location: 20, Combination: Pm+Pb

Appendix F. Typical Section of Batch Program to Execute AOS Load Cases

The AOS input data files and post-processor executions are organized and run by a Command batch program. A separate batch program is required for each of the four model configurations. A section of a typical batch program is shown below. Note that the program PmPbData is run before the first execution of PmPb. The GroupAllow program is only run after a Libra thermal analysis. The PmPb (or PmPb3D) program is run after each Libra stress analysis. Calls to the Libra program include the input file name, output file name, and a flag set to 1 to prevent Libra pausing after execution.

```
rem load case 101
call libra lc101-t-update.025  tape6 1
call libra lc101-update.025  tape6 1
groupallow lc101-update.025
pmpbdata
pmpb

rem load case 102
call libra lc102-t-update.025  tape6 1
call libra lc102-update.025  tape6 1
groupallow lc102-update.025
pmpb

rem load case 103
call libra lc103-t-update.025  tape6 1
call libra lc103-update.025  tape6 1
groupallow lc103-update.025
pmpb

rem load case 104
call libra lc104-t-update.025  tape6 1
call libra lc104-update.025  tape6 1
groupallow lc104-update.025
pmpb

rem load case 105
call libra lc105-t-update.025  tape6 1
call libra lc105-update.025  tape6 1
groupallow lc105-update.025
pmpb

rem load case 106
call libra lc106-t-update.025  tape6 1
call libra lc106-update.025  tape6 1
groupallow lc106-update.025
pmpb
```

THIS PAGE INTENTIONALLY LEFT BLANK

2.12.5 Selected Material Properties References

This appendix provides information related to the following materials, that is not included elsewhere in the SAR:

- Contact Resistance
- Decay Heat
- Structural Stability
- Tungsten Alloy
- General Plastics LAST-A-FOAM
- Port Seal

THIS PAGE INTENTIONALLY LEFT BLANK

Contact Resistance

THIS PAGE INTENTIONALLY LEFT BLANK.

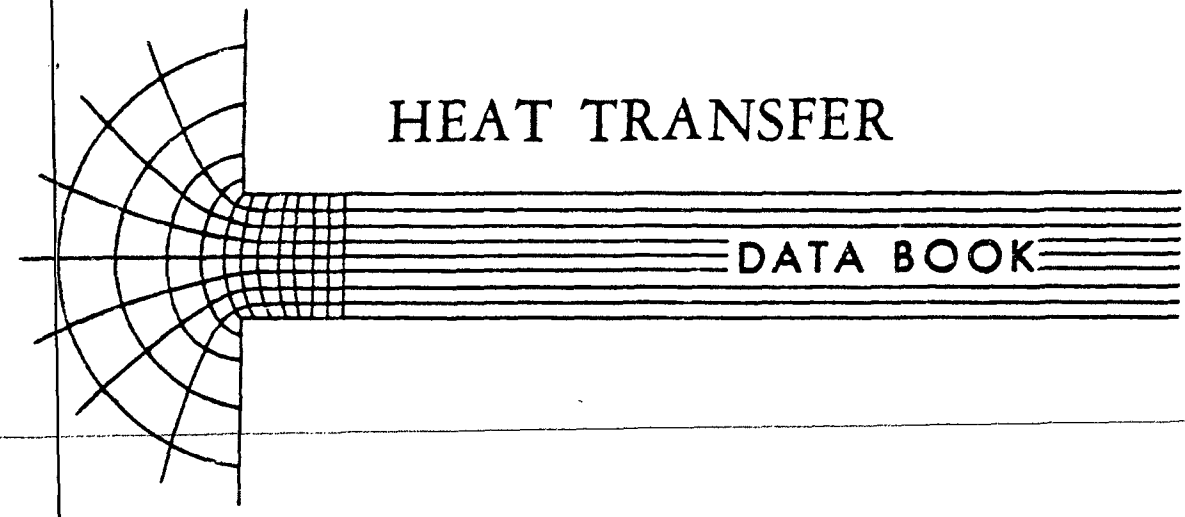

HEAT TRANSFER

DATA BOOK

EDITORS	TENURE AS EDITOR
R. Hosmer Norris	1943 - 1971
Mrs. Florence F. Buckland	1943 - 1963
Mrs. Nancy D. Fitzroy	1956 -

GENERAL ELECTRIC COMPANY
CORPORATE RESEARCH AND DEVELOPMENT
Schenectady, N.Y.

STEEL, BARE SURFACES AT HIGH CONTACT PRESSURES (0 to 1200 psi) - Solid blocks in air at reduced pressure (p < 0.1 atm)

For steel with bare surfaces in air, see pages 5-6.
For steel with sandwich material in air, see page 8.
For steel in other gases, see page 9.
For steel with dissimilar metal in air, see page 20; at reduced pressure (p < 0.1 atm), see page 21.
For other metals in air, see pages 10-11, 17; at reduced pressure (p < 0.1 atm), see pages 12-13, 18-19.
For laminated steels in air, see page 23.

Curve	Material[4]	Finish	Roughness Rms (μ in.) Block 1	Roughness Rms (μ in.) Block 2	Fluid in Gap	Temp (°F)	Condition	Ref. No.[3]
a	Stainless Steel 304	Ground	42-60	43-48	Air	75	Clean, 10^{-4} mm Hg abs	45
b	Stainless Steel 304	Ground	15-15	10-10	Air	84	Clean, 10^{-4} mm Hg abs	45

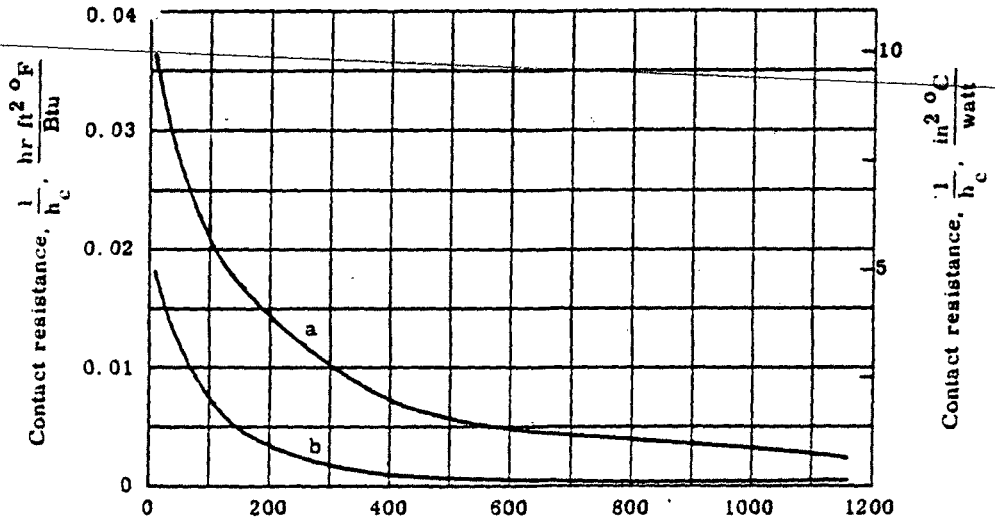

4-5 See page 24

Decay Heat

Decay Heat Load

Model AOS-025 Cask

Decay Heat = 10W

$$10W = 3.4121 * 10 = 34.121 \text{ Btu/hr}$$

Cavity Area

$$A = 2\pi (0.812^2 + (0.612)(7.0 - 2.0))$$

$$= 29.65 \text{ in}^2$$

Heat Flux

$$q = 341.21 / 29.65$$

$$= 1.151 \text{ Btu/hr-in}^2$$

Model AOS-050 Cask

Decay Heat = 100W

$$100W = 3.4121 * 100 = 341.21 \text{ Btu/hr}$$

Cavity Area

$$2\pi (1.62424^2 + 1.62424 * (14.0 - 4.0))$$

$$= 118.63 \text{ in}^2$$

Heat Flux

$$341.21 / 118.63 = 2.876 \text{ Btu/hr-in}^2$$

Outside Cask Body and Cask Height – Model AOS-100

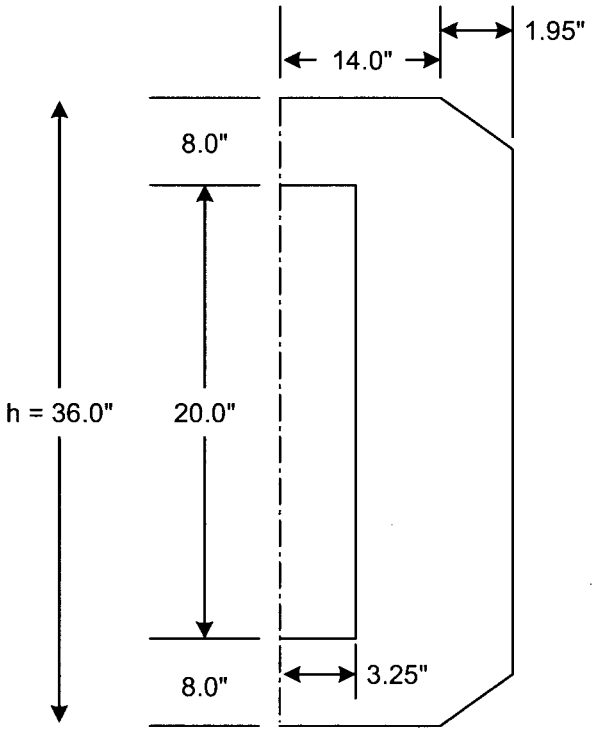

Decay Heat = 400W

400W = 3.4121 * 400 = 1,365 Btu/hr

Cavity Surface Area

$2\pi (3.25^2 + ((3.25)(20))) = 474.77 \text{ in}^2$

Heat Flux

$1{,}365 / 474.77 \text{ in}^2 = 2.88 \text{ Btu/hr-in}^2$

THIS PAGE INTENTIONALLY LEFT BLANK.

Structural Stability

THIS PAGE INTENTIONALLY LEFT BLANK.

INTRODUCTION TO
Structural Stability Theory

GEORGE GERARD, Sc.D.

Associate Director of Research and
Research Professor of Aeronautics
College of Engineering, New York University

McGRAW-HILL BOOK COMPANY, INC. 1962

New York *Toronto* *London*

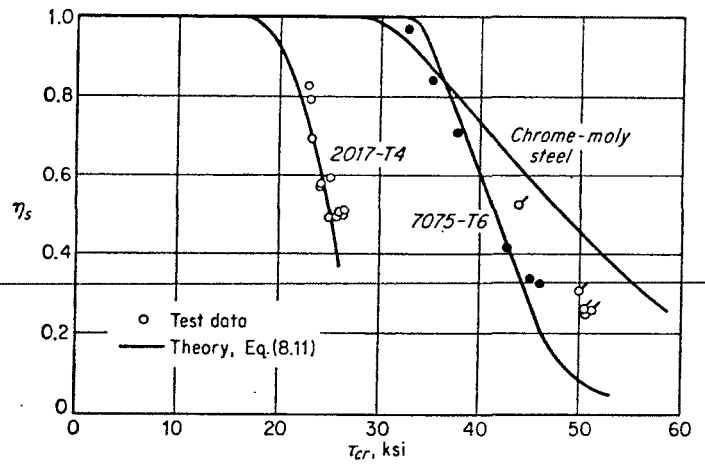

FIG. 8.4. Comparison of test data with plasticity-reduction factor for long cylinders in torsion.

In Fig. 8.3, test data (summarized in Ref. 8.2) on failure of cylinders in torsion of several materials are presented and compared with theory. It can be observed that the upper limit of the test data does conform to the theory. As a result of the postbuckling behavior of cylinders in torsion, there is a considerable mass of test data that lie somewhat below the theory. On the whole, the average of the test data is approximately 15 per cent below theory in the moderate-length-cylinder range.

Before discussing the discrepancy for the torsion case any further, it is convenient to consider the axial compressive buckling of cylinders. Certain additional principles have been evolved in connection with the compressive case that are useful in discussing the small discrepancy between theory and test data in the torsion case (Sec. 8.7).

For torsional loadings, inelastic stability of moderate-length and long cylinders has been considered in Ref. 8.4, and the following plasticity-reduction factor has been derived:

$$\eta_s = \left(\frac{1 - \nu_e^2}{1 - \nu_p^2}\right)^{3/4} \frac{E_s}{E} \tag{8.11}$$

A comparison of Eq. (8.11) with test data summarized in Ref. 8.6 on several materials is presented in Fig. 8.4. Agreement between test data and theory is particularly good for the two aluminum alloys.

8.4. ELASTIC STABILITY UNDER COMPRESSION

For a circular cylinder under axial compression, $N_{xy} = N_y = 0$, $N_x = \sigma t$, and therefore the governing equilibrium relation [Eq. (7.33)]

reduces to

$$D\nabla^8 w + \sigma t \nabla^4 \frac{\partial^2 w}{\partial x^2} + \frac{Et}{R^2}\frac{\partial^4 w}{\partial x^4} = 0 \tag{8.12}$$

A solution of Eq. (8.12) that satisfies the boundary conditions of simple support at the ends of the cylinder is

$$w = w_{mn} \sin \frac{m\pi x}{L} \sin \frac{ny}{R} \tag{8.13}$$

Upon substituting the appropriate derivatives of Eq. (8.13) into (8.12), the following nontrivial solution is obtained:

$$\sigma_{cr} = \frac{\pi^2 k_c E}{12(1 - \nu^2)} \left(\frac{t}{L}\right)^2 \tag{8.14}$$

where

$$k_c = \frac{(m^2 + \beta^2)^2}{m^2} + \frac{12Z^2 m^2}{\pi^4 (m^2 + \beta^2)^2} \tag{8.15}$$

$$\beta = \frac{nL}{\pi R}$$

It can be observed that the wavelength parameter $(m^2 + \beta^2)^2/m^2$ appears in both terms of Eq. (8.15). By minimizing Eq. (8.15) with respect to this parameter, we obtain

$$\frac{(m^2 + \beta^2)^2}{m^2} = \left(\frac{12Z^2}{\pi^4}\right)^{1/2} \tag{8.16}$$

Substituting into Eq. (8.15), we obtain the solution for a moderate-length cylinder under compression:

$$k_c = 0.702Z \tag{8.17}$$

By substituting Eq. (8.17) into (8.14), we obtain the simple result

$$\sigma_{cr} = CE\frac{t}{R} \tag{8.18}$$

where

$$C = [3(1 - \nu^2)]^{-1/2} \cong 0.6$$

We return now to Eq. (8.16) to establish the range of validity of Eqs. (8.17) and (8.18). By solving Eq. (8.16) for β, we obtain

$$\beta = \left[\frac{(12Z^2)^{1/4}}{\pi} m - m^2\right]^{1/2} \tag{8.19}$$

Since, as a minimum, $m = 1$, it is apparent that for real values of β

$$Z \geq \frac{\pi^2}{12^{1/2}} \geq 2.85 \tag{8.20}$$

Thus, the moderate-length-cylinder solution applies for values of Z greater than 2.85.

Short Cylinders

For short cylinders of Z less than 2.85, the values of $\beta = 0$ and $m = 1$ are to be substituted into Eq. (8.15). Thus, for a simply supported cylinder in the short-cylinder range,

$$k_c = 1 + \frac{12Z^2}{\pi^4} \tag{8.21}$$

In this region, the short cylinder behaves in the same manner as a wide, simply supported column which buckles into one half-wave-

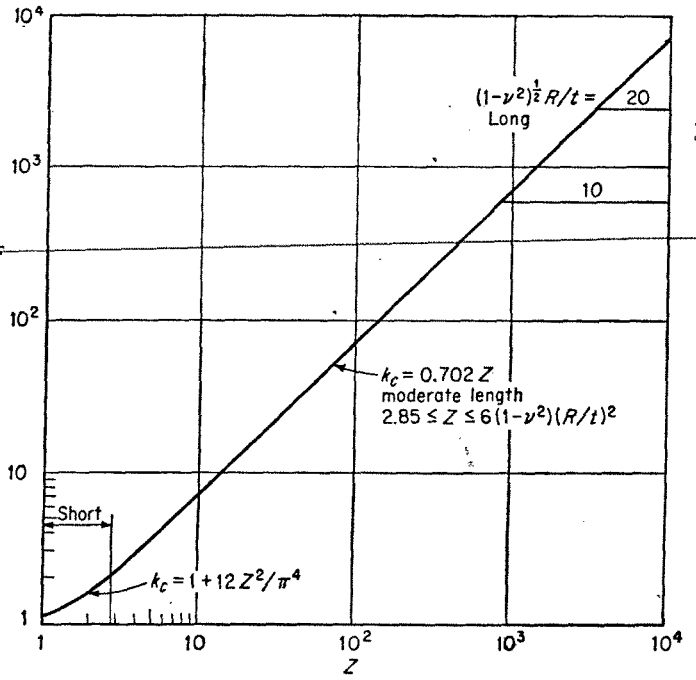

$Z = \frac{L^2\sqrt{1-\nu^2}}{Rt}$

FIG. 8.5. Buckling coefficients for simply supported circular cylinders under axial compression.

length in the loaded axial direction, $m = 1$, and none in the unloaded direction, $n = 0$.

The results given by Eqs. (8.17) and (8.21) are shown in Fig. 8.5. It is to be noted that, at large values of Z, long cylinders buckle as Euler columns with no distortion of the circular cross section. For

cylinders of practical R/t values, however, Euler buckling occurs at values of Z beyond those shown in Fig. 8.5.

8.5. Postbuckling Behavior under Compression

By using the large-deflection equations [Eqs. (7.51) and (7.52)], many investigators have studied the postbuckling behavior of compressed cylinders of moderate length. The essential theoretical results of such an analysis by Donnell and Wan (Ref. 8.7) are shown in Fig. 8.6 for both perfect cylinders and those containing small initial imperfections.

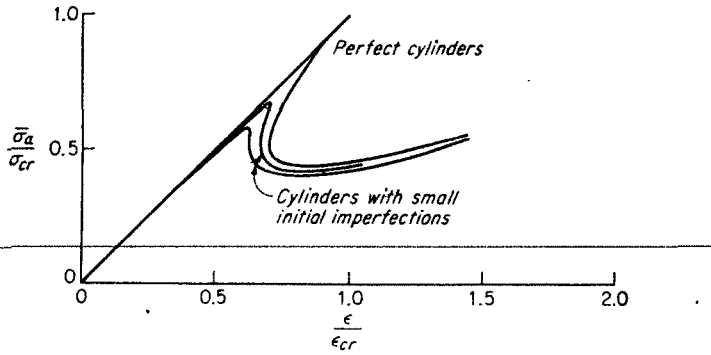

Fig. 8.6. Postbuckling behavior of moderate-length cylinders in axial compression.

It can be seen from Fig. 8.6 that the influence of curvature observed previously in connection with the torsion case is greatly accentuated. For the perfect cylinder under compression, a precipitous decline from the linear buckling stress of Eq. (8.18) occurs after buckling. Of particular importance is the fact that, with continued end shortening, the load-carrying ability is significantly reduced, and it is probably not regained before the onset of plasticity effects.

Cylinders with small initial imperfections exhibit the same type of behavior. Here, too, the postbuckling load-carrying ability apparently does not rise again to the peak load in the region of buckling before the onset of plasticity. As a consequence, we should expect that the failure of moderate-length cylinders in axial compression should be profoundly influenced by the magnitude of the initial imperfections in the cylinder.

This expectation is indeed borne out by the comparison of the linear theory presented in Sec. 8.4 with the large mass of experimental data

on failure of compressed cylinders (Fig. 8.7). It can be observed that none of the test data in the moderate-length region reach the theory and that all are significantly below the theory. Only in the short-cylinder region do the data exceed theory. This is because the test data are for cylinders with clamped ends ($k = 4$ for wide column), whereas the theory is for simply supported ends ($k = 1$ for wide column).

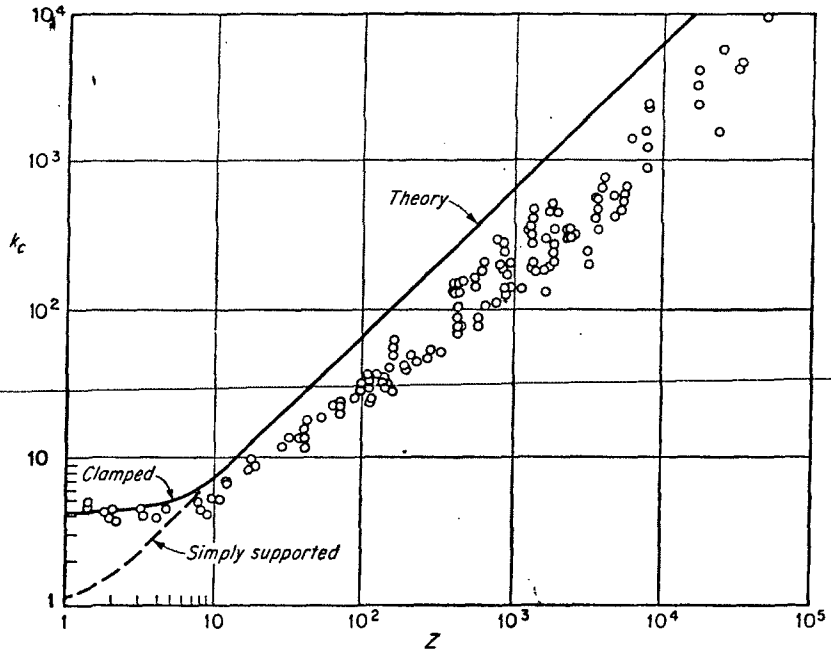

FIG. 8.7. Comparison of linear buckling theory with test data for circular cylinders under axial compression.

At this point, we have reached a rather startling development in that a most significant discrepancy between the results of linear stability theory and experimental data exists. The cause of the discrepancy appears to be associated with the unusual postbuckling behavior of an axially compressed cylinder, and therefore it would seem that we must account for large-deflection effects in this case. Before proceeding to the large-deflection theories that have been developed to resolve this discrepancy, however, we shall first compare the physical behavior of columns, plates, and shells in order to appreciate when large-deflection effects are likely to be of importance.

8.6. Behavior of Compressed Elements

A schematic representation of the postbuckling behavior of axially compressed columns, flat plates, and cylinders is shown in Fig. 8.8 for both theoretically perfect elements and those containing small initial imperfections. It is assumed here that all elements behave elastically.

For the perfect column, the postbuckling behavior is essentially horizontal in the range of end-shortening values considered. The horizontal behavior can be attributed to the fact that, after buckling, no significant transverse-tension membrane stresses are developed to

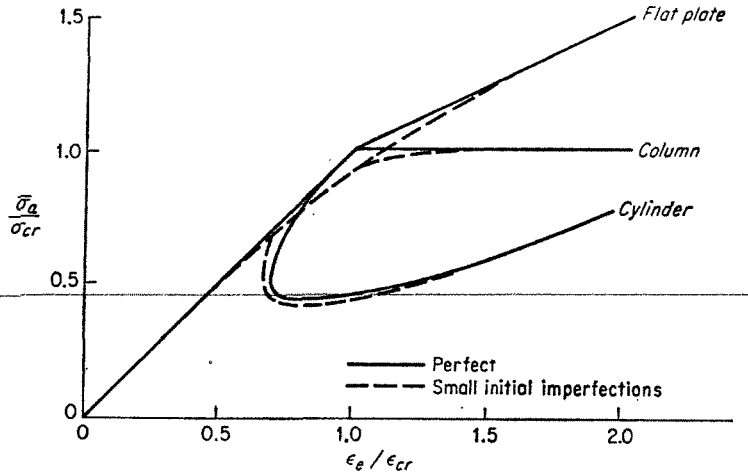

Fig. 8.8. Postbuckling behavior of axially compressed elastic elements.

restrain the lateral motion; therefore, the column is free to deflect laterally under the buckling load.

The flat plate, however, does develop significant transverse-tension membrane stresses after buckling because of the restraint provided by the boundary conditions at the unloaded edges. These membrane stresses act to restrain lateral motion, and thus the flat plate is capable of carrying loads beyond buckling, as indicated in Fig. 8.8.

For the axially compressed cylinder, the effect of the curvature is to translate the postbuckling path considerably downward, with the result that an inward type of buckling is observed to occur. This inward buckling causes superimposed transverse membrane stresses of a compressive nature, so that the buckle form itself is unstable.

As a consequence of the compressive membrane stresses, buckling of an axially compressed cylinder is coincident with failure and occurs

THIS PAGE INTENTIONALLY LEFT BLANK.

Tungsten Alloy

THIS PAGE INTENTIONALLY LEFT BLANK.

ATI Firth Sterling
Allegheny Technologies

1297 County Line Road, Madison, AL 35756

Date: 8 November 2006

To: Alpha-Omega Services, Inc.
GE Energy

Elevated Temperature Material Characterization

-- Summary of Findings --

Abstract

Summarized herein are the results of specific thermal property tests performed with SD180 as requested by the customer. Elevated temperature tensile testing of this alloy identified a gradual decrease in both offset yield strength and UTS with increasing temperature whereas the elongation at failure rose sharply and then leveled off. Thermal conductivity testing was inconclusive, as thermal testing firms now utilize laser flash diffusivity measurement, which has been shown to provide unreliable results for this material.

Background

ATI Firth Sterling tungsten heavy alloy (WHA) grade SD180 was selected for use in a new large scale design of gamma shield. This alloy has a nominal composition of 95W-3.57Ni-1.43Fe and a nominal density of 18.0 g/cc. The intensity of the gamma flux will result in significant heating of the shield, such that elevated temperature material properties are of significant interest. As a result, this application requires that the shielding material possess a multiplicity of attributes:

- adequate strength and ductility
- good γ radiation attenuation
- sufficient thermal conductivity

The customer specified the tests and the temperatures at which measurements should be made. Temperatures of interest were ambient, 200F, 400F, 600F, and 800F. Further, so as to match the application, testing was to be performed in air. As ATI Firth Sterling is presently equipped only for room temperature material characterization, elevated temperature testing was contracted out to two selected testing firms.

Experimental

Elevated Temperature Tensile Testing

Tensile Testing Metallurgical Lab (Cleveland, OH) was selected to perform the required elevated temperature tests. Tensile testing was conducted using ASTM E8 1" gauge length

specimens pulled at a constant speed of 0.05 in/min. The notch sensitivity of WHA precluded the use of scribe lines or grooves for positioning of a high temperature extensometer. Therefore, crosshead motion was used to generate the displacement measurements in this low compliance, lead screw testing machine. For comparison purposes, a pair of room temperature tensile tests was also performed at ATI Firth Sterling using the same test parameters but with a servohydraulic machine and extensometer. Two specimens were pulled for each test temperature. Averaged results are shown in Table 1.

Table 1. Summary of tensile testing results for SD 180 lot 1808..

Test Temperature	UTS (ksi)	0.2% YS (ksi)	EL (%)
RT (ATIFS)	114.0	93.9	5.0
RT (TTML)	109.7	94.3	3.5
200F (TTML)	112.4	70.8	15.5
400F (TTML)	105.2	60.2	21.8
600F (TTML)	98.2	51.9	21.9
800F (TTML)	95.4	47.8	21.6

The data pairs for each temperature exhibited good agreement, suggesting test results were free from anomalies.

Thermal Property Measurement

Anter Laboratories (Pittsburgh, PA) was selected for measurement of thermal diffusivity and specific heat at the various temperatures of interest. Anter specified that a single disk sample of 0.500" nominal diameter and 0.140" nominal thickness with parallel surfaces and known density be supplied. A SD180 sample from lot 1748 giving a measured ASTM B311 density of 18.11 g/cc was prepared and supplied by ATIFS. Measurements were conducted per ASTM E1461-01. Results are presented in Table 2.

Table 2. Summary of thermal property evaluation of SD 180 lot 1748.

Test Temperature		Diffusivity	Specific Heat	Conductivity
Nom. (F)	Actual (C)	(cm^2/sec)	(J/(kg-K))	(W/m-K)
RT	25	0.2742	154.7	76.8
200	97	0.2700	159.2	77.8
400	206	0.2624	163.4	77.6
600	316	0.2553	170.3	78.8
800	427	0.2451	173.9	77.2

The thermal conductivity remained relatively constant over the entire test temperature range, whereas specific heat showed a gradual increase and thermal diffusivity a slow decrease. The room temperature density was applied to all conductivity calculations, as the very low CTE of WHA (less than 5.0×10^{-6} K^{-1}) would result in a change of calculated value of only 0.5 W/m-K or less even at the highest test temperature. This was a factor of 4 less than the reported uncertainty of the test procedure.

Discussion of Results

In reviewing the tensile data set generated, the most pronounced effect was that of moving above the ductile to brittle test temperature (DBTT) for WHA, which in most metallurgical conditions is in the vicinity of room temperature. This accounts for the significant increase in alloy ductility, as measured by %EL. Accompanying this increase in ductility was a gradual decrease in both the ultimate and offset yield strengths, which is to be expected in light of induced thermal effects on various dislocation mechanisms that determine deformation response under load. These effects can be seen clearly when the data of Table 1 are plotted and displayed in Figure 1.

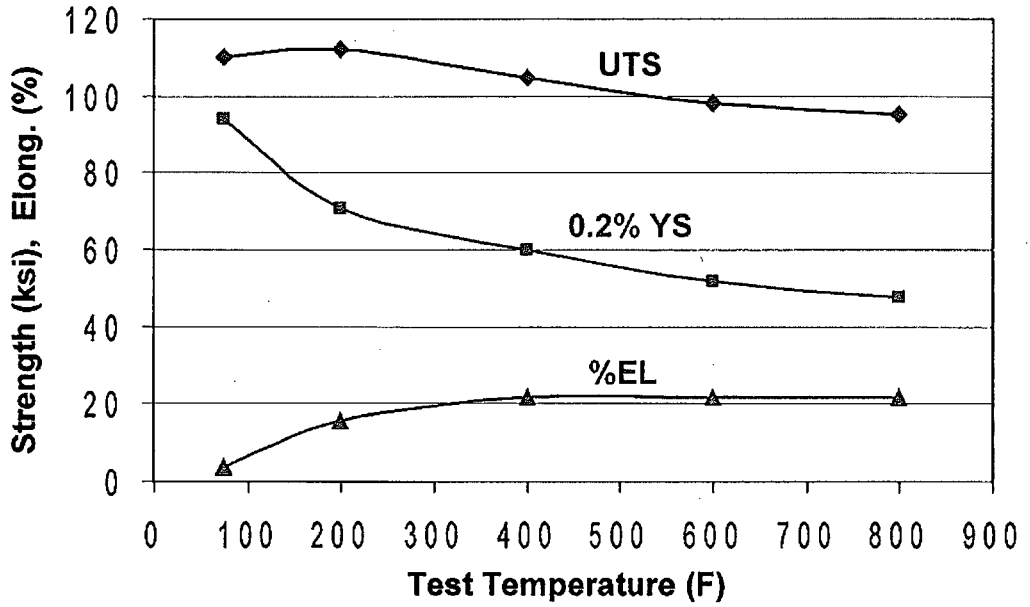

Figure 1. Graphical display of tensile property variation with test temperature.

While the strength of the gamma shield would decrease slightly with heating, the durability of the shield would tend to increase, depending on the magnitude of temperature rise attained.

The data set obtained from thermal property evaluation exhibited consistent trends. However, the resultant calculated values for thermal conductivity, which averaged 78 W/m-K, were well below the accepted industry values for this composition class of WHA. The literature for about two decades has reported values in the range of 110-130 W/m-K. This range is much more in keeping with an alloy having 95 wt.% of a metal that has a conductivity of ~160 W/m-K and is present as a virtually pure phase in the two phase WHA microstructure. The reason for the low measured values is presently unknown. The results obtained appear to underestimate the accepted thermal conductivity by about 35%. Dialogue with Anter revealed no apparent test execution problems. The data set obtained from Anter Laboratories did show that for the temperature range of interest, the thermal conductivity of the WHA, though of systematically low magnitude, did not vary significantly. It was decided that a second independent test be conducted in an effort to understand these results relative to industry accepted values.

Supplemental Testing

In view of the question posed from thermal conductivity testing of the SD180 alloy, a second test sample was prepared for submission to a different laboratory for analysis. While

Anter is nationally recognized for both thermal analysis and the manufacture of thermal analyzers, it was desirable to have a completely independent measurement made. Raul Pomares forwarded the firm of M & P Lab, in that they performed thermal measurements for GE Energy in the past. However, when their thermal analysis contact M. B. Bolduc was contacted, it was learned that they do not perform any thermal conductivity measurements. Harrop likewise, while performing other thermal measurements, does not perform conductivity measurement. Netzsch was therefore chosen as the second source for SD180 thermal conductivity measurement. Netzsch indicated that they also use the laser flash method per ASTM E1461 and calculate the thermal conductivity from measured diffusivity. After about a 6 week lead time, the room temperature test was completed and is shown in Table 3. Netzsch used a density of 18.0 g/cc for the calculation, whereas our measurement yielded 18.06 g/cc.

Table 3. Second conductivity evaluation of grade SD 180.

Test Temperature		Diffusivity	Specific Heat	Conductivity
Nom. (F)	Actual (C)	(mm^2/sec)	(J/(g-K))	(W/m-K)
RT	25	16.6	0.153	45.9

This new value for thermal conductivity was even further away from the expected value based on composition and density. This measurement underestimated the accepted average conductivity by at least 60%. After obtaining this margin of error, testing was halted, as any elevated temperature values would likewise be of no value.

Conclusions

The selected elevated temperature characterization of SD180 provided a more comprehensive prediction of alloy performance in the target application. The identified property trends were in keeping with fundamental elevated temperature response of metallic materials. Excellent ductility was retained over the entire range of test temperature.

Thermal conductivity measurements however were inconclusive. Two independent tests – both using nationally recognized testing firms that not only routinely perform toll thermal testing but also actually manufacture the equipment – failed to provide results that were even in approximate agreement or close to the accepted values used for decades within the refractory metals industry. These low values should therefore be disregarded, as they cannot be independently repeated. As the entirety of this testing was conducted off site, the reasons for this extreme variation in measurements are presently unknown. Both testing houses guarantee conformance to ASTM E1461. Whatever the case, those skilled in performing laser flash tests have not demonstrated that this technique, now used almost universally for thermal conductivity measurements, is appropriate for tungsten heavy alloy. To the contrary, conductivity measurements obtained to date suggest the flash diffusivity approach is unreliable for this material. The higher industry accepted values of 110-130 W/m-K were no doubt made by techniques that predated laser flash diffusivity and measured conductivity directly using larger size samples. No presently available source for repeating earlier test methods is known.

S. G. Caldwell
Technical Director – Tungsten Alloys

ATI Firth Sterling
Allegheny Technologies

1297 County Line Road, Madison, AL 35756

DISREGARD DUPLICATE PAGE BAR 60CT10

Date: 8 November 2006

To: Alpha-Omega Services, Inc.
GE Energy

Elevated Temperature Material Characterization

-- Summary of Findings --

Abstract

Summarized herein are the results of specific thermal property tests performed with SD180 as requested by the customer. Elevated temperature tensile testing of this alloy identified a gradual decrease in both offset yield strength and UTS with increasing temperature whereas the elongation at failure rose sharply and then leveled off. Thermal conductivity testing was inconclusive, as thermal testing firms now utilize laser flash diffusivity measurement, which has been shown to provide unreliable results for this material.

Background

ATI Firth Sterling tungsten heavy alloy (WHA) grade SD180 was selected for use in a new large scale design of gamma shield. This alloy has a nominal composition of 95W-3.57Ni-1.43Fe and a nominal density of 18.0 g/cc. The intensity of the gamma flux will result in significant heating of the shield, such that elevated temperature material properties are of significant interest. As a result, this application requires that the shielding material possess a multiplicity of attributes:

- adequate strength and ductility
- good γ radiation attenuation
- sufficient thermal conductivity

The customer specified the tests and the temperatures at which measurements should be made. Temperatures of interest were ambient, 200F, 400F, 600F, and 800F. Further, so as to match the application, testing was to be performed in air. As ATI Firth Sterling is presently equipped only for room temperature material characterization, elevated temperature testing was contracted out to two selected testing firms.

Experimental

Elevated Temperature Tensile Testing

Tensile Testing Metallurgical Lab (Cleveland, OH) was selected to perform the required elevated temperature tests. Tensile testing was conducted using ASTM E8 1" gauge length

When the reported unit of measure is converted from a gram to kilogram basis, this supplemental testing by a second independent testing house yielded excellent agreement in specific heat – a value of 153 compared to the earlier 154.7 (J/[kg-K]). These values were thus in agreement within ~1.1% - an excellent match for single test data comparison.

In examining Section 15 of NUREG/CR-6150, it is not surprising to find disagreement in specific heat values to those we reported – it is rather to be expected. Tables 15-1 and 15-2 both list date for pure, elemental tungsten (W) – not tungsten heavy alloy. The SD180 alloy additionally contains Fe and Ni, and possesses a lower theoretical alloy density that pure W.

The relevance of previously reported specific heat values for the SD180 used in the aforementioned project over those contained in the cited NUREG document can therefore be summarized as follows:

1. NUREG/CR-6150 does not even relate to the tungsten heavy alloy used in the cask project.
2. NUREG/CR-6150 contains calculated values only, whereas our reported values were from actual material testing conducted by equipment manufacturers to an ASTM standard.
3. The thermodynamic data used for computation of NUREG/CR-6150 data are not given in Section 15. Even for the case of pure W, the calculated density reported in NUREG/CR-6150 Section 15.3 is 19.600 g/cc, which is greater than the tungsten industry accepted value of 19.3 g/cc for W as well as the value of 19.30 g/cc specified in the National Institute of Standards Physical Reference Data listing. It would appear that at least that input datum used in thermal calculations is in slight error even for the case of pure W. Calculated data are only as good as the input data and model.
4. Specific heat values we reported previously accounted for the actual measured density of the SD180 tungsten heavy alloy, as was determined using ASTM B311. As both chemical makeup and density varied from that of pure W, it is only natural that the thermal properties would differ from pure W as well.
5. The values we reported from Anter and Netzsch tests are consistent in trend with data for pure W in Table 15-1 of NUREG/CR-6150. For example, room temperature specific heat for pure W is listed as ~138 J/(kg-K), whereas testing of SD180 gave ~155 J/(kg-K) – an increase of ~12%. The tungsten heavy alloy contained 5 wt.% of transition metals having significantly higher specific heats than W (~460 J/(kg-K) for Ni, ~440 J/(kg-K) for Fe). It is therefore only expected that the room temperature specific heat for the SD180 heavy alloy would be higher than that of pure W.

There is therefore no reason whatsoever to question the specific heats reported by ATI Firth Sterling for SD180 based on NUREG/CR-6150. At best, the cited Section 15 data are not applicable for the reasons described above. Please contact me if further information is needed.

Yours truly,

Steven G. Caldwell

Steven G. Caldwell, Ph.D.
R&D Director
ATI Firth Sterling
1297 County Line Road
Madison, AL 35756

ATI Firth Sterling
Allegheny Technologies

Tungsten Heavy Alloy

Engineering Manual

S. G. Caldwell, PhD

ATI Firth Sterling
1297 County Line Road
Madison, AL 35756
ph 888-778-0979
fax 888-208-9109

www.firthsterling.com

2. Alloy Selection Criteria

Density

Density is the single most important property that makes a WHA the material of choice for virtually all applications. The selection of a specific composition for a given density application may ultimately be made on the basis of mechanical property requirements in conjunction with sintering considerations, unless a density is mandatory.

As is true with most mechanical designs, the optimum design is the one that adequately addresses all critical parameters and offers the best compromise of the remaining options. As the density of a WHA is increased, the available ductility decreases. Alloy density varies according to tungsten content, as can be seen in the following table of ATI Firth Sterling standard alloys. These alloys conform to the various classes as defined by industry standard MIL-T-21014D (alternately AMS-T-21014 and ASTM B777).

Grade Specification Conformance

Alloy*	Nom. Composition (Wt. %)	MIL-T-21014D Classification	Typical Density (g/cc)	Typical Density (lbs/in^2)	Magnetic Permeability (μ)
SD170	90W-7.14Ni-2.86Fe	Class 1	17.09	0.618	5.0-5.5
Dens21	89.8W-8.92Ni-1.28Fe	Class 1	17.16	0.620	<1.01
SD175	92.5W-5.36Ni-2.14Fe	Class 2	17.62	0.637	4.5-5.0
Dens23	92.5W-6.56Ni-0.94Fe	Class 2	17.67	0.639	<1.01
SD180	95W-3.57Ni-1.43Fe	Class 3	18.12	0.655	4.0-4.5
Dens25	95W-4.37Ni-0.63Fe	Class 3	18.16	0.656	<1.01
SD185	97W-2.14Ni-0.86Fe	Class 4	18.56	0.671	1.6-2.0

Dens21 is manufactured with a tungsten content slightly under the nominal in order to have a sintered density positioned more centrally within the defined interval. In addition to these standard compositions, ATI Firth Sterling can also manufacture custom alloys.

Mechanical Properties

Mechanical properties of modern WHAs far surpass those available from WHAs even a few decades ago. Three factors primarily contribute to this advance: (1) higher purity raw materials, (2) cleaner and more precisely controlled process environments, and (3) the use of modern tungsten-nickel-iron (W-Ni-Fe) compositions rather than the older alloys containing copper.

It is also important to note as a general consideration that the maximum attainable property set for these alloys varies with the size of the blank. This is a direct consequence of the nature of the sintering operation used to make the parts. A number of gradients – thermal, chemical, and gravitational – exist during sintering. As the maximum section thickness of a given part is increased, thermochemical removal of impurities from the center of the pressed part prior to surface pore closure becomes more difficult. Therefore, small parts will always tend to have higher mechanical properties than larger ones.

As seen in the table below, the nominal properties listed meet or exceed the industry standard requirements. All values shown are for material in the as-sintered state, as this is the most commonly supplied condition of the material for commercial applications.

Typical Densalloy™ Properties

Alloy*	Wt.% W (nominal)	UTS (ksi)	0.2% YS (ksi)	EL (%)	Elastic Modulus (x 10^6 psi)	Hardness (HRC)
SD170	90	120	80	10	45	28
Dens21	90	110	75	4	45	28
SD175	92.5	120	80	8	48	28
Dens23	92.5	110	80	3	48	28
SD180	95	120	75	6	50	29
Dens25	95	110	75	3	50	29
SD185	97	110	75	2	52	30

All WHAs are susceptible to hydrogen embrittlement, which lowers the ductility of the alloy. ATI Firth Sterling can provide alloys in a hydrogen outgassed condition, which in some cases can double the tensile elongation. Further property enhancement is possible through additional post-sinter processing.

For structural (load bearing) applications, it is recommended that alloy be used in the most ductile condition feasible for the given part. This promotes "bend before break" behavior needed for critical parts. Part durability is favored by use of lower tungsten content Class 1 and 2 alloys such as SD170 and SD175.

Thermal and Electrical Properties

The properties of WHA are governed by the properties of its principal constituent, tungsten. While properties will vary slightly with tungsten content, binder composition, and microstructure, several example properties will be cited for SD180, as it is near the middle of the commercially defined compositional range.. The thermal conductivity of the alloy is ~80 W/m-°K and a corresponding electrical conductivity of ~13% IACS. The thermal expansion is very low, with a CTE of only ~5.0E-6/°C at 20°C – only about 1/3 that of ferrous alloys. The specific heat of SD180 at room temperature is ~0.037 cal/g-°C. While the melting point of pure tungsten is extremely high, WHAs will begin to form a liquid phase when heated in excess of ~1450°C (2642°F). Therefore, unlike pure W, WHAs are not suitable for high temperature applications.

The change in tensile properties of WHA at elevated temperature is of increasing interest to oilfield engineers. As drilling depths approach 5 miles, there is growing interest in the ability of WHA components to survive the harsh pressure and elevated temperature conditions. The following graph shown below illustrates the systematic change in mechanical properties with temperature for vacuum annealed SD175 typical of what that industry uses. For applications in which the service temperature will exceed ~300°C, slight surface oxidation will occur in air. A protective atmosphere should be considered for prolonged exposure at or above this temperature. It is important to note that at service temperatures exceeding ~500°C – beyond the range of the data shown below – WHA

THIS PAGE INTENTIONALLY LEFT BLANK.

Tungsten

Properties, Chemistry, Technology of the Element, Alloys, and Chemical Compounds

Erik Lassner and
Wolf-Dieter Schubert
Vienna University of Technology
Vienna, Austria

Kluwer Academic / Plenum Publishers
New York, Boston, Dordrecht, London, Moscow

Library of Congress Cataloging-in-Publication Data

Lassner, Erik.
Tungsten : properties, chemistry, technology of the element, alloys, and chemical compounds / Erik Lassner and Wolf-Dieter Schubert.
p. cm.
Includes bibliographical references and index.
ISBN 0-306-45053-4
1. Tungsten. I. Schubert, Wolf-Dieter. II. Title.
QD181.W1L37 1998
620.1'8934--dc21 98-45787
CIP

ISBN 0-306-45053-4

233 Spring Street, New York, N.Y. 10013

10 9 8 7 6 5 4 3 2 1

A C.I.P. record for this book is available from the Library of Congress.

Printed in the United States of America

Significant strengthening is observed up to 2700 K (2427 °C). Above this, rapid particle coarsening occurs, and the strengthening effect fades. Additions of rhenium provide ductility at low temperatures by decreasing the DBTT.

W–Re–HfC alloys cannot be produced by powder metallurgical techniques owing to the high oxygen affinity of hafnium. They are produced by arc melting.

Yield strength and ultimate tensile strength of a W–3.6Re–0.26HfC alloy as a function of temperature are shown in Fig. 6.12, in comparison to pure W, W–3.6Re, and W–3.6Re–1ThO_2.

W–Re–HfC alloys are the strongest man-made metallic materials at temperatures above 2000 K [6.25].

6.3. TUNGSTEN COMPOSITES

Tungsten metal exhibits outstanding thermal properties, which makes it attractive for a broad range of applications. However, for certain applications, its electrical and thermal conductivity, sensitivity toward oxidation, and poor workability are unsatisfactory. These limitations have led to the development of two-phase alloys, in which the useful properties of tungsten are combined with those of the additive.

Two important alloy systems belong to this group and are described below:

- The so-called heavy metal alloys, based on W–Ni–Fe and W–Ni–Cu–(Fe). They are used wherever high density, excellent mechanical properties, and good workability are required.
- W–Cu and W–Ag alloys, in which the high electrical and thermal conductivity of copper or silver is combined with the high hardness and wear resistance of tungsten.

6.3.1. *Tungsten Heavy Metal Alloys* [6.1, 6.2, 6.26, 6.27, 6.29]

The term *tungsten heavy metal* or *heavy metal* is used for a group of two-phase composites, based on W–Ni–Fe and W–Ni–Cu. They are characterized by a high density and a novel (unique) combination of strength and ductility.

Tungsten is the main component of the alloys (typically present in the range of 90 to 98 wt%) and the reason for their high density (between 17 and 18.5 g/cm^3). Nickel, iron, and copper serve as a binder matrix, which holds the brittle tungsten grains together and which makes the alloys ductile and easy to machine. A typical microstructure is shown in Fig. 6.13. It consists of spherical tungsten grains (20 to 60 µm in diameter), which are embedded in a tough, metallic matrix. While the grains are nearly pure bcc tungsten, the fcc binder matrix contains about 20 wt% W in solid solution.

Heavy metals are used for applications, where the high specific weight of the material plays an important role. They are used as counterweights, rotating inertia members, X-ray and γ-radiation shields, as rigid tools for machining, as well as for defense purposes (kinetic energy penetrators, fragmentation devices, etc.).

Fabrication [6.26, 6.27]. Heavy metals are produced by conventional P/M techniques. A flow chart of the fabrication process is shown in Fig. 6.14. Elemental powders (W,

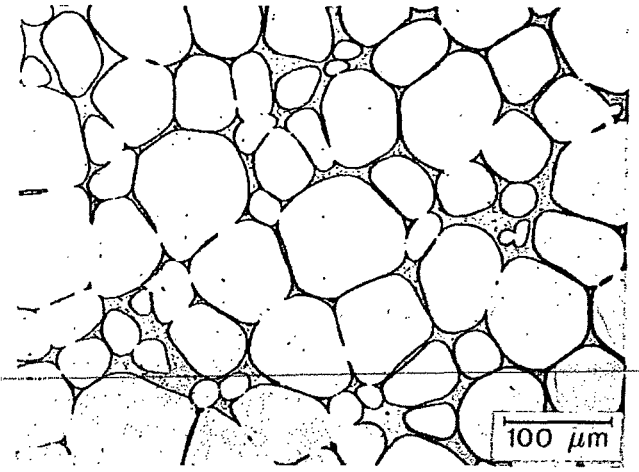

FIGURE 6.13. Optical micrograph of a 95 wt% tungsten heavy metal alloy with 3.2 wt% Ni and 1.8 wt% Cu. By courtesy of Plansee AG, Reutte, Austria.

Fe, Ni, Cu) are blended in mixers or ball mills to the desired ratio, compacted to form a green body, and subsequently liquid-phase sintered. Assuming proper manufacturing conditions, they exhibit full or near-theoretical density in the as-sintered condition.

Powder particle sizes are in the range of 2 to 6 μm. Both die pressing and isostatic pressing (dry- and wet-bag pressing) are in use. No lubricant is commonly added, since the green strength is high enough to handle the compacts. Powder injection molding (PIM) is used for applications where net shaping is desired and large quantities of complex parts are produced [6.28].

Sintering is commonly carried out in molybdenum-wire resistance-heated furnaces under hydrogen or nitrogen mixtures (dissociated ammonia) but can also be performed in vacuum units. The use of wet hydrogen has become industrial practice to suppress hydrogen embrittlement (water vapor porosity) [6.29]. The temperature/time program of the sintering cycle must be adjusted to the composition and size of the sintered parts. A

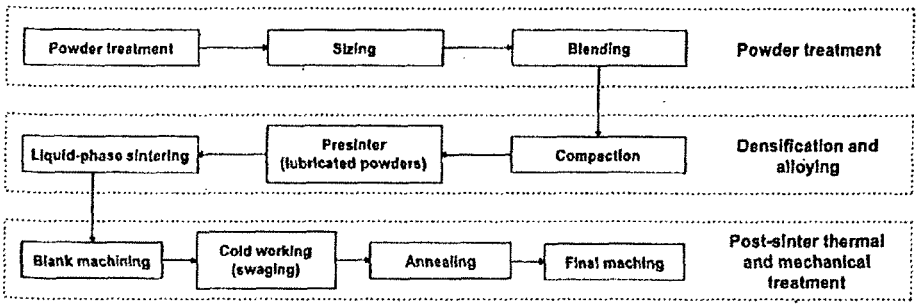

FIGURE 6.14. Flowchart of the fabrication process of tungsten heavy metal penetrators [6.26].

cleaning step in hydrogen at 1000 °C is commonly performed to render the outgassing of volatile compounds. High-purity powder grades must be used for sintering. Otherwise, blistering will occur on liquid-phase sintering, and interface precipitations will occur on cooling.

Isothermal sintering is carried out above the eutectic temperature, typically between 1440 and 1500 °C, but can be as high as 1600 °C. The higher the tungsten content of the alloy, the higher the temperature. Tungsten–nickel–copper alloys are sintered at somewhat lower temperatures than tungsten–nickel–iron alloys. Sintering times are between 30 minutes and two hours. Prolonged sintering under dry hydrogen leads to swelling of the parts and significant embrittlement due to pore coarsening by Ostwald ripening and coalescence. Residual porosities larger than 0.5% drastically reduce the ductility [6.30, 6.31].

On cooling, a significant amount of tungsten remains in solid solution, depending on the binder composition and the cooling rate. The solubility is highest in binary W–Ni alloys (up to 40 wt%; resulting in low ductility), but additions of Fe and Cu depress it to lower values (typically 20 to 25 wt% W), providing a tough and ductile binder matrix.

Shrinkage porosity can form on cooling, in particular in W–Ni–Cu alloys and at high cooling rates; furthermore, impurities (P, S, C) segregate at the tungsten matrix interface. Both effects must be controlled by proper manufacturing conditions, since they significantly lower the ductility.

Optimal mechanical properties require subsequent heat treatment of the alloys. Solution annealing at 900 to 1300 °C and subsequent quenching to avoid impurity segregation and formation of intermetallic phases significantly improves ductility [6.26]. Heavy metals can be cold-worked (swaged, rolled) to increase hardness and strengths at the expense of elongation and toughness. Aging at 500 °C after 25% deformation (cold work) is a compromise to achieve both high ultimate tensile strengths and elongation. Conventional procedure is a double swaging–heat treatment cycle (deformation 25–30%) [6.32]. The structure shows that the original spheroids formed during liquid-phase sintering have been transformed to ellipsoids on deformation (Fig. 6.15). Recently, the advantage of large deformation levels (up to 95%) yielding in a fibrous microstructure (Fig. 6.16) has been demonstrated [6.32]. Heavy metals exhibit a ductile-to-brittle transition temperature. In comparison to pure tungsten it is, however, not a sharp transition but spreads over several hundred degrees [6.1].

Although a considerable amount of densification already occurs during solid-state heating, isothermal liquid-phase sintering is a prerequisite to obtain near-theoretical density and a high degree of microstructural homogeneity. Rapid final densification occurs on formation of the liquid phase under the action of capillary forces. Particle rearrangements, solution/reprecipitation processes (Ostwald ripening), and coalescence contribute to a higher packing density and a significant grain coarsening during sintering. The original tungsten powder grain size of 3–5 μm is transformed during sintering to rounded tungsten particles (spheroids) of at least 10 times the original grain diameter. Shape accommodation (formation of polyhedras with rounded corners) plays an important role in high tungsten alloys, where only a small quantity of liquid is available for achieving full density.

Depending on the binder composition, heavy metals can be classified into two main groups [6.2, 6.27]:

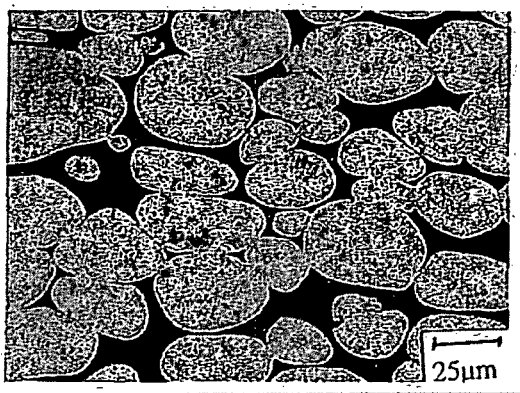

FIGURE 6.15. Microstructure of a W–Ni–Fe–Co alloy after swaging by 30% [6.32]. By courtesy of A. R. Bentley, M. C. Hogwood, and M. Power, Defence Research Agency, Kent, England.

(a) W–Ni–Fe (Ni: 1–7 wt%, Fe: 0.8–3 wt%, Mo: 0–4 wt%)

This group is ferromagnetic. Typical nickel-to-iron ratios range between 1:1 and 4:1. The preferred ratio is 7:3, since this composition avoids the formation of intermetallic phases [6.26]. W–Ni–Fe alloys exhibit excellent strength/ductility combinations and can be cold-worked to a reduction of 60% without intermediate annealing. Molybdenum acts as grain refiner. Higher additions of iron and/or additions of molybdenum cause a significant matrix-strengthening effect and improve high-temperature strength (Gyromet grades) [6.2]. Other additives, such as Co, Ta, and Re, act as grain refiners and increase hardness and strength, but lower the ductility [6.29]. Rhenium additions are of interest in net-shape production, since their high strength in the as-sintered condition (1180 MPa) does not require any post-sintering treatment [6.33].

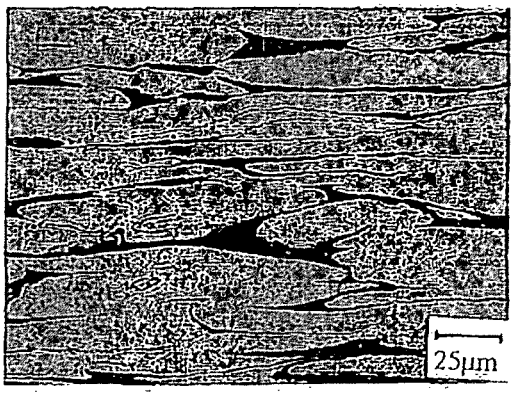

FIGURE 6.16. Microstructure of a W–Ni–Fe–Co alloy after deformation by 80% [6.32]. By courtesy of A. R. Bentley, M. C. Hogwood, and M. Power, Defence Research Agency, Kent, England.

(b) W–Ni–Cu (Ni: 1–7wt%, Cu: 0.5–3 wt%, Fe: 0–7 wt%)

Members of this group are nonmagnetic and exhibit a higher electrical conductivity. The nickel-to-copper ratio ranges from 3:2 to 4:1. W–Ni–Cu alloys exhibit lower strength and ductility than comparable W–Ni–Fe alloys. Due to the low melting point of copper, low heating rates are required to obtain full density.

Properties: [6.1, 6.34, 6.35]. Some properties of tungsten heavy metal alloys are summarized in Table 6.1. Ultimate tensile strengths (660–1350 MPa), yield strengths (565–300 MPa), and fracture elongations (5–30%) can vary widely. In general, mechanical properties are very sensitive to processing conditions, impurities, and microstructure. Problems with controlling porosity, impurities, and microstructural homogeneity are therefore common in heavy alloy fabrication [6.31]. Residual sinter porosity and the formation of interface precipitates are the main reason for inferior material properties.

With increasing tungsten content, the contiguity of the tungsten grains increases (i.e., the W–W interfacial area as a fraction of the total interface area) and both strength and ductility decrease [6.36]. This "microstructural limitation" of the properties is demonstrated in Fig. 6.17 for alloys of different tungsten contents [6.1, 6.31, 6.37]. While the

TABLE 6.1. Properties of Tungsten Heavy Metal Alloys[a]

Properties	1	2	3
Density ($g \cdot cm^{-3}$)	17.0–18.5	17.0–18.5	17.1–18.6
Young's modulus (GPa)	350–400	320–380	—
Shear modulus (GPa)	—	125–160	—
Poisson's ratio	0.28–0.29	0.28–0.29	—
Hardness			
HV10	270–360	270–470	—
HB30	—	250–450	—
RC	—	—	28–40
Tensile strength (MPa)			
20 °C	870–1000	660–1350	880–1320
100 °C	—	560–730	—
500 °C	340–650	340–610	—
1000 °C	220–260	90–260	—
Yield strength (0.2%) (MPa)	600–700	565–1300	750–1240
Fracture elongation (%)	10–30	—	5–30
Compressive strength (MPa)	3500–4500	3500–5500	—
K_{ic} ($MPa \cdot mm^{-1}$)	800–6300	—	—
Compressibility (% of length)	—	—	45–60
Charpy value (notched)	0.9–2.8	—	—
Specific electrical resistivity ($\mu\Omega \cdot m$)	0.10–0.18	0.10–0.18	—
Mean linear coefficient of thermal expansion at 20–800 °C ($mm^{-1} \cdot K^{-1}$)	$5.2–6.5 \times 10^{-6}$	$5.2–6.5 \times 10^{-6}$	—
Half-value thickness			
against ^{60}Co	—	8.5–9.7	—
against ^{137}Cs	—	4.5–5.2	—

[a] 1. Pink and R. Eck, "Refractory Metals and their Alloys," in: *Materials Science and Technology* (R. W. Cahn, P. Haasen, and E. J. Kramer, eds.), Vol. 8, pp. 591–638, VCH, Weinheim, (1996).
2. Metallwerk Plansee, Densimet Schwermetall Legierungen, Company Brochure, Reutte, Austria (1982).
3. Ashot Ashkelon, Tungsten-Based Products, Company Brochure.

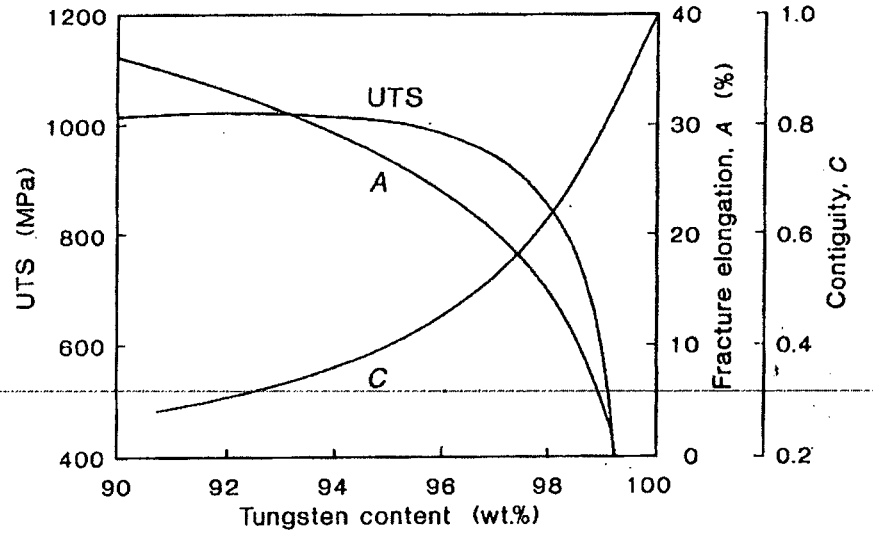

FIGURE 6.17. Optimum values of room-temperature strength and fracture elongation and their correlation with the contiguity factor for tungsten heavy alloys [6.1, 6.31].

trend is most pronounced for the fracture elongation, the tensile strength exhibits a maximum at about 85 vol% W (93 wt%) before it significantly decreases. At 99 wt% W, the elongation is zero and the tensile strength is about 400 MPa [6.38].

Recently, it was demonstrated that large deformation levels yield exceptionally high tensile strength levels (up to 1700 MPa), combined with fracture elongations above 15% [6.32].

Besides the high density and the unique combination of high strength and ductility, there are other attributes which make heavy metals a versatile product:

- the high modulus of elasticity (much higher than steel),
- excellent vibration damping characteristics (for chatter-free heavy machining),
- its good machinability,
- the high absorption ability for X-rays and γ-rays,
- good thermal and electrical conductivity,
- low electrical erosion and welding tendency,
- good corrosion resistance.

Research in tungsten heavy alloys was previously boosted by the ballistic application as anti-amor kinetic energy penetrator. Numerous papers have appeared in the last years and reviews have recently been published [6.29, 6.39, 6.40]. Although the basic requirements are the same for civil as for defense applications (i.e., high density, strength, and elongation), there are two more important factors which must be considered for this specific application: the behavior of the material under high strain rate conditions and their ballistic performance (i.e., their penetration ability). In particular, the latter aspect is of critical importance and, to a certain extent, still a weak point of heavy metals. Their ballistic performance is inferior compared to depleted uranium, which is still used as a

standard penetrator material [6.29]. Nevertheless, recent environmental considerations have put a strong emphasis on substituting depleted uranium by heavy metals because of its radioactivity. Efforts to improve the ballistic performance through proper processing and compositional modifications have failed [6.29, 6.39]. Recent research has therefore focused on alternative matrix alloys, such as tungsten–hafnium, tungsten–uranium composites [6.29], or heavy metal alloys with a spiculating core of WC [6.41].

6.3.2. Tungsten Copper and Tungsten Silver [6.1, 6.2, 6.42].

Tungsten–copper and tungsten–silver composites are widely used in mechanical and electrical engineering. Typical applications include high-, medium-, and low-voltage circuit breakers (W–Cu, W–Ag), resistance welding electrodes, electrode materials for electrical discharge machining, and heat sink materials for microelectronic packaging (W–Cu). More recently, W–Cu composites have been tested as heat flux components in experimental fusion reactors [6.43] and as materials in MHD (magnetohydrodynamics) power generation systems [6.44].

They combine the high hardness, hot strength, and wear resistance of tungsten with the outstanding electrical and thermal conductivity of the two high-conductivity metals. Furthermore tungsten increases the resistance of the materials against spark and arc erosion (burn-off) and lowers the sticking and welding tendency, which are both important criteria for heavy-duty electrical contacts, where switching currents can be up to 100 kA and arc temperatures of a few 10,000 K can occur within a few milliseconds [6.45]. Under arcing conditions, the contacts are cooled through the melting and evaporation of silver or copper ("transpiration" cooling), an effect which was earlier used for rocket nozzle throat liners (for example for underwater-launched ballistic missiles) made of W–Ag [6.2].

W–Cu and W–Ag composites are not real alloys in the strict meaning of the word, because the mutual solubility of the components is practically zero. Therefore, they are also sometimes called "pseudoalloys."

Production. Powder metallurgy is the only viable way to produce composites of high quality. The method of production depends on the composition ratio. Materials with 10 to 40 wt% copper (20 to 50 wt% silver) are commonly produced by infiltration, while at higher copper or silver contents the powders are blended, pressed, and subsequently solid-state sintered [6.42, 6.46].

Infiltration of porous structures. A porous tungsten skeleton is first produced by pressing either pure tungsten powder or a mixture of tungsten powder and small amounts of the additive element with subsequent sintering in a reducing atmosphere at comparably low temperatures (1200–1800 °C). The porosity of the compact can be varied by the pressing and sintering parameters, as well as by the grain size distribution of the starting tungsten powder. It determines the percentage of infiltrate. For higher copper and silver contents, loose tungsten powder can also be infiltrated.

Infiltration is accomplished by immersion, dipping, or flooding, either in vacuum, inert gas, or, preferably, in reducing atmosphere at 1150–1250 °C. Oxide layers disturb the infiltration process and must be removed prior to infiltration by reduction with hydrogen. Trace impurities can impair the wetting between tungsten and the melt (for example, silicon) but can also improve it (nickel, cobalt, iron) [6.47]. Densities of 96% up to near-

FIGURE AND TABLE NO. 58R. RECOMMENDED VALUES FOR THERMAL LINEAR EXPANSION OF TUNGSTEN W

RECOMMENDED VALUES

[Temperature, T, K; Linear Expansion, $\Delta L/L_0$, %; α, K^{-1}]

T	$\Delta L/L_0$	$\alpha \times 10^6$
5	-0.086	0.0006
25	-0.086	0.21
50	-0.085	0.88
100	-0.076	2.6
200	-0.040	4.1
293	0.000	4.5
400	0.048	4.5
500	0.093	4.6
600	0.140	4.7
700	0.188	4.8
800	0.237	5.0
900	0.287	5.0
1000	0.339	5.2
1200	0.444	5.3
1400	0.551	5.4
1600	0.661	5.6
1800	0.774	5.8
2000	0.893	6.1
2200	1.020	6.6
2400	1.157	7.1
2600	1.307	7.8
2800	1.469	8.3
3000	1.646	9.2
3200	1.837	10.0
3400	2.042	10.8
3600	2.263	11.6

REMARKS

The tabulated values are considered accurate to within ±3% over the entire temperature range. These values can be represented approximately by the following equations:

$$\Delta L/L_0 = 4.266 \times 10^{-4} (T - 293) + 8.479 \times 10^{-8} (T - 293)^2 - 1.974 \times 10^{-11} (T - 293)^3 \qquad (293 < T < 1395)$$

$$\Delta L/L_0 = 0.548 + 5.416 \times 10^{-4} (T - 1395) + 1.952 \times 10^{-8} (T - 1395)^2 + 4.422 \times 10^{-11} (T - 1395)^3 \qquad (1395 < T < 2495)$$

$$\Delta L/L_0 = 1.226 + 7.451 \times 10^{-4} (T - 2495) + 1.654 \times 10^{-7} (T - 2495)^2 + 7.568 \times 10^{-12} (T - 2495)^3 \qquad (2495 < T < 3600)$$

General Plastics LAST-A-FOAM

THIS PAGE INTENTIONALLY LEFT BLANK.

GENERAL PLASTICS

LAST-A-FOAM® FR-3700

FOR

CRASH & FIRE PROTECTION

OF

NUCLEAR MATERIAL

SHIPPING CONTAINERS

GENERAL PLASTICS MANUFACTURING COMPANY
4910 BURLINGTON WAY/ P O BOX 9097 TACOMA, WA 98409
(253) 473-5000, Fax 253-473-5104, Email: engineering@generalplastics.com

TABLE OF CONTENTS

INITIAL ISSUE 4/91, REPRINTED 5/91, 11/91, 9/92, 12/93, 6/95, 2/97, 6/97, 3/98,2/99 , 3/01, 10/03
*(new or revised)

LAST-A-FOAM ® FR-3700
DYNAMIC CRUSH STRENGTH (PSI)
and ENERGY ABSORPTION (FT -LB./CU.IN.
@ 75°F, PARALLEL TO RISE

	CRUSH %													
DENSITY	10		20		30		40		50		60		65		70	
3	100	0	83	1	81	2	78	3	81	3	85	4	96	4	106	5
4	145	1	124	2	124	3	123	4	130	5	143	6	167	7	186	7
5	193	1	170	2	172	4	174	5	188	7	215	8	257	9	288	10
6	244	1	220	3	225	5	231	7	255	9	300	11	365	12	412	14
7	298	1	274	4	282	6	294	8	329	11	397	14	491	16	558	18
8	353	1	331	4	343	7	361	10	411	13	507	17	635	19	725	22
9	411	2	390	5	408	8	434	12	500	16	628	20	797	23	914	27
10	471	2	453	6	477	10	512	14	595	18	761	24	977	28	1124	32
11	627	3	593	8	618	13	660	18	763	24	984	31	1275	36	1468	42
12	736	3	699	9	730	15	785	21	912	28	1186	37	1549	43	1774	50
13	854	4	815	11	851	17	920	25	1075	33	1409	43	1853	50	2112	59
14	979	4	938	12	980	20	1066	29	1252	38	1653	50	2187	58	2482	68
15	1112	5	1070	14	1118	23	1223	33	1442	44	1918	58	2552	67	2884	78
16	1253	5	1209	15	1265	26	1391	37	1647	50	2203	66	2949	76	3320	89
17	1402	6	1357	17	1420	29	1569	41	1865	56	2510	74	3377	86	3788	101
18	1558	6	1513	19	1584	32	1758	46	2097	62	2839	83	3836	97	4290	114
19	1722	7	1677	21	1757	36	1958	51	2344	69	3189	92	4332	108	4826	127
20	1893	8	1849	23	1938	39	2168	56	2604	76	3561	102	4858	119	5397	141
21	2072	9	2029	26	2127	43	2389	62	2879	84	3955	112	5419	132	6002	156
22	2258	9	2217	28	2325	47	2621	68	3166	92	4371	123	6013	145	6641	171
23	2452	10	2413	30	2531	51	2863	74	3471	100	4810	134	6642	158	7316	187
24	2653	11	2616	33	2745	55	3116	80	3788	109	5271	146	7306	172	8027	204
25	2861	12	2828	36	2968	60	3380	86	4119	117	5755	159	8004	187	8773	222
26	3076	13	3047	38	3199	64	3654	93	4465	127	6262	171	8738	203	9555	241
27	3298	14	3274	41	3438	69	3939	100	4825	136	6792	185	9508	219	10374	260
28	3527	15	3509	44	3686	74	4235	107	5199	146	7344	199	10314	235	11229	280
29	3764	16	3751	47	3941	79	4541	114	5588	157	7920	213	11157	253	12120	301
30	4007	17	4001	50	4205	84	4858	122	5991	167	8520	228	12036	271	13049	323

Note: Crushing into shaded area not recomended. Energy Bold, Stress Plain Text.

THIS PAGE INTENTIONALLY LEFT BLANK.

Port Seal

THIS PAGE INTENTIONALLY LEFT BLANK.

MATERIAL REPORT

REPORT NUMBER: KK2206
DATE: 06/19/96

TITLE: Evaluation of Parker Compound S1224-70 to ASTM D2000 7GE705 A19 B37 EA14 EO16 E036 F19 G11

PURPOSE: To determine if S1224-70 meets the callout.

CONCLUSION: Compound S1224-70 meets the ASTM D2000 callout.

Recommended temperature limits: -65^0F to 450^0F

Recommended For
Dry heat
Some petroleum oils
Moderate water resistance
Fire resistant hydraulic fluids (HFD-R and HFD-S)
Ozone, aging, and weather resistance
Low temperature

Not Recommended For
Ketones
Acids
Silicone oils
Auto and aircraft brake fluid

Parker O-Ring Division
2360 Palumbo Drive
Lexington, Kentucky 40509
(859) 269-2351

Compound Data Sheet
Parker O-Ring Division United States

REPORT DATA

Report Number:	KK2206

	ASTM D2000 **7GE705 A19 B37 EA14 EO16 E036 F19 G11** Pass / Fail Limits	**S1224-70** Slab Results
Basic Physical Properties		
Hardness	70 +/- 5	69
Tensile Strength, psi min	725	1204
Elongation, % min	150	265
ASTM D573 Heat Aging, 70 HRS @ 225°C		
Hardness Change, pts max	+10	+6
Tensile Change, % max	-25	-14
Elongation Change, % max	-30	-26
Compression Set ASTM D395, 22 HRS @ 347°F, plies		
% of Original Deflection, max	30	23
Fluid Immersion, ASTM #1 Oil, 70 HRS @ 150°C		
Hardness Change, pts	0 to -15	-9
Tensile Change, % max	-20	+10
Elongation Change, % max	-20	+3
Volume Change, %	0 to +15	+4
Fluid Immersion, ASTM #3 Oil, 70 HRS @ 302°F		
Hardness Change, pts max	-40	-19
Volume Change, % max	+60	+35
Fluid Immersion ASTM D471 Water 70 HRS. @ 212°F		
Hardness Change, pts. max.	+/-5	0
Volume Change, % max.	+/-5	0
Tear Resistance, ASTM D624, Die B		
kN/M, min	9	14
Low Temperature BrittlenessTest ASTM D2137, Method A		
3 min. @ -55°C	Pass	Pass

Parker O-Ring Division
2360 Palumbo Drive
Lexington, Kentucky 40509
(859) 269-2351

2.12.6 Impact (Free-Drop) Test Report

THIS PAGE INTENTIONALLY LEFT BLANK

CSA Engineering, Inc.
Engineering Services and Products in Structural Dynamics www.csaengineering.com
2565 Leghorn Street Mountain View, California 94043-1613 (650) 210-9000 Fax: (650) 210-9001

Test Report:
Drop Tests of the
Alpha Omega Services Shipping Cask
for Radioactive Material

Report No. 2007533 Rev 1
May 25, 2007

TABLE OF CONTENTS

This report documents the drop tests of a transport package for shipping radioactive material. The planning and the test itself were conducted by CSA Engineering in cooperation with the Nuclear Energy Division of General Electric and with Alpha Omega Services. CSA's work is conducted under Purchase Order number AOS-3301 from Alpha Omega Services who will be the end user of the transport package.

David A. Kienholz
Vice President/Principal Engineer

Christian A. Smith
Quality Assurance Manager

Revision History

Rev 0 19 April 2007

Initial release.

Rev 1 19 May 2007

Sequence photos for end drop, Figure 29, changed from color to black and white.

Redundancy in data types noted in introduction.

Total deceleration times estimated from video data and results included.

Conclusion added re. total deceleration time from video data.

1. Introduction and Background

This report documents the objectives, methods, results, and conclusions of drop tests of a shipping package for radioactive materials. Among other requirements imposed by the Nuclear Regulatory Commission (10 CFR 71), a shipping cask with its protective impact limiter must survive a 30-foot free fall onto an unyielding surface without loss of structural integrity by the cask. Damage to the impact limiter is allowed but the cask itself must remain capable of performing its primary functions of providing containment, shielding, and subcriticality[1] of the radioactive material.

The cask was the model AOS-165, the largest of a family of casks developed by General Electric Nuclear Energy for Alpha Omega Services. Therefore questions of testing scale models are not considered in this report.

As usual in testing of shipping packages, the test was done without radioactive material. This means that compliance with requirements must be demonstrated indirectly. In this case compliance was shown through dimensional inspections and leak rate tests of the cask before and after each drop.

In addition to verifying that the cask and impact limiter comply with their primary requirements, various instrumentation was used to obtain quantitative data during the test. This data is used both for engineering design and for verifying that the test itself meets its requirements. Measurement methods were chosen to produce some redundancy; data obtained by different methods can serve to verify each other or to fill in for each other in the event of lost data.

2. Test Overview and Objectives

The test objective is to obtain data for demonstrating the adequacy of analytical methods employed for qualifying the shipping package, both at the size tested and scaled-down versions. These analytical methods are used to show that the impact limiters are capable of limiting impact loads on the payload to an acceptable level.

The package was free-dropped three times, once in each of three orientations. The orientations, shown in Figure 1, and the reasons for choosing them are as follows.

[1] Subcriticality is always a requirement for a nuclear shipping container but is not relevant to the present test.

- End drop. The package was dropped with its axis vertical such that it struck on one end. This orientation usually tends to present the largest crushing surface and thus the largest crushing force and greatest payload acceleration.

- Side drop. The package was dropped with its axis horizontal such that the impact limiter sections on both ends struck the ground at nominally the same time. This tends to produce the largest bending and buckling loads in the cask walls.

- Slap-down drop. The package was dropped with its axis at an angle to the vertical as shown such that it lands on one side of one impact limiter section. This tends to present the smallest crush area and thus the largest inward deformation of the impact limiter. It also produces a "slap-down" effect where the cask acquires a significant angular velocity after initial impact, leading to high loads when the second impact limiter strikes the surface (slaps down).

The tests were performed in the order shown above with new impact limiters for each test. Previous tests have used the first two orientations successfully[2]. The slap-down orientation is new and is included in place of previous c.g.-over-corner drops on the basis of analysis which indicates that slap-down is a worst-case.

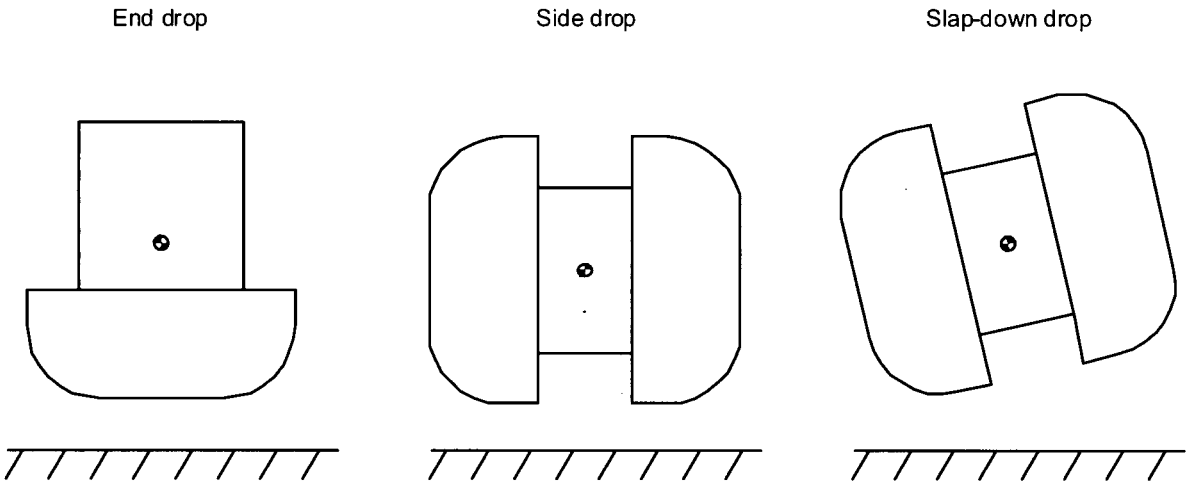

Figure 1 Package orientations for the three drop tests.

Structural integrity of the cask was determined after each of the three drops. Methods for doing so are described in the next section on acceptance criteria. In addition to this pass-fail functional testing, engineering data in the form of cask and impact limiter acceleration time histories at several location/directions were sensed and recorded. Pressure sensitive film was used to

[2] Kienholz, D.A., and Allen, Bradley, "30-ft. Free Drop Tests of a Quarter-Scale Model 2000 Transport Package," GE Nuclear Energy division Report NEDO-31581, San Jose, CA, August, 1987.

determine the pressure distribution between the cask and impact limiter. Details of the methods for obtaining these engineering data are presented later in this report.

3. Acceptance Criteria

The primary pass-fail criterion for the test is based on a helium leak rate test performed on the cask before and after the drop tests. The methodology for the leak test is detailed later in subsection 5.9 An acceptable leak rate is less than 2.96 x 10E-7 standard cubic centimeters of helium per second at a differential pressure of one atmosphere[3]. For the package to be judged acceptable, the measured leak rate must be less than this amount both before and after the drop tests.

The secondary criterion relates to external dimensions of the cask. These shall not have changed by any amount that would prevent or endanger the cask's performance of its primary functions of containment and shielding.

4. Cask Description

The test article is a full-scale prototype transport package. It is composed of two main parts: the cask and the impact limiters. The cask (
Figure **2**) is cylindrical in shape with an outside diameter (excluding trunnion lugs) of 46.20 inches and an axial length of 59.40 inches. Weight of the cask with impact limiters is approximately 38,500 lbs. The cask is composed of stainless steel inner and outer shells with thick tungsten inserts between them for radiation shielding. The central payload cavity is cylindrical in shape with a diameter of 10.72 inches and axial length of 33.63 inches. The cavity is connected to atmosphere by two small ports (shown later in cross section) that are both sealed during normal transport operations.

The cask lid is secured to the cask body by 20 socket head cap screws, size 1-8 x 3.25. There is a double seal between the lid and body with a sealable port running from the volume between the seals to atmosphere. The second (outer) seal and the port allow testing the integrity of the inner seal as described in a later subsection.

The impact limiter is in the form of two "caps" that go over the ends of the cask (
Figure **2**). Each cap is composed of a stainless steel shell filled with castable impact-absorbing foam. The caps are installed over the ends of the cask and secured to each other by six turnbuckles as shown.. Each cap has a recess in its outer end to produce the desired crush area and thus the desired crushing force during an end drop. The lifting rings shown at the top of

[3] Mok,G.C., Carlson,R.W., Lu, S.C., and Fischer, L.E.,"Guidelines for Conducting Impact Tests on Shipping Packages for Radioactive Material,", Lawrence Livermore National Laboratory Report No. UCRL-ID-121673, September 1995, page 19. Also ANSI N14.5.

each impact limiter are for lifting the impact limiter by itself. When assembled, the package is lifted by the side trunnions on the cask.

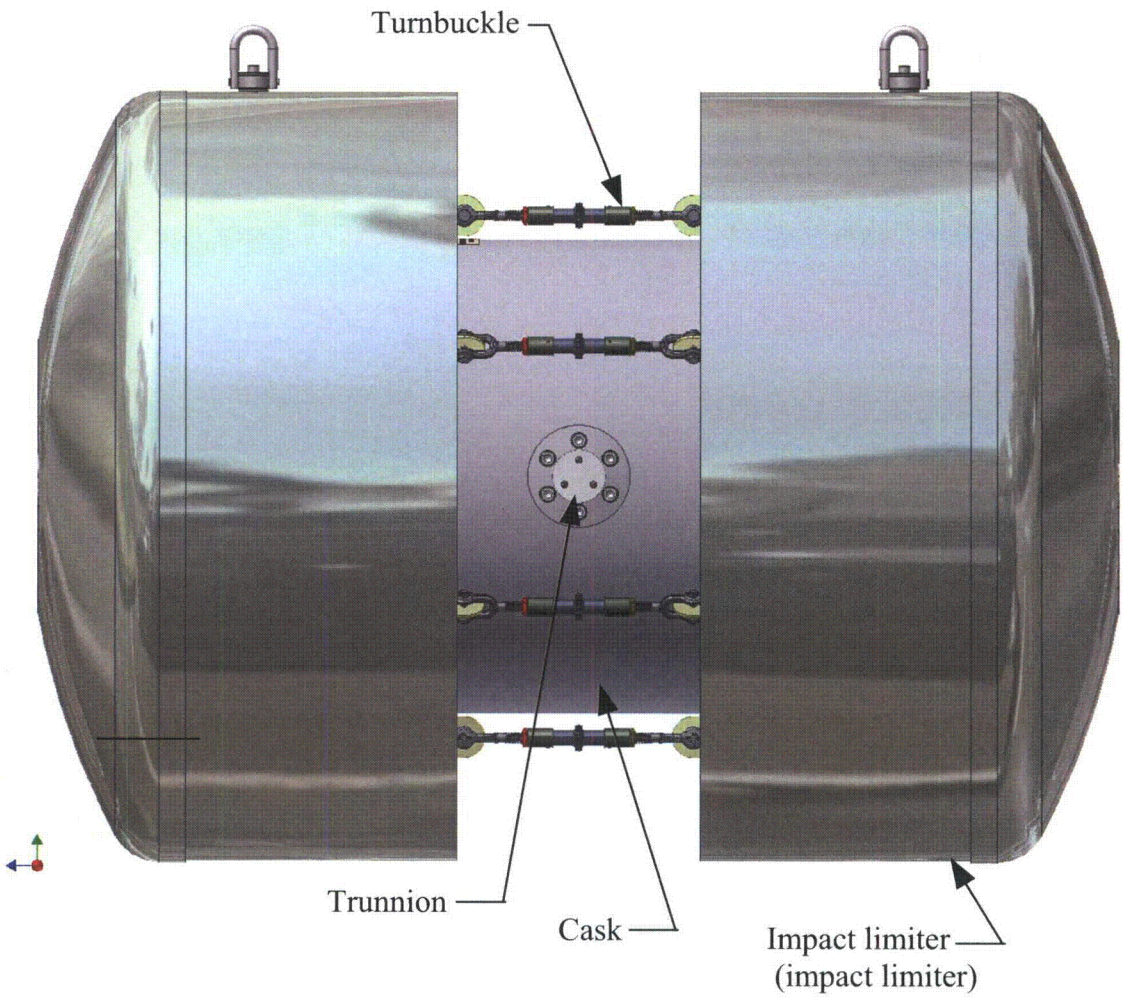

Figure 2 Shipping cask with impact limiters

5. Test Procedure and Equipment

The test procedure and instrumentation generally followed that used successfully in a 1987 test of a quarter-scale transport package[4]. Some enhancements were made in accordance with NRC

[4] Kienholz, D.A. and Allen, Bradley op cit

guidelines published since the 1987 test[5] and to take advantage of advances in photographic and instrumentation technology.

5.1 Drop target

The drop target was a large reinforced concrete block embedded in the earth at the General Electric Vallecitos CA site. Figure 3 shows a plan view of the site, including the crane for lifting the test article and the locations for two high-speed cameras. The concrete block is approximately 20' x 15'6" in plan view and six feet thick. It has a steel plate, 120" x 90" x 3", embedded in its horizontal top surface. The target block weighs approximately 290,000 lbs. The concrete has a 28-day cured strength of at least 4500 psi. The site has been used several times before for drop tests. The storage shed on the north side of the drop pad was moved to allow room for the tests. Figure 4 shows an overall view of the site.

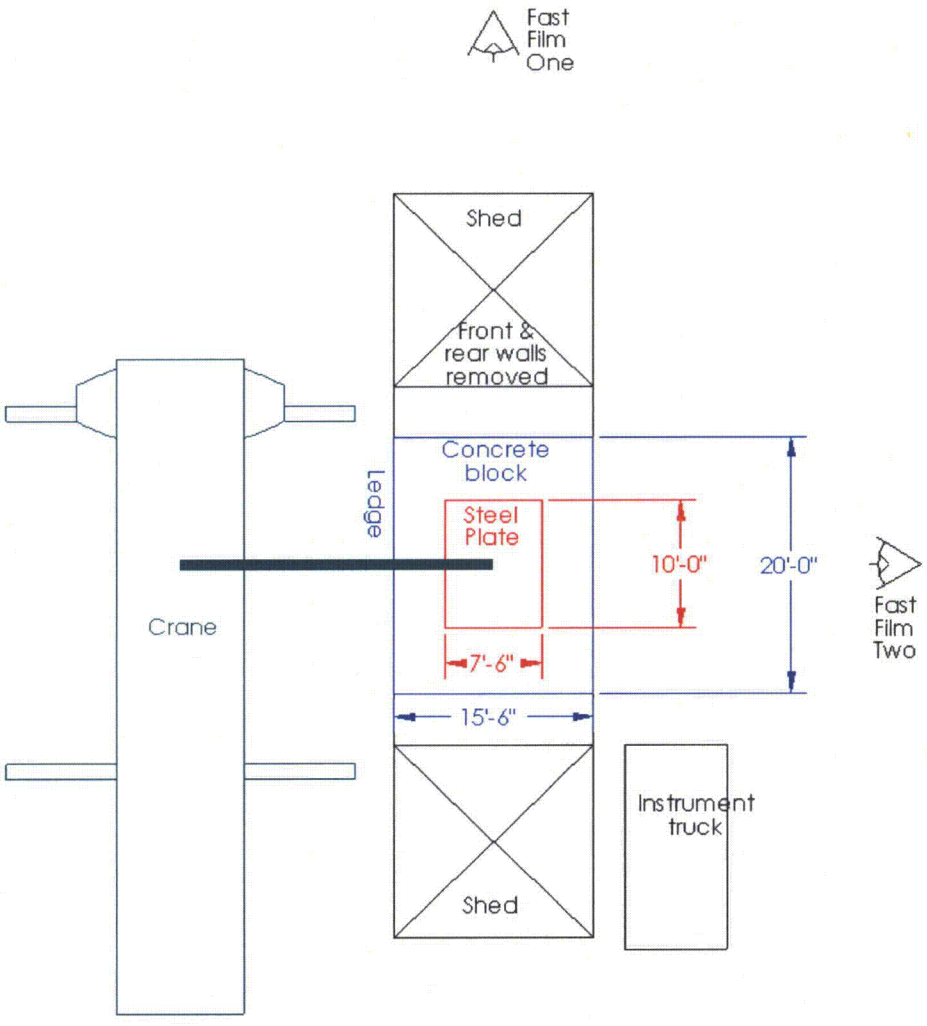

Figure 3 Plan view of drop test site.

[5] Mok, G.C. et al, op cit

Figure 4 Drop test site with crane and instrument truck in place.

5.2 Pretest and post-test dimensional inspection of cask

Dimensional inspections of the cask before and after each drop were done by East Coast Metrology, Topsfield, MA, under subcontract to GENE. The measurements were made using a laser tracker system capable of rapidly locating many points on the cask in 3-dimensional space. Figure 5 shows an impact limiter being set up for measurements. The laser tracker is the blue device on a tripod on the left

For the impact limiters, scan data was taken at the 0, 30, 60, 90, 120, 150, 180, 210, 240, 270, 300 and 330 degree profiles. In order to compare each impact limiter in its pre- and post- drop condition, an alignment using the bottom perimeter (opposite the domed-end), measured as a circle, was used a reference. By measuring it as a circle, the center point and vector of the measured circle were established. The portions of this circle that were deformed due to each drop test were not used in this calculation. The vector of this axis was defined to be the primary datum in this alignment. A point was then measured at the 90 degree lifting lug to establish the second axis in the coordinate system. This process provided the only repeatable means to align each impact limiter and subsequently compare the results.

Figure 5 Measuring an impact limiter with the laser tracker.

Once the pre- and post-drop scan data was obtained for each impact limiter, the 90-270 degree profile cross-sections were overlaid in order to calculate the magnitude of deformation for each drop.

For the cask, the 0, 90, 180, and 270 degree profiles were scanned. An alignment using the axis of the cylindrical part of the cask as the controlling datum was used. This axis was then intersected with the "Lid End" of the cask and a point was constructed. Another point was measured at the 90 degree lifting lug to establish the other axis. This alignment was repeated for each measurement of the cask. Results from scans taken before any of the drop tests are shown in Figure 6 and Figure 7. The red areas represent the positive (maximum deviations) and the yellow areas represent the negative (minimum deviations) from the nominal as-designed profile.

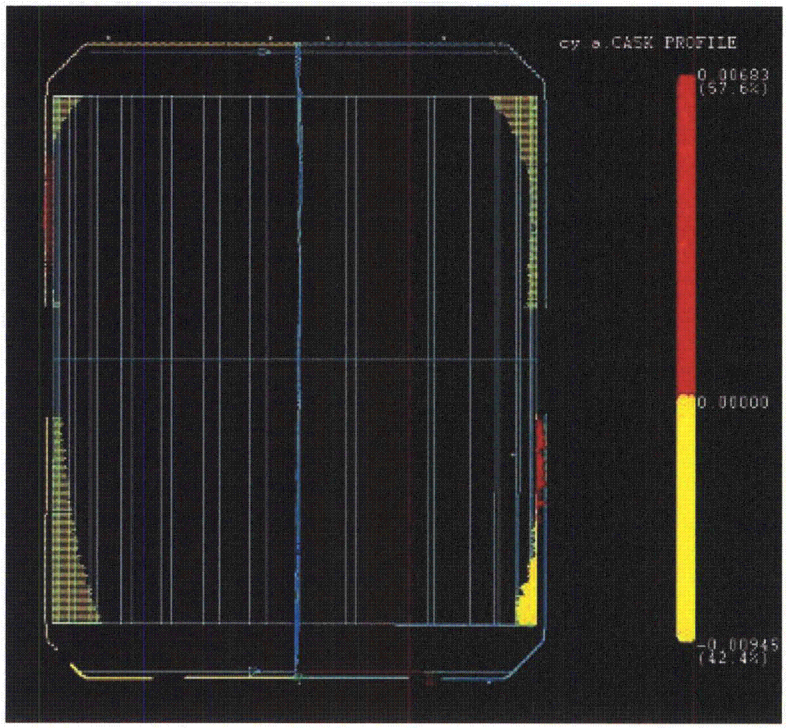

Figure 6 Scan data from cask taken before the first drop, 0-180-degree cross section

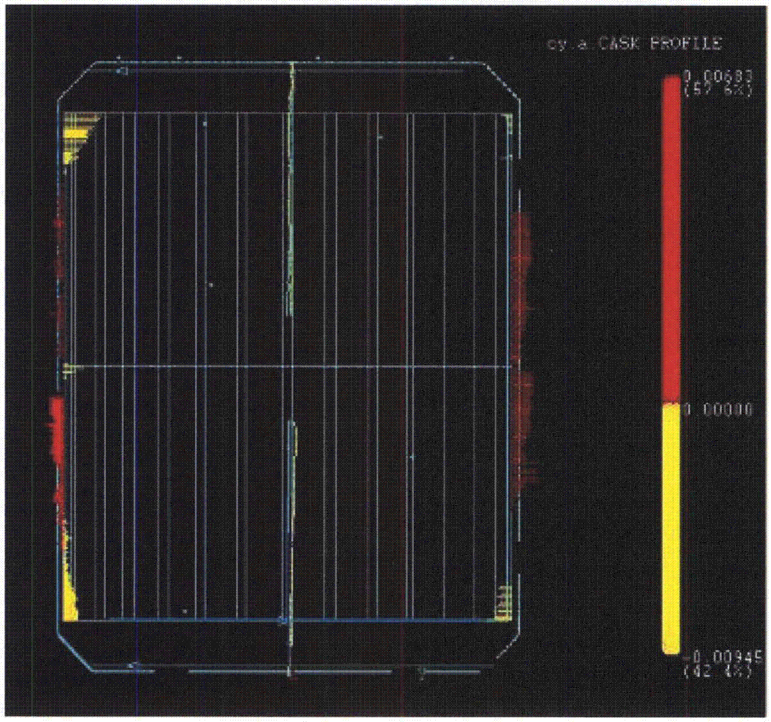

Figure 7 Scan data from cask taken before the first drop, 90-270-degree cross section.

5.3 Lifting and release methods

For each drop, the test article was lifted by a 90-ton mobile crane to a height of at least 30 feet[6] directly above the steel plate drop target. The crane was provided by Peninsula Crane Service under subcontract to GENE. GENE provided the remaining rigging equipment. Figure 8 illustrates the crane setup for the end drop. Figure 9 shows the crane and quick-release mechanism being tested by dropping a dummy weight.

Two methods were used to measure the drop height. For the first (end) drop, a graduated light chain was hung from above the package.. The chain was marked at one-foot and ten-foot intervals such that the package height above the impact point could be verified just before the drop. The chain was then pulled out of the way prior to the drop. For the second and third drop, a tape measure was secured with tape to the bottom of the package and used to adjust the height to the desired value. The tape measure was then pulled off the test article from the ground.

The use of a hydraulic crane required that the crane boom be "snubbed" with heavy wire ropes from the crane hook down to heavy weights on the ground (Figure 8). The snubbing lines restrained the crane boom when the load was released, preventing damage to the hydraulic system. Since the snubber lines were of fixed length and had to be taut at the time of release, they had some effect on the drop height. Shorter rigging as used on the end drop caused the drop height to be greater than for the side and slap-down drops. However the drop height was over 30 feet for each drop. Exact values are given later.

The package was released using the mechanism shown in the Figure 10, Figure 11, and Figure 12. The heart of the system is the mechanical release mechanism shown in Figure 10. Called a SeaCatch Model TR15Air[7], it is used in the marine industry for releasing loads while under tension, often underwater. In the photo on the right of Figure 10, the release mechanism is actuated by hand via the lever on the right side. Lifting the lever opens the jaws and allows the lower anchor shackle to fall free. The red rope tied between the shackles in the figures is only for demonstration. In the actual test, the package was hung from the lower shackle, the red rope was not present, and the lower shackle remained attached to the test article as it fell.

Because the package must strike the drop target in a known, repeatable orientation, it is essential that the release mechanism do its job quickly and cleanly, minimizing transient forces and moments imposed on the package during release. This minimizes the angular velocity imparted to the package at release and allows it to fall without rotation such that it strikes the drop target in the same orientation it had prior to release. To this end, the SeaCatch release mechanism was equipped with an integral air cylinder, an accumulator, and a fast solenoid valve for actuation. This method was used in preference to pulling the release lever via a lanyard because the required pull force of over 100 lbs would have disturbed the orientation of the test article just at the critical moment of release.

[6] 30 feet minimum from the lowest point on the test article to the upper surface of the steel plate of the drop target.
[7] McMillan Design, Inc., Gig Harbor, WA.

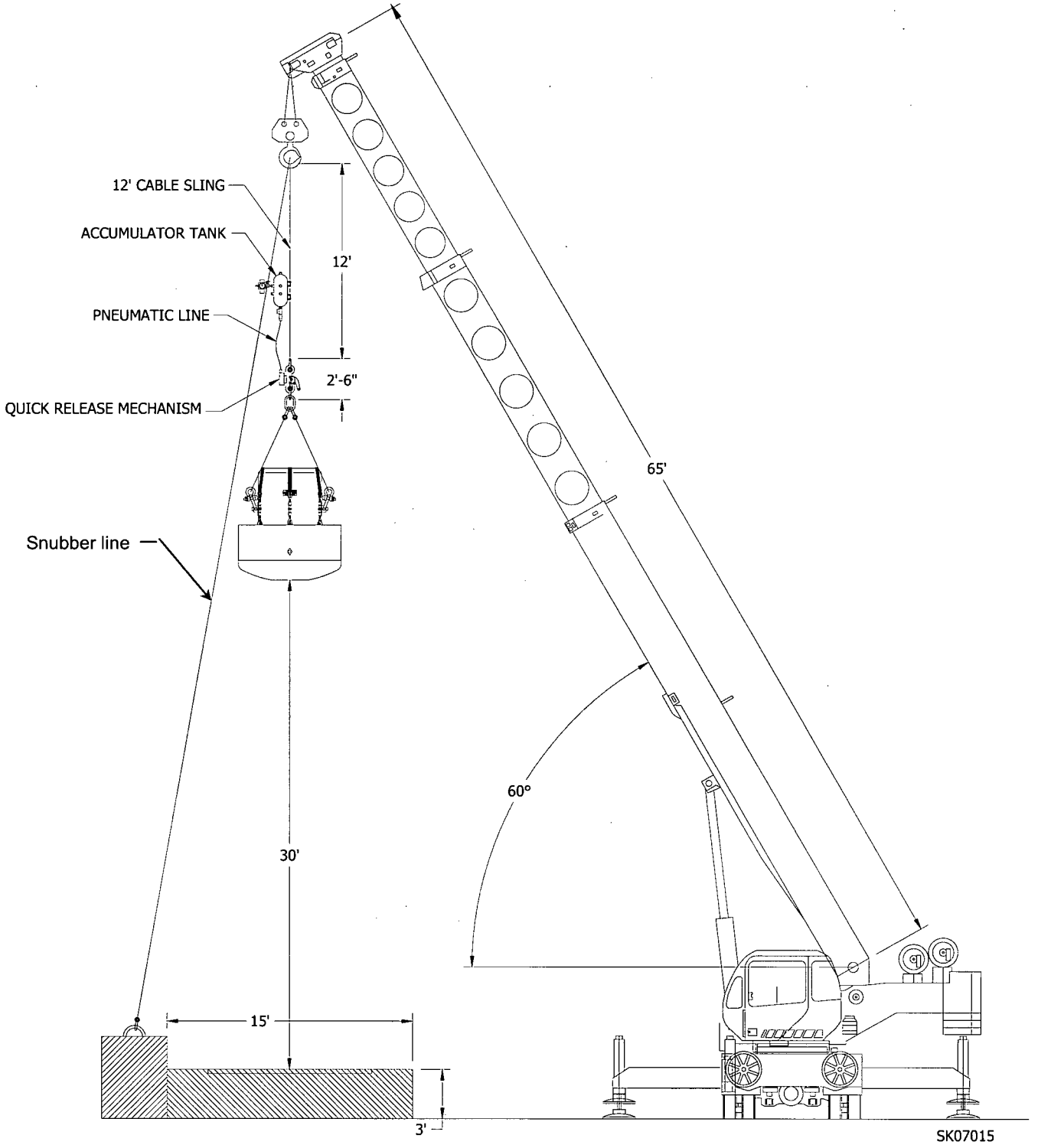

Figure 8 Crane and rigging set up for end drop.

Figure 9 Testing the quick-release mechanism by dropping a dummy weight.

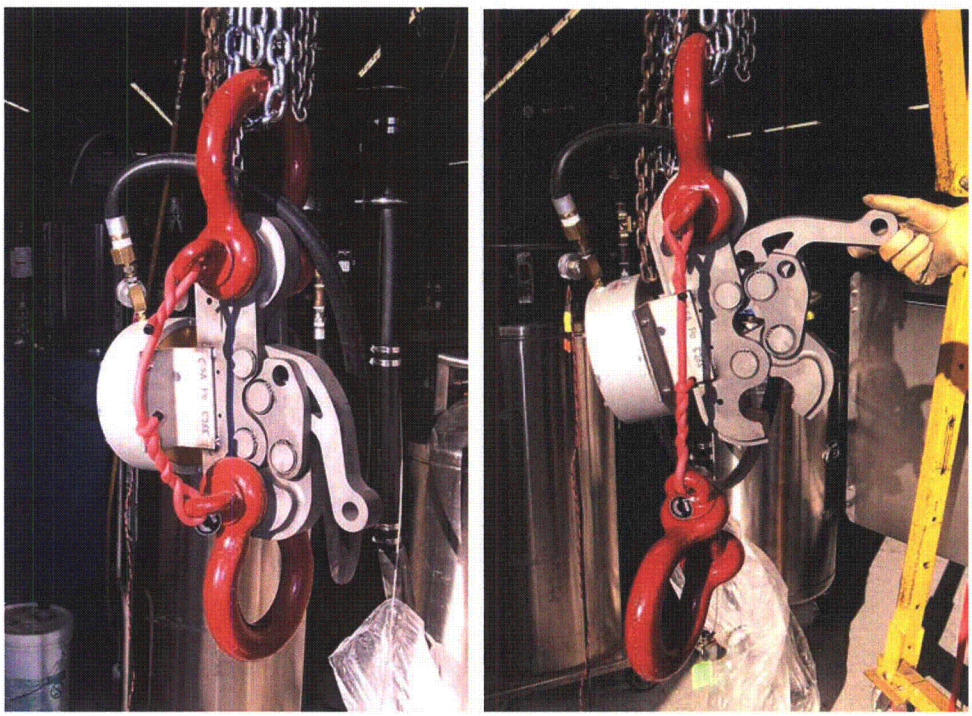

Figure 10 SeaCatch release mechanism before release (left) and after release (right).

A quick release was obtained by using a 3-gallon local air accumulator tank and a fast-acting, two-stage, electrically triggered diaphragm valve mounted close to the release mechanism . Calculated release time is on the order of 0.2 seconds. Figure 11 shows the accumulator tank and valve. Figure 12 shows the accumulator and valve mounted on a short section of heavy wire rope with the SeaCatch hanging from the loop at the lower end of the wire rope. In operation, a compressed air line for charging the accumulator and electrical trigger line were run up the crane boom and over to the accumulator tank.

The SeaCatch is a model TR15AIR and is rated at 50,200 lbs working load with a safety factor of five. It was proof tested to twice the working load by the manufacturer prior to delivery to CSA. Likewise the wire rope, which is rated for 42,000 lbs, was proof tested to 84,000 lbs.

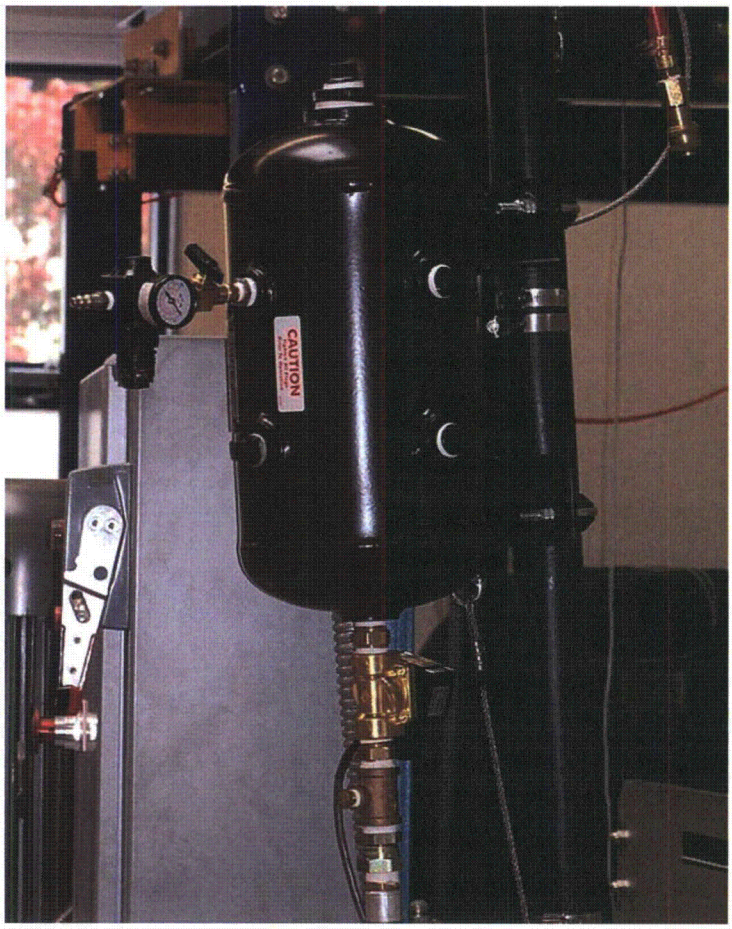

Figure 11 Accumulator tank and fast-acting valve for operating the SeaCatch air piston (left). Entire release system (right).

Figure 12 Cask being assembled with impact limiter for the end drop. The quick-release mechanism is visible at the top of the picture. Pressure-sensing paper has been taped to the part of the cask that goes inside the impact limiter.

5.4 Acceleration sensing

Acceleration time history data was recorded using accelerometers inside the cask and on the impact limiter. A total of nine uniaxial sensors was used, configured as three triaxial groups. One triaxial group was mounted on the flat surface of the impact limiter (Figure 13). The mounting block is fastened to the impact limiter by two ¼-20 cap screws threaded into tapped mounting bosses welded to the impact limiter. A cable breakout bracket for mating the main umbilical cable to individual accelerometer cables is likewise mounted to tapped bosses on the impact limiter as shown.

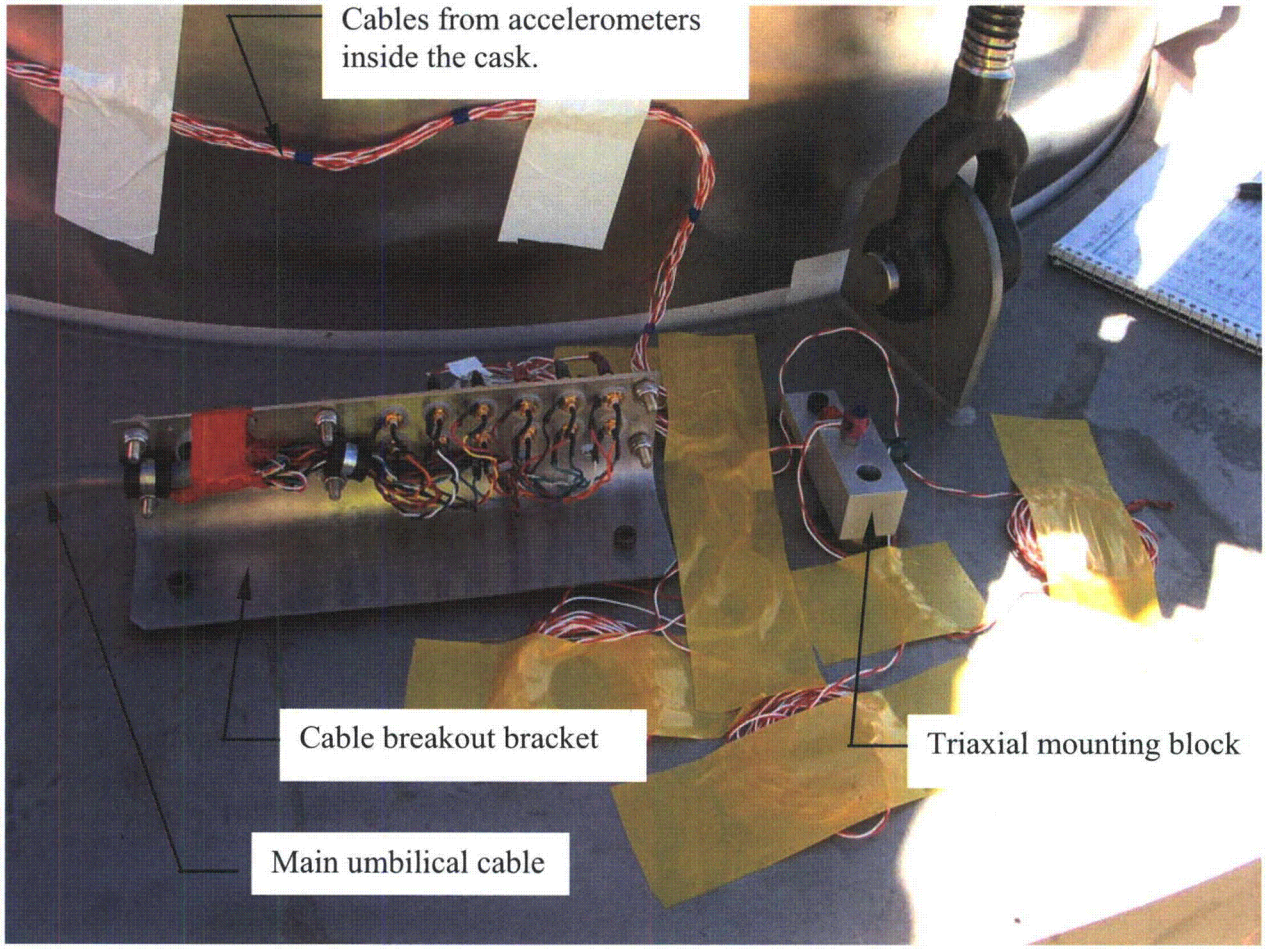

Figure 13 Triaxial accelerometer group mounted on impact limiter. The sheet metal part is a bracket for connecting the 20-conductor umbilical cable to the two-conductor cables of the individual accelerometers.

Two triaxial groups were mounted inside the cask on the wall of the payload cavity (Figure 14). They were mounted on machined aluminum blocks bonded to the cavity wall with Lord 906-16 acrylic structural adhesive. The triaxes were at nominally the same axial location and 180 degrees apart, at the 90-degree and 270-degree lines on the cask. Each triaxial set sensed in

nominally the cask radial, tangential, and axial directions. The cask was oriented for the side drop and slap-down drop such that a plane containing the cask axis and the accelerometer locations was vertical and the accelerometers on the 90-degree line were on the upward-facing side of the cask. In the photos, the radial accelerometers are marked with red tape, the axials with purple tape, and the tangentials with green tape.

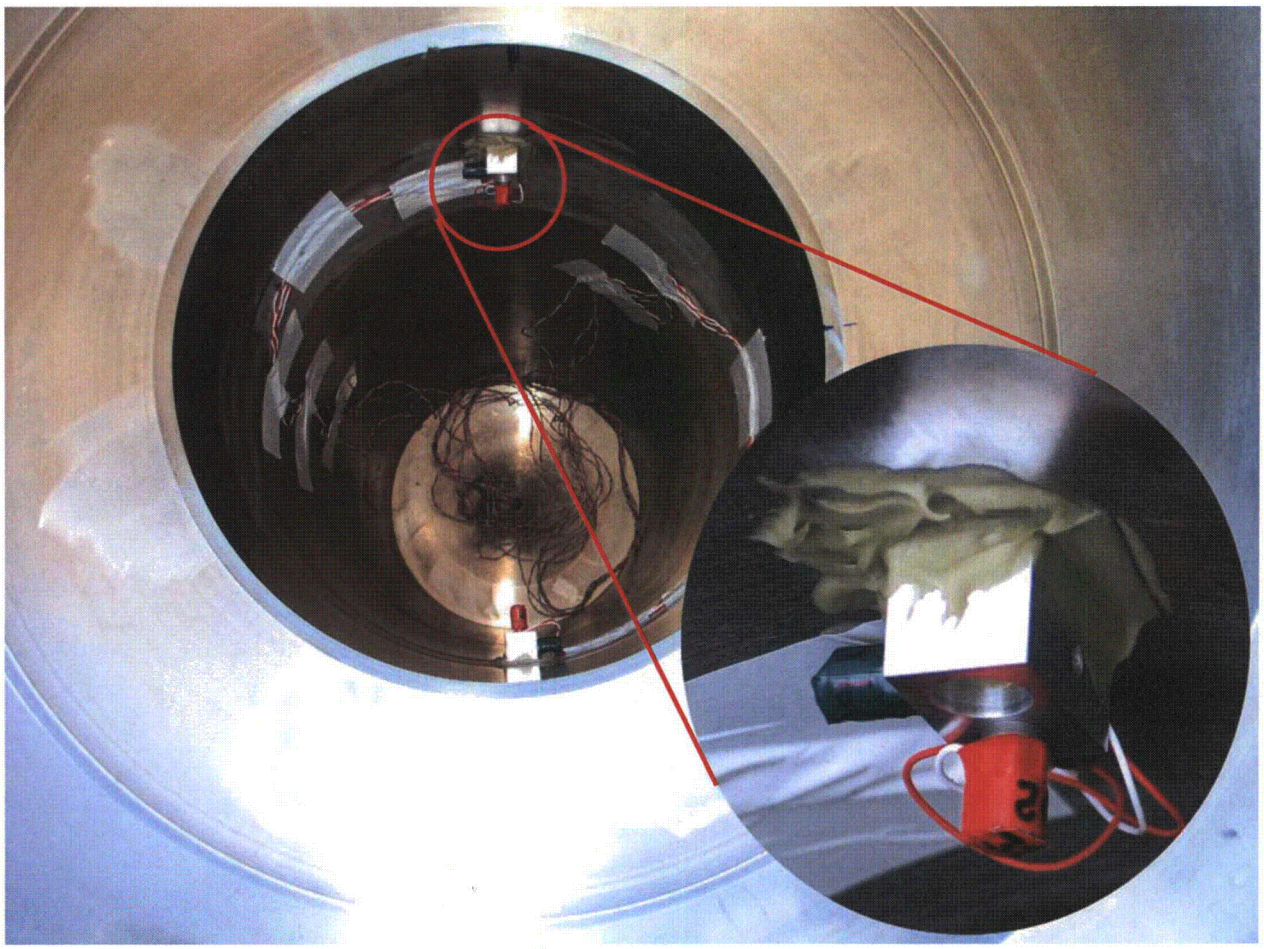

Figure 14 Accelerometers mounted inside the cask. The cables can be seen exiting via the drain port at the bottom of the cask payload cavity.

Cables for the accelerometers inside the cask were routed out through the drain port which exited near the cask bottom along the 90-degree azimuth. For the end drop, only a single impact limiter was used and it was on the lid end of the cask, with the cask being dropped upside-down (Figure 17). For this drop, there was no interference between the accelerometer cables and the impact limiter. For the other two drops, impact limiters were mounted on both ends of the cask and the cables had to come out through the 1/8th-inch radial gap between the cask OD and the impact limiter ID (Figure 16). 1/8-inch-diameter stainless steel rods were welded to the impact limiter ID running in the axial direction on either side of the cable routing to prevent the cables from being crushed between the cask and impact limiter. As described later, this was only partially successful although acceleration data was obtained for the important initial impact on each of the three drops.

All accelerometers were of the piezoelectric, integrated amplifier (ICP) type. The accelerometers mounted on the impact limiter were PCB model 350B23 having a nominal range of +/-10,000 g's (0.5 mV/g sensitivity, 0.5 g resolution, range/resolution = 20,000) and a 1-dB bandwidth of 0.4 to 10,000 Hz. The triaxial accelerometers inside the cask were PCB model 353B13 having a nominal range of +/-1000 g's (5 mV/g sensitivity, 0.05 g resolution, range/resolution = 20,000) and a 1-dB bandwidth of 0.7 to 20,000 Hz. All were powered and AC coupled to the recording system by a Kistler model 5124A power supply/coupler. Figure 15 shows the accelerometers and their power supply / signal coupler. There is no pass-fail criterion based on cask acceleration. However the data obtained will be of use in understanding the package behavior during impact and for estimating loads on the cask.

Figure 15 Accelerometers (1,000 g on lower left, 10,000 g on lower right) and power supply / signal coupler.

Piezoelectric accelerometers were used in preference to bridge-type, DC-coupled accelerometers because the former tend to be better suited to the high acceleration levels found in drop testing. Also, they use simpler electronics integrated directly into the sensor which is of great value in eliminating noise pickup in the signal cabling. Their only disadvantage is that they cannot capture the part of the signal at very low frequency, below about 1 Hz for the present case. This is considered acceptable because the very short-duration impact events have only a very small part of their signal energy in this missing band. Peak accelerations during such short impacts can be measured with AC-coupled accelerometers with negligible loss of accuracy.

The polarity for all accelerometers follows the industry convention: acceleration into the mounting surface of the sensor gives a positive output voltage. Thus the axial accelerometers inside the cask (Figure 14) give a positive voltage when the acceleration is towards the bottom end of the cask (as opposed to the top or lid end), as was the case for the end drop.

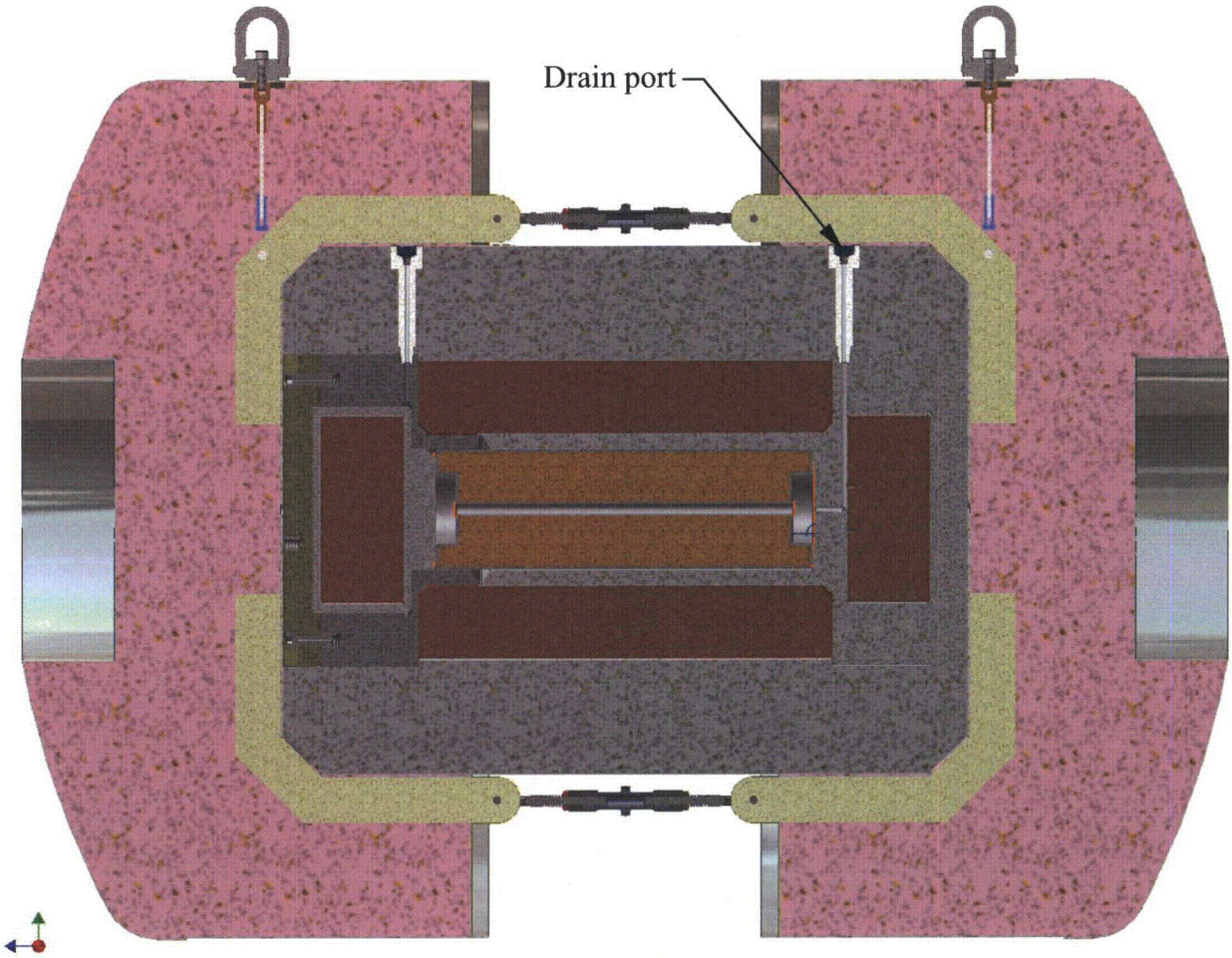

Figure 16 Cross section of cask showing drain port to be used for accelerometer cable routing.

Cables for the accelerometers inside the cask were routed through the water drain port (Figure 16) such that no special feedthroughs or modifications to the cask were needed. During the leak test, the cables were disconnected from the external breakout bracket and pushed back into the drain port so the port can be plugged.

A multi-channel umbilical cord with one shielded, twisted pair for each accelerometer was used to route the signals to a breakout box with BNC connectors on the output side. BNC cables then carried the signals to the Kistler power supply/coupler and from there to the data acquisition system located in the instrumentation truck. The total cable length of approximately 150 feet presented no significant limitation for the relatively low-frequency signals of interest in this test.

Figure 17 Cables from accelerometers inside the cask were routed through the drain port to the breakout bracket. Configuration shown is for the end drop with only one impact limiter used.

5.5 Acceleration signal recording

Acceleration signals during the impact were digitized and recorded directly to disk using a VXI data system from VXI Technology with a 16-channel front end card (model VT1432A). A/D conversion was done at 25,600 samples per second per channel with 16-bit resolution. Anti-aliasing filters were set for a cutoff frequency of 10 kHz.

Real time data acquisition was performed using I-DEAs TEST software to control the VXI front end. Immediately following each drop tests, acceleration time history data was translated to MatLab .mat format. MatLab was used for all display, plotting, filtering, spectrum analysis, and other post-processing work.

It was planned originally to use a digital tape recorder in parallel with the VXI system for redundancy. However problems were encountered with the tape recorder during test preparation so the VXI system was used alone. It performed satisfactorily so no backup was needed.

During the 1987 test, each acceleration signal was recorded to two channels of an FM instrumentation tape recorder. This allowed two different full-scale settings to be used for each signal in order to obtain the best possible signal/noise ratio within the limited (50 dB) dynamic range of the recorder. Modern 16-bit digital recording systems such as the VXI system have rendered this unnecessary since they typically have well over 72 dB of dynamic range.

5.6 Data processing

Data acquired with the VXI system was initially in I-DEAs .ati format. It was converted immediately on-site to MatLab standard double precision (8 bytes per sample) using the I-DEAs IMAT translator. Simple plotting and processing routines were created using basic MatLab commands and the MatLab Signal Processing Toolbox. All raw time history files were permanently archived.

Processing tasks include

- locating, isolating, and plotting the relevant time sections containing the impact
- digital low-pass filtering of acceleration time histories to accentuate the rigid-body component over the resonant flexible-body components
- computing the energy spectral density of the acceleration transient to determine how much is rigid-body response and how much is flexural.

5.7 Contact pressure sensing

Pressure sensitive film was installed between the cask and impact limiters prior to each drop. The film (Fuji Prescale P/N M S R270 M10 1) changes color in response to pressure. The single-sheet type contains embedded microcapsules of a chemical that reacts with another chemical impregnated into the film to produce a red color. Higher pressure breaks more capsules and produces a more intense color. The size and density of the microcapsules can be tailored to make the color change occur over various pressure ranges. The film used is for the pressure range from 10 to 50 MPa (1450 to 7250 psi). Pressure can be inferred by comparing the exposed film to a color chart (Figure 18). However for the present application, the intent is simply to use the pressure paper to indicate areas of contact between the cask and impact limiters.

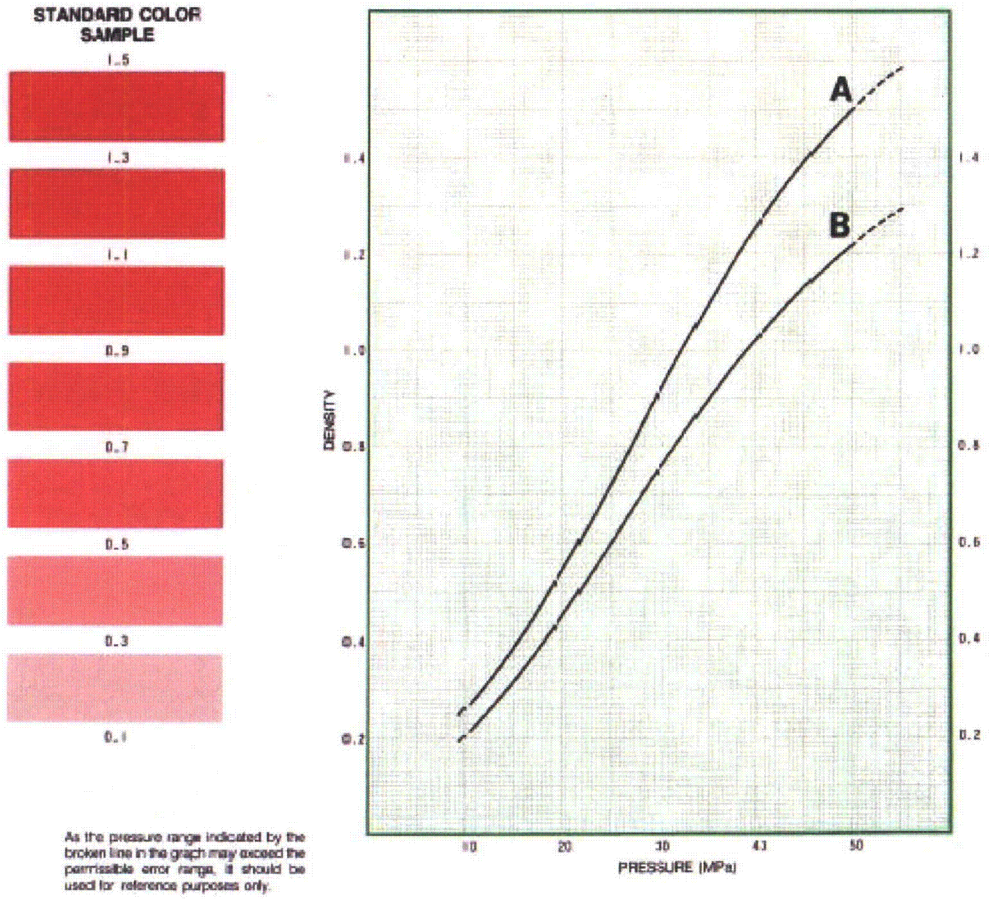

Figure 18 Chart for correlating color to pressure for Fuji medium-range Prescale film.

Fuji publishes two different color charts, one for film exposed to continuous pressure and another for film exposed to momentary pressure. However the two charts are virtually identical to the eye. Also, tests conducted with Prescale film prior to the 1987 drop tests[8] showed that the color change is virtually instantaneous upon exposure to pressure.

Figure 19 shows the cask with pressure-sensing paper attached being assembled into the impact limiter. The paper can also be seen in Figure 17 protruding out slightly beyond the impact limiter.

[8] Kienholz, D.A. and Allen, Bradley op cit

Figure 19 Cask with pressure paper attached being lowered into the impact limiter for the end drop.

5.8 High speed photography

High-speed digital video photography was used to record each of the three drops. All cameras were furnished and operated by Speedvision Technologies of San Diego under subcontract to CSA Engineering.. Two high-resolution black-and-white cameras were used with their sight lines at right angles to each other as shown in Figure 3 For the first (end) drop, lower resolution color cameras were located next to each black-and-white camera. Following review of the end drop videos from all four cameras, it was decided that only one color camera would be used for the second and third drops and it would be located at an oblique angle, about midway between the two black-and-white cameras. Figure 20 shows the cameras set up for the end drop.

Figure 20 High-speed cameras set up for end drop

Frame rates for the first drop were 1000 frames/second for the black-and-white cameras and 500 frames/second for color. After review of the videos, it was determined that the higher frame rate offered no real advantage so all cameras were operated at 500 frames/second for the second and third drops.

Following each drop, the raw files from the camera were converted to .avi format. The raw files remain available but examination of the compressed .avi files showed that they had adequate

resolution for most purposes. SpeedVision furnished software for extracting individual frames as jpeg or tiff files. This software was used to produce the frame-by-frame presentation given in later sections for each of the three drops.

A time scale and a length scale were included in the field of view of the each black-and-white camera. The length scales are dark-colored poles mounted vertically with light-colored graduations marked on them at one-inch (yellow marks) and one-foot (white marks) intervals. The poles are placed as close as possible to the vertical drop path and at the same distance from the camera as the drop path in order to minimize parallax and foreshortening error. Time scales, Figure 21, are rotating disks with a light-colored radial line. The background behind the disk has fixed, radial witness lines painted at 30-degree intervals as shown. The disk is rotated by a two-pole induction motor at a constant speed of approximately 3575 RPM or approximately 43 degrees per camera frame at 500 frames per second. The exact rotational speed was determined prior to the test using a digital optical tachometer. Table 1 shows the recent time scale calibration results and those from just before the 1987 test.

Table 1 Calibration results for time scales.

Clock	Speed (RPM)		Percent Change	Degrees per 0.002 seconds
	1987	2005		
#1	3579.00	3579.00	0.00	42.95
#2	3575.40	3572.30	-0.09	42.87

The use of time scales was a hold-over from earlier tests where high-speed film photography was used and frame rates could vary significantly from their nominal value. Modern digital video cameras have very accurate frame rate control (a few parts per million) so the time scales are not strictly necessary and are actually less accurate then the cameras themselves.

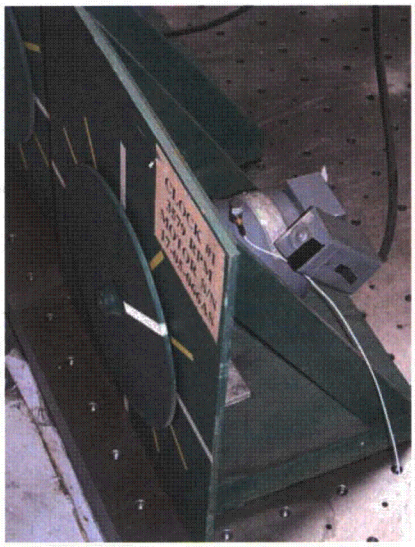

Figure 21 Time scale

At the suggestion of SpeedVision, a simple impact trigger signal generator was constructed and used to provide a time reference signal indicating when the test article first impacted the ground. The trigger was simply a sheet of cardboard approximately two feet square with a grid of 2-inch-square holes cut in it and sandwiched between two sheets of heavy-duty aluminum foil (Figure 22). The sandwich was taped to the impact surface at the location where the test article would first strike the surface. When the impact limiter hit the sandwich, it pressed the two sheets of aluminum foil together and closed a circuit. The resulting voltage signal placed a reference time marker on the stream of video frames to indicate first contact. It also cued the cameras to continue recording for another two seconds and then stop. Finally, it produced a step voltage signal that was recorded on one channel of the VXI data system as a time reference for interpreting the acceleration time histories. The impact trigger was used on the second and third drops and found to work very well.

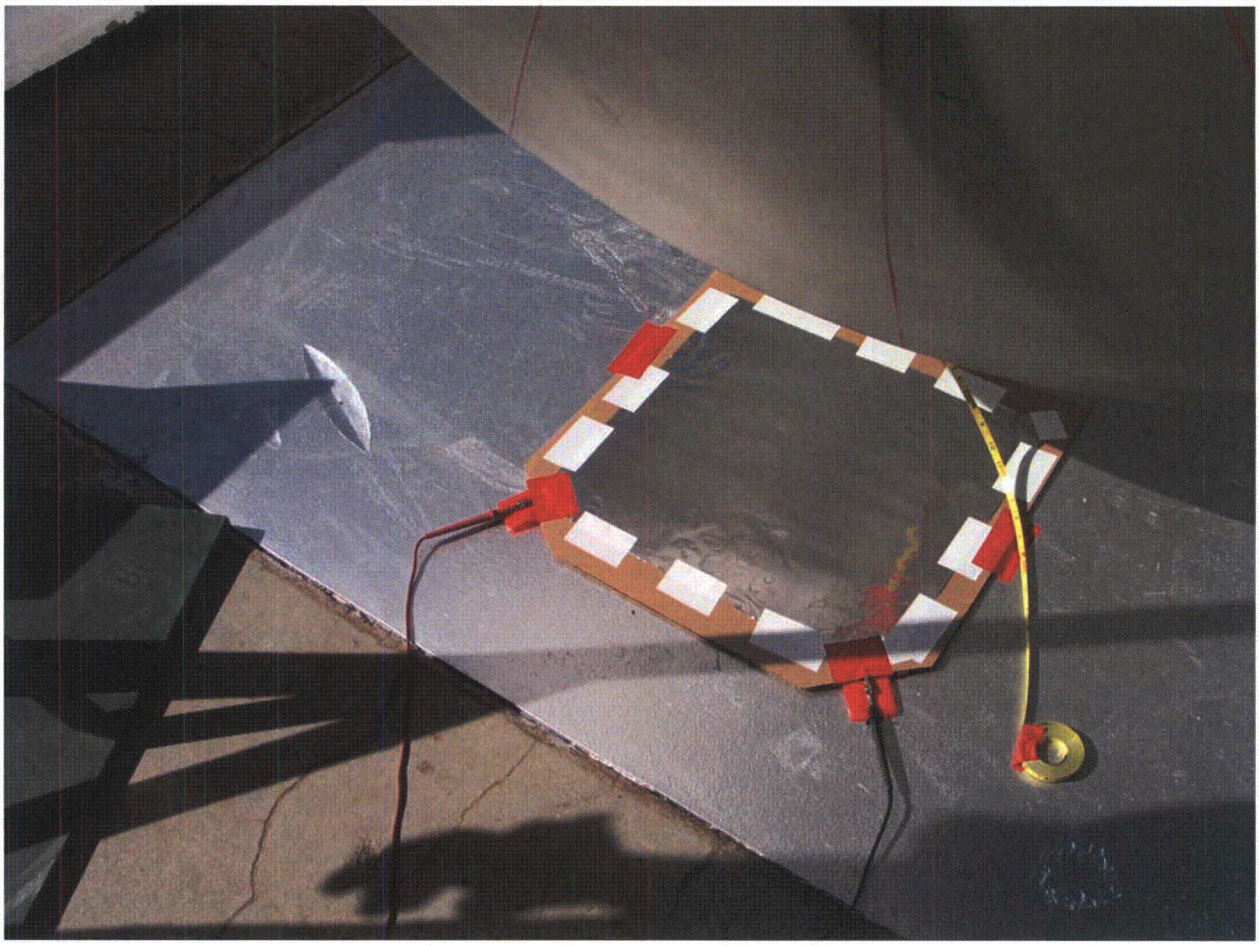

Figure 22 Impact trigger in position for side drop.

5.9 Leak rate tests

Integrity of the cask body and its lid seal was tested before and after each drop test by measuring the leak rate. The lid was bolted in place in the normal operating configuration. A helium pressure bottle was connected to one of the ports leading to the payload cavity and the cavity was purged with helium and then maintained at a pressure of 17.0 psia. The vacuum pump of a helium leak detector was connected to the port leading to the volume between the double seals of the lid. The volume between the seals was pumped down to an absolute pressure of less than 1 Torr and the leak rate of helium was measured by the leak. A leak rate of less than 2.96 x 10E-7 standard cubic centimeters of helium per second at this pressure differential was considered leak-tight. Leak detection equipment was furnished and operated by GENE personnel.

During the leak test, the cables from the accelerometers inside the cavity were disconnected from the break-out panel on the outside of the cask and pushed back into the port from which they exited the cask. The port was then plugged such that the cavity could be pressurized. Figure 23 shows the cask undergoing its initial leak test.

Figure 23 Leak testing the cask.

5.10 Test operations

GENE prepared a detailed check list of all the activities to be performed during preparation and execution of the tests. It was maintained by the GENE QA manager assigned to the project and included the designation of the individual responsible for each item. Items were checked off as they were performed.

5.11 Drop heights

Table 2 gives the free-fall distances for each of the drops. These are the measured vertical distances from the drop target to the lowest point on the impact limiter. They were different for the three drops for reasons given earlier related to the crane and rigging.

Table 2 Drop heights

Drop configuration	Drop height (feet and inches)
End	34'-3"
Side	31'-0"
Slap-down	31'-2"

6. Results: End Drop

6.1 Acceleration measurements

This section gives the time history plots of accelerations measured inside the cask and on the impact limiter for the end drop. Only the most important data are shown in this section. A full set of plots has been furnished to GENE. This organization will also be followed for presenting acceleration data from the side drop and the slap-down drop.

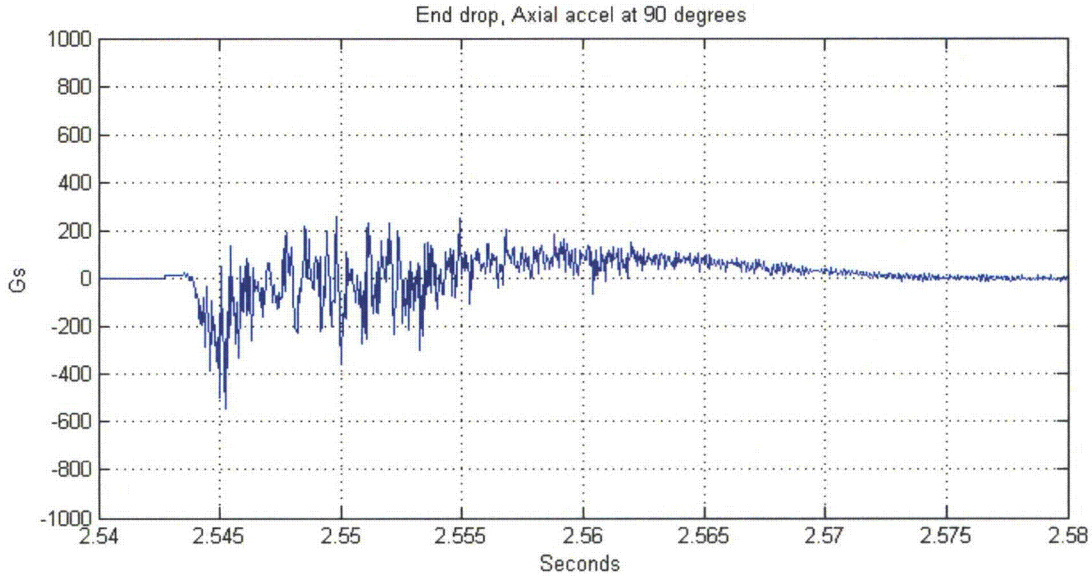

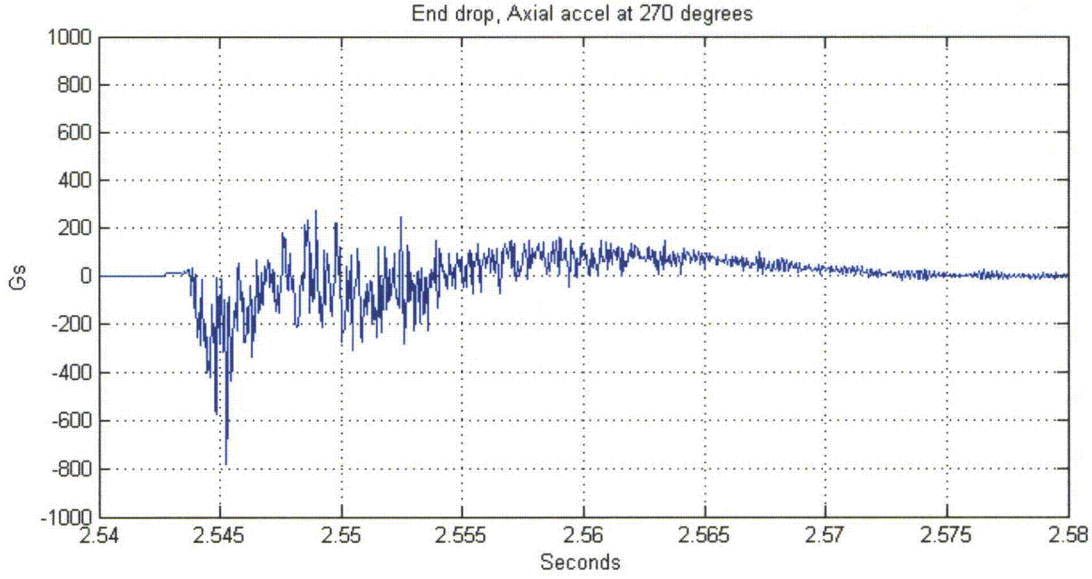

Figure 24 Accelerations measured at impact inside the cask for the end drop.

Figure 24 shows the signals from the two axial accelerometers inside the cask (Figure 14). These two were sensing in the vertical direction for this drop. A positive signal denotes upward acceleration at the accelerometer location.

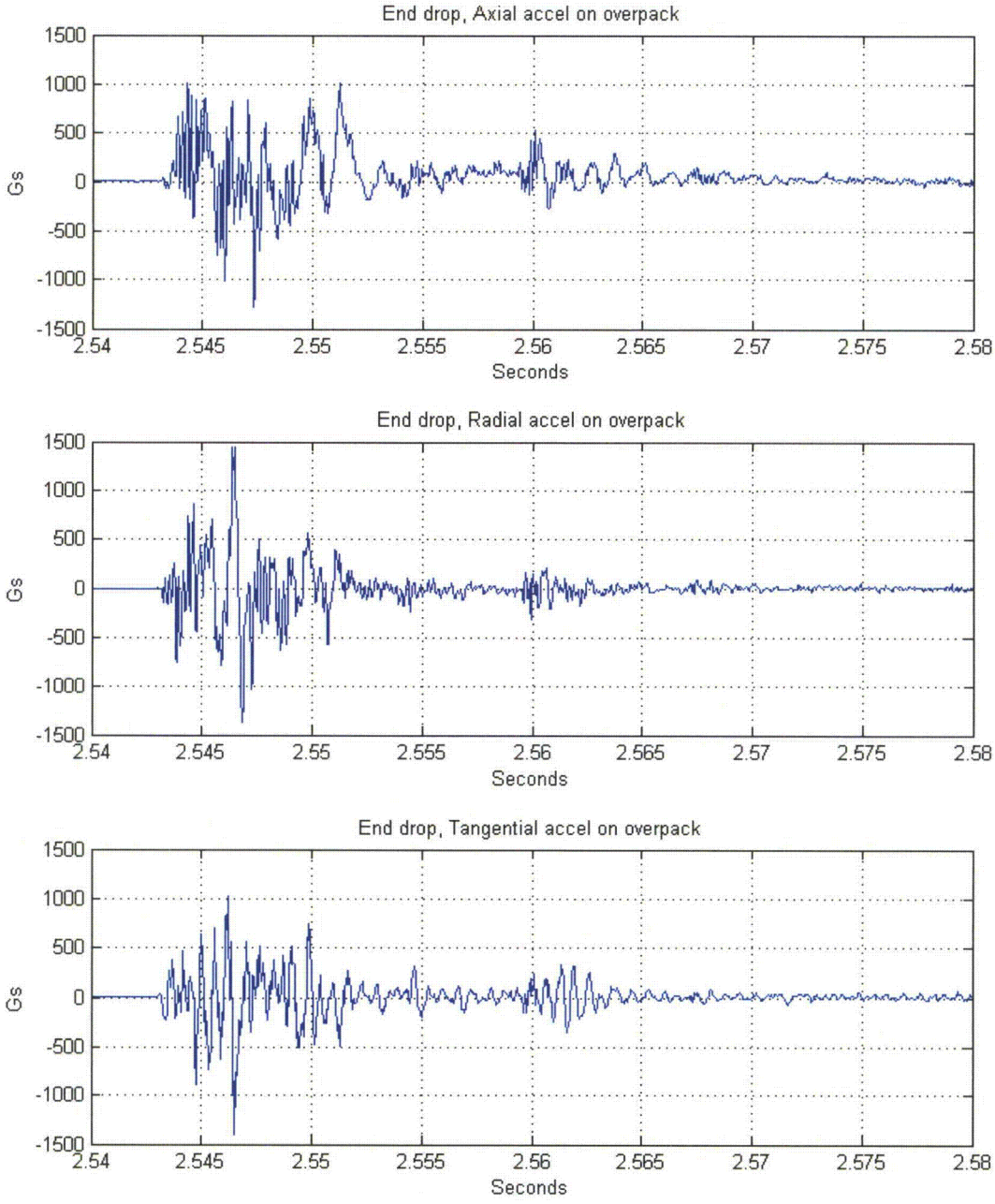

Figure 25 Accelerations measured on the impact limiter during the end drop.

Figure 25 shows data from the accelerometers on the impact limiter (Figure 13). Signals from all accelerometers showed a large amount of "ringing" or resonant response from the cask and impact limiter. This was not surprising considering the sharp blow applied to the package when it struck the steel plate of the target block. However the ringing makes it difficult to estimate the

true deceleration of the cask mass center. To this end, the signals were digitally low-pass filtered to reduce the resonant response and make the rigid-body component of the cask deceleration more evident. The filter was a 4-pole phaseless Butterworth[9] with a cutoff frequency of 900 Hz. Results are shown in Figure 26, Figure 27, and Figure 28.

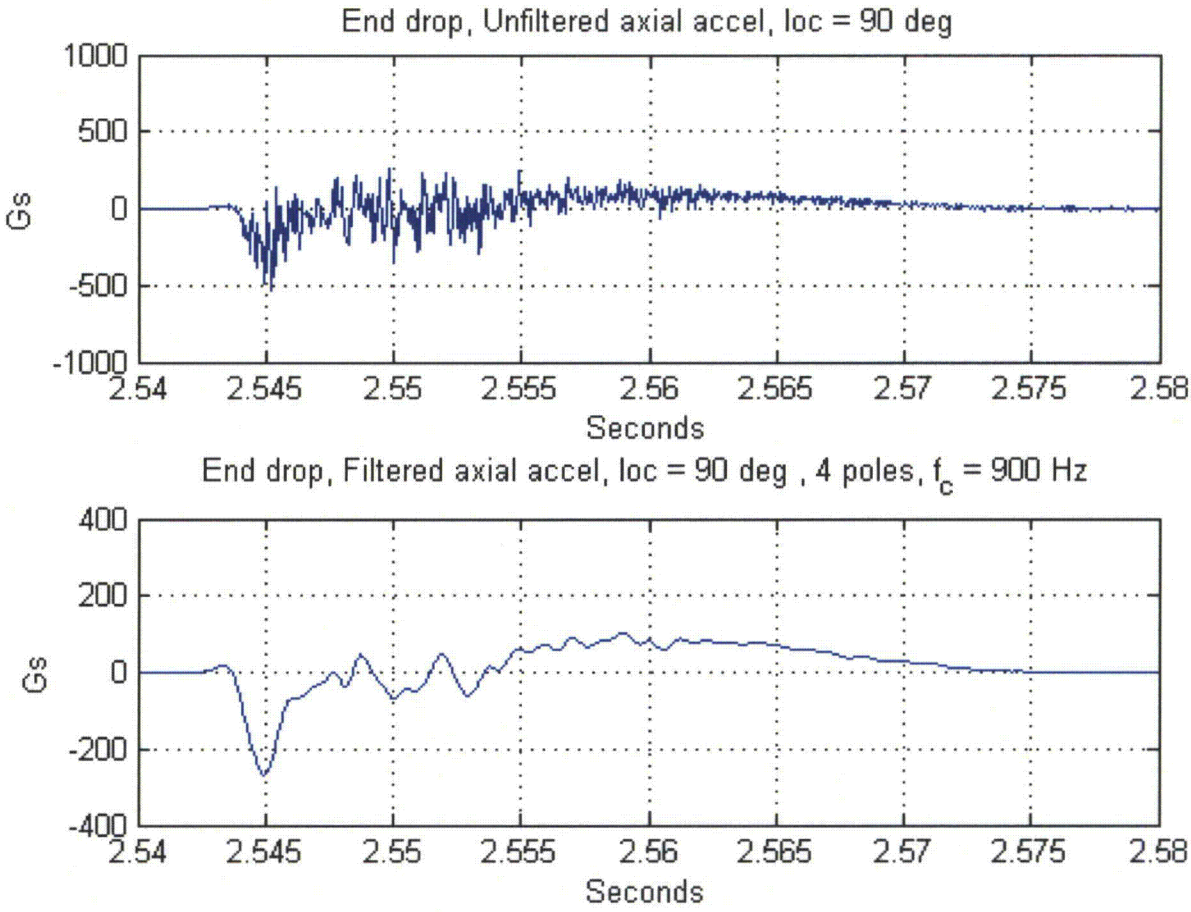

Figure 26 Signal from the axial accelerometer inside the cask on the 90-degree aximuth before (top) and after (bottom) low-pass filtering.

The vertical acceleration signals in Figure 26 and Figure 27 may seem confusing at first. It appears that the big spike in acceleration is in the downward direction. However the signals make sense when one considers the way the cask is constructed. Referring to Figure 16, the brown areas represent voids between the thick stainless steel walls of the cask. These voids are filled with heavy, tungsten "bricks" which are held in place only by steel wool packing. When the cask first strikes the hard surface, there is in fact a small pulse of upward acceleration

[9] A phaseless filter is created by running the digitized signal twice through the filter, first forward and then backwards. Thus a four-pole phaseless filter gives the same frequency rolloff as an eight-pole conventional filter and does so with no phase distortion.

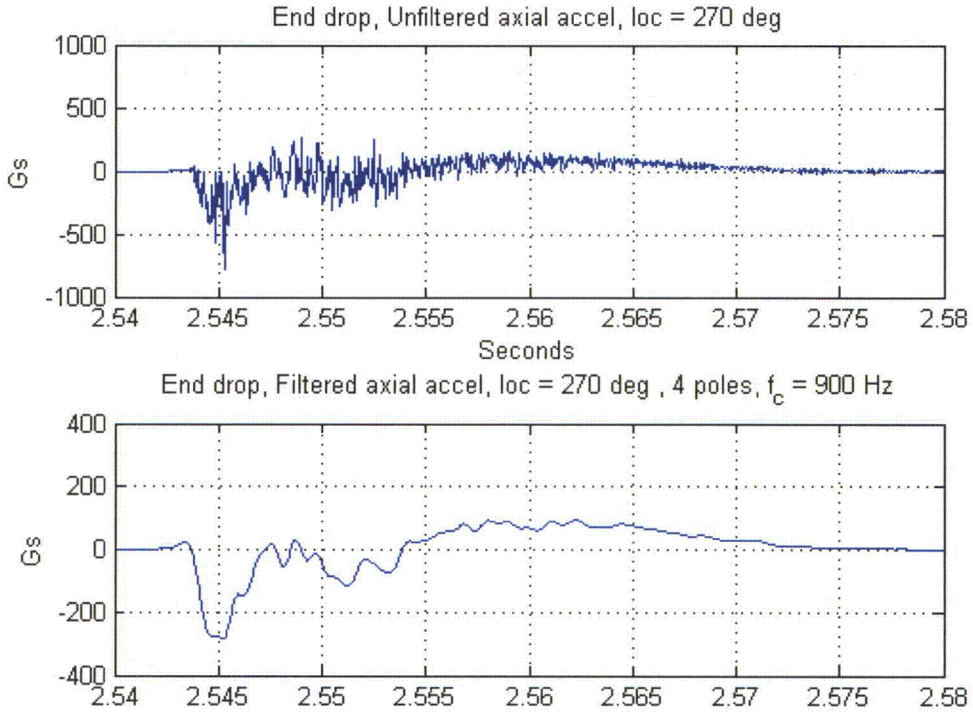

Figure 27 Signal from the axial accelerometer inside the cask on the 270-degree aximuth before (top) and after (bottom) low-pass filtering.

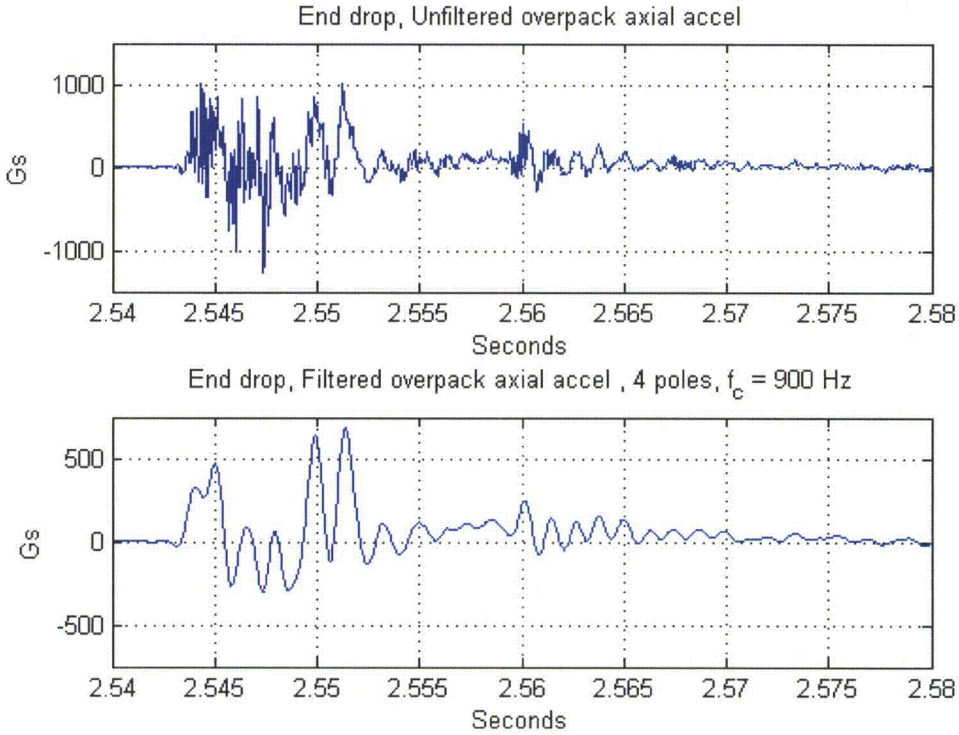

Figure 28 Signal from the axial accelerometer on the impact limiter before (top) and after (bottom) low-pass filtering.

corresponding to the initial deflection of the impact limiter and compression of the steel wool packing. However a millisecond later a secondary collision occurs as the packing goes solid and the tungsten bricks strike the lid end of the cask (recall that the cask is upside down) driving it downwards into the ground. The phenomenon is similar to a car accident where the occupants don't have their seat belts buckled, except that in this case the "occupants" are the heavy tungsten bricks. The secondary collision causes the large negative spike. Following that, a much longer period of upward acceleration occurs, which corresponds to the decay in the initial downward impact velocity. The signal corresponding to this latter positive acceleration is slightly attenuated by the AC coupling of the accelerometers themselves and also by the AC coupling of the signal to the data acquisition system.

The effect of secondary collisions is even more pronounced in the side and slap-down drops presented later, probably because the tungsten bricks are restrained less in the tangential and radial directions than they are in the axial direction.

An important feature of the peak acceleration due to the secondary collision is that it is not heavily dependent on the characteristics of the impact limiter. The spike is caused by several heavy, rigid bodies (the tungsten bricks) striking another (the stainless steel body of the cask) with the accelerometer rigidly mounted to the latter. This factor should be kept in mind in attempting to compare measured peak accelerations to analytical predictions, where the latter assume that all energy absorption is done by the impact limiter.

The effect of the secondary collisions is much less pronounced in the axial acceleration measured on the impact limiter (Figure 28), probably because the surface of the impact limiter mounting the accelerometer is only loosely coupled to the cask body. At this surface, the initial pulse of acceleration is quite large and is in the upward direction as one would expect.

6.2 High-speed video

Figure 29 shows frames from one of the four high speed video cameras. Because the impact trigger was a last-minute addition after this first test, there is no accurate way to time-align the end-drop acceleration time history to the video frames. However based on that alignment for the side and slap-down drops, the initial impact is estimated to occur at t = 2.542 seconds in the traces of the last five figures.

Using the video and the length scales, it was determined that the cask bounced to a height of about 43 inches, indicating that about 90% of the kinetic energy was dissipated upon initial impact. After the first bounce, the cask teetered on one corner and then fell over on its side, crushing the umbilical cable from the accelerometers. Fortunately, the important acceleration event was over by this time and had been recorded.

A video editing program[10] was used to estimate the elapsed time from first impact to the point where the vertical velocity of the cask c.g. dropped to zero. It was 0.021 +/-0.004 seconds. Time resolution (time between frames) was 0.001 seconds in the video used for this estimate.

[10] Imaging Studio version 2.4.0, AOS Technologies AG

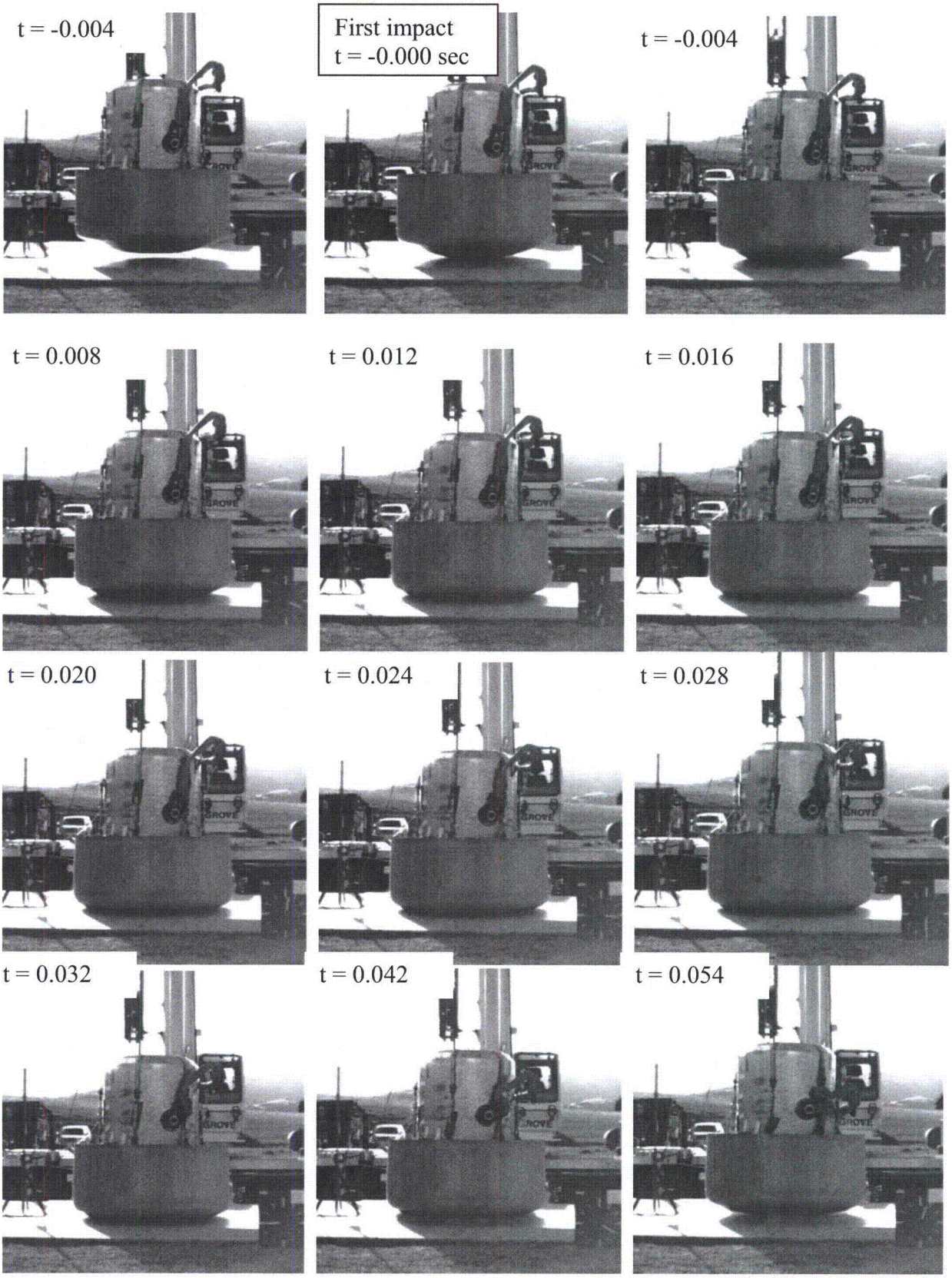

Figure 29 Frames from high-speed video of end drop.

6.3 Pressure sensing film

Figure 30 shows the pressure sensing film from the end drop. The band of film that was taped to the cylindrical surface of the cask (Figure 19) has been cut into four equal pieces which are placed in their respective azimuthal locations in Figure 30. In Figure 30 and in the similar photographs from the side and slap-down drops, the surface of the film which faced away from the cask is towards the camera.

Figure 30 Pressure sensing film removed from the cask after the end drop.

The red areas on the film indicate where contact occurred between the cask and impact limiter. The radial "spoke" impressions made by the 12 strengthening ribs inside the impact limiter are clearly visible on the circular piece of film from the flat end surface of the cask. The picture also shows that significant forces between the cask and impact limiter occurred on the conical surface produced by the chamfer on the end of the cask. The package struck with its axis nearly vertical which accounts for the fact that there was relatively little contact between the cask cylindrical surface and the inside diameter of the impact limiter.

6.4 Deformation measurements

Table 1 shows the measured cask profile deviation from the design nominal before and after the end drop. The conclusion from these measurements was that no significant damage to the cask had occurred.

Table 3 Before and after end-drop measurements of the cask.

	Cask state at measurement	
		After end drop
Deviation	Before end drop	Before side drop
Maximum	0.0068	0.0046
Minimum	-0.0094	-0.0101

Figure 31 shows an overlay of the profile of the impact limiter before and after the end drop.

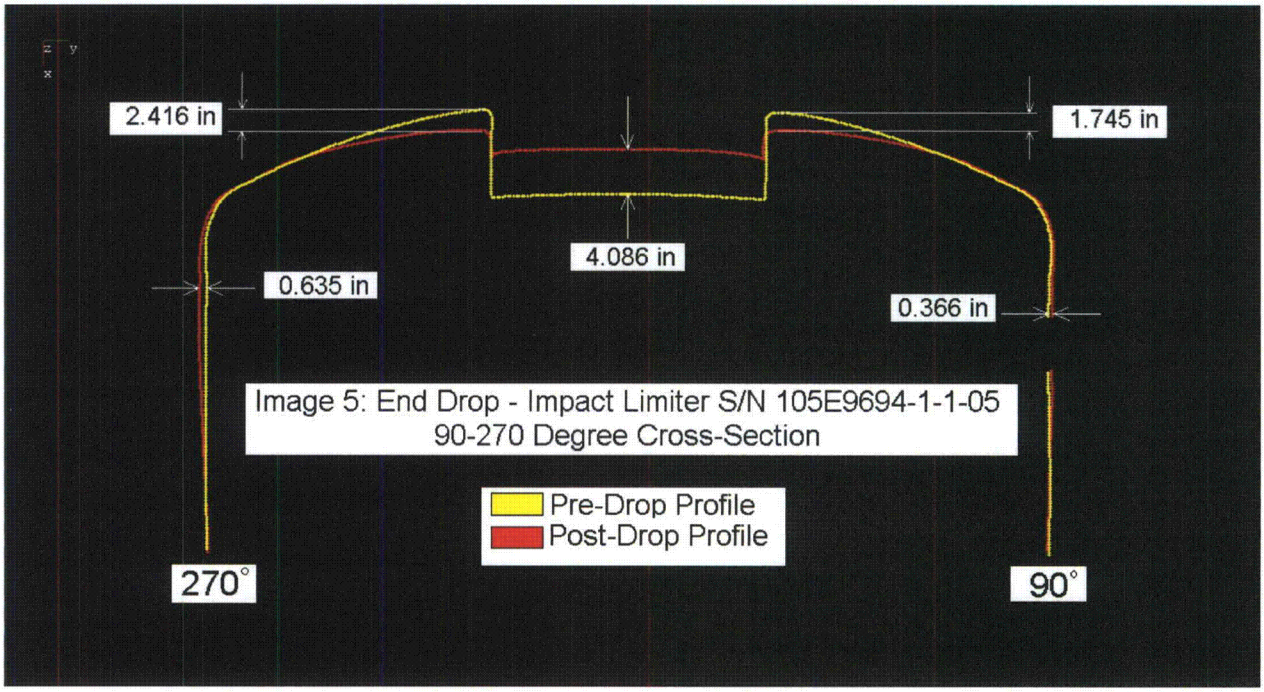

Figure 31 Profiles of the impact limiter before and after the end-drop

Figure 32 shows the impact end of the impact limiter after the end drop. The previously flat surface in the large center relief on the end of the impact limiter has been bulged out over four inches by the force from the cask transmitted through the foam. The weld around the edge of the relief has split over a small part of the circumference.

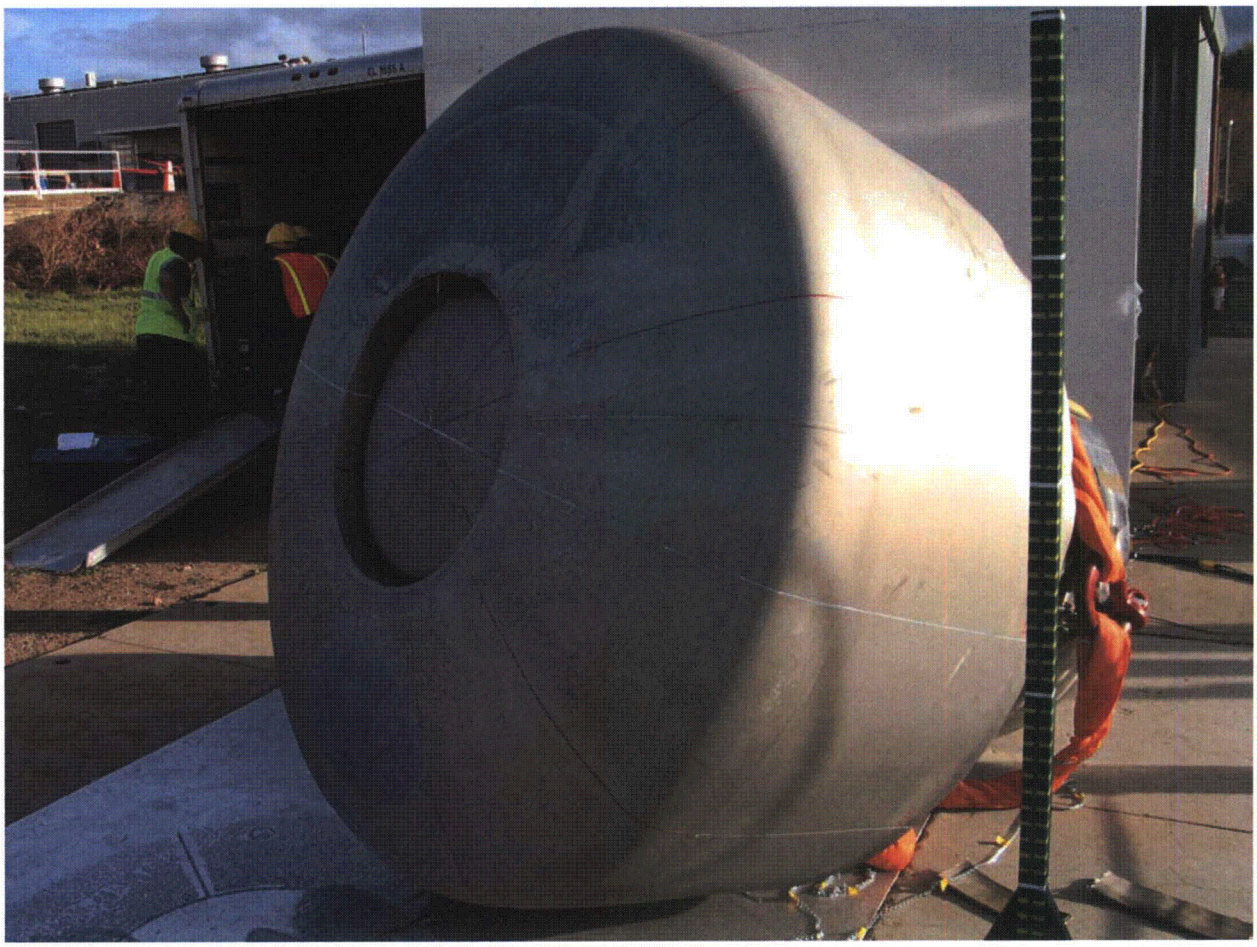

Figure 32 Cask and impact limiter immediately following the end drop.

6.5 Leak rate test

The cask was leak tested following the end drop and was found to meet specification. It was concluded that no degradation had occurred in the seal integrity of the cask.

7. Results: Side drop

7.1 Acceleration measurements

For the side drop, the two radial accelerometers inside the cask were oriented in the vertical direction but facing in opposite directions. The sensor at 90 degrees azimuth faced downwards so upwards acceleration gave a negative signal. Figure 33 shows the signals from these two sensors during the initial impact.. Initial contact as sensed by the impact trigger was at time = 0.1217 seconds[11] in the plot.

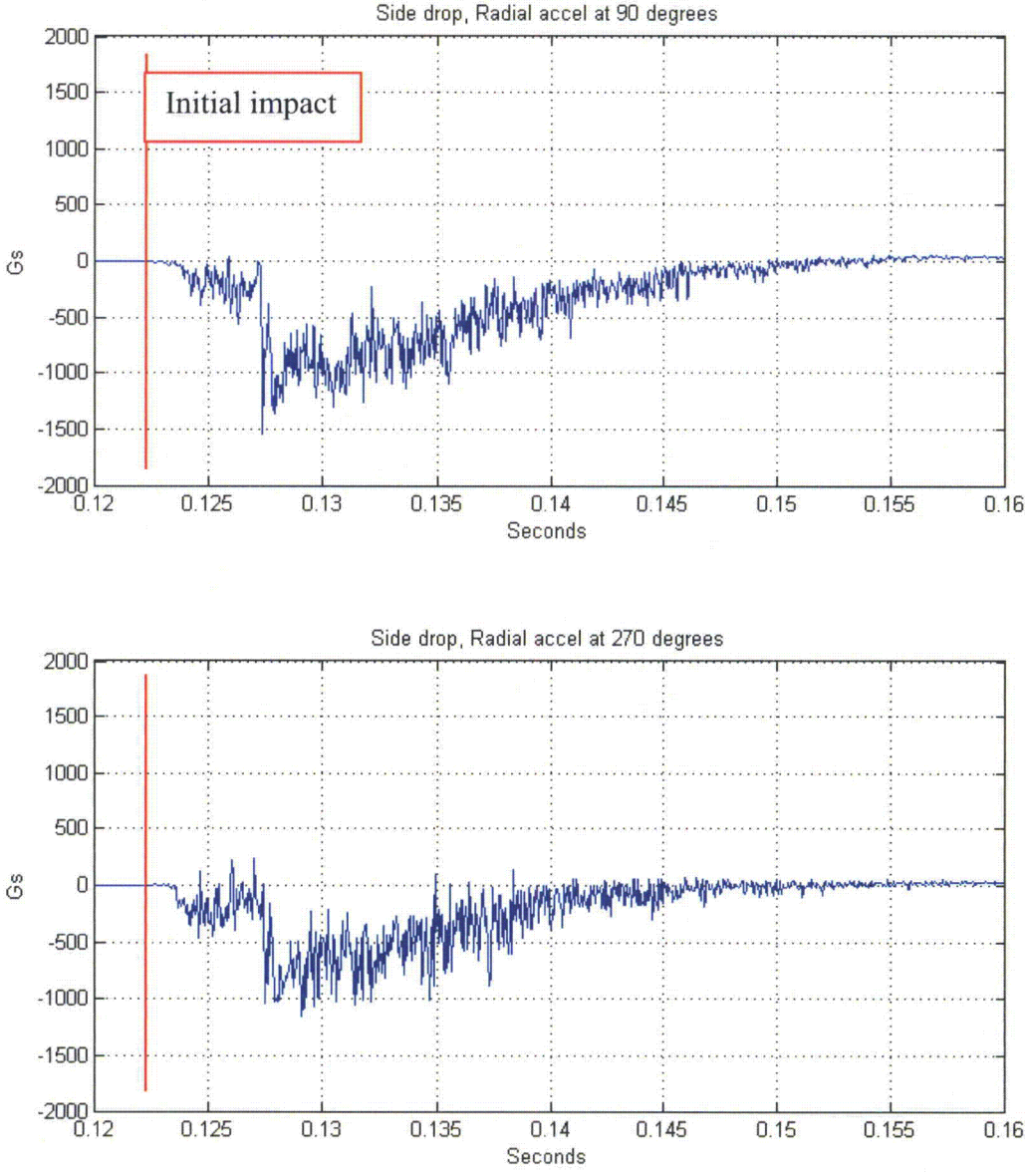

Figure 33 Vertical accelerations measured at impact inside the cask for the side drop.

[11] The t = 0 origin is arbitrary but is the same for all acceleration signals on a given drop.

Figure 34 shows the triaxial signals from the sensors on the impact limiter. The radial sensor on the impact limiter is essentially vertical and faces downward, like the in-cask accelerometer at 90 degree azimuth, so upwards acceleration gives a negative signal.

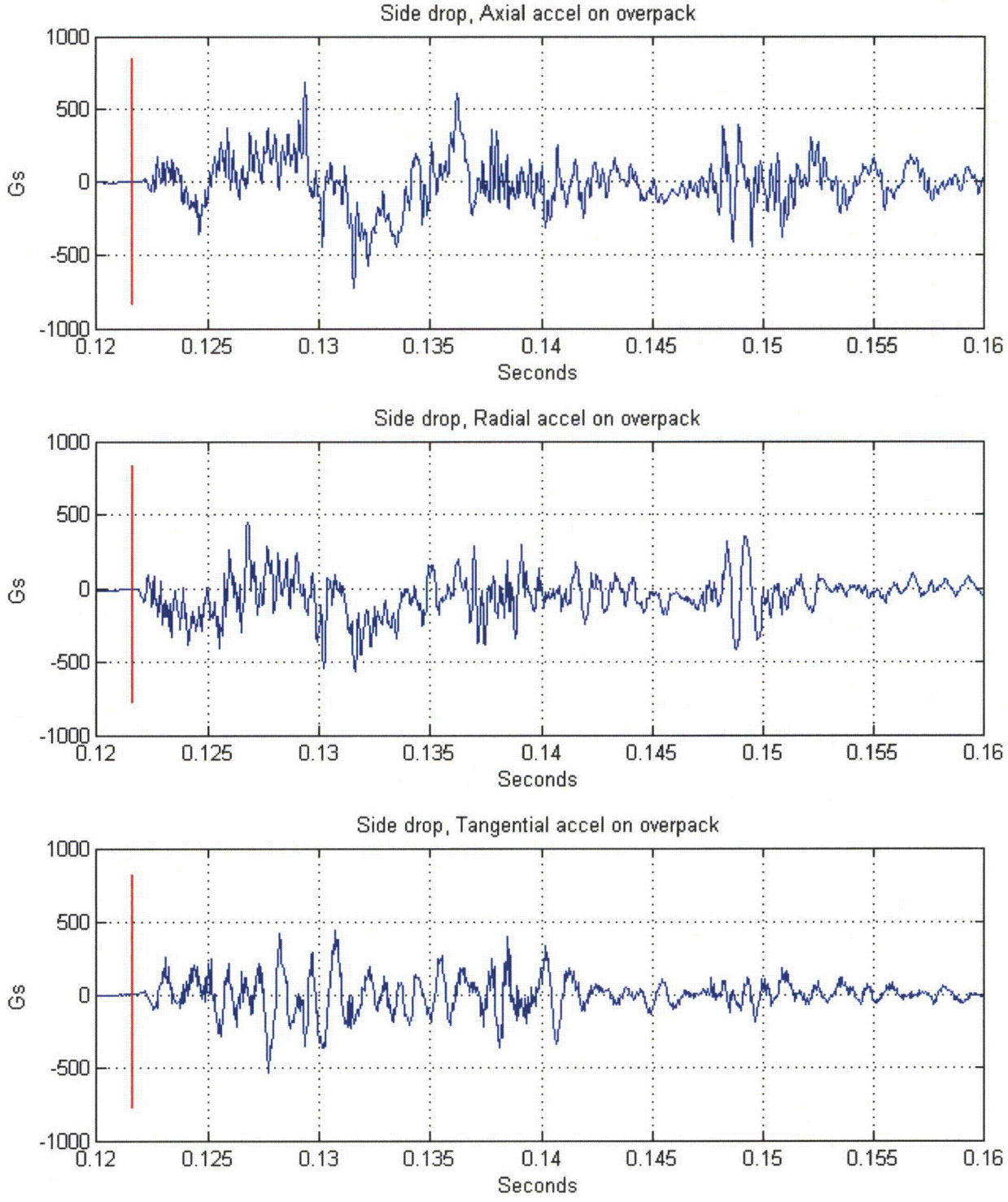

Figure 34 Accelerations measured on the impact limiter during the side drop.

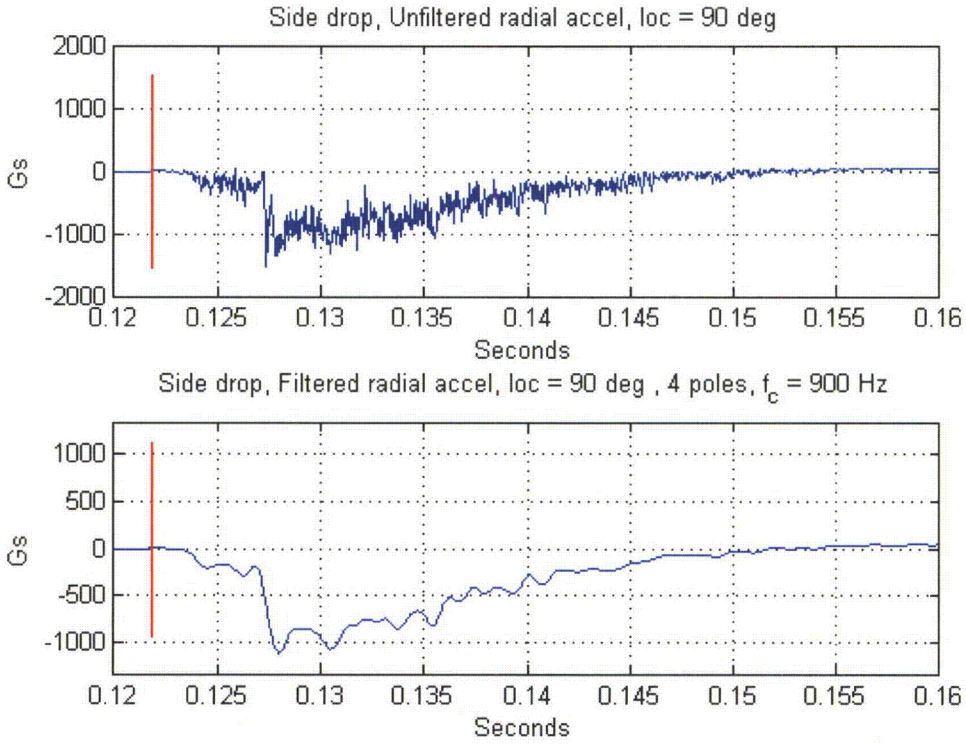

Figure 35 Signal from the radial in-cask accelerometer at 90-degree azimuth for the side drop, unfiltered (top) and low-pass filtered (bottom).

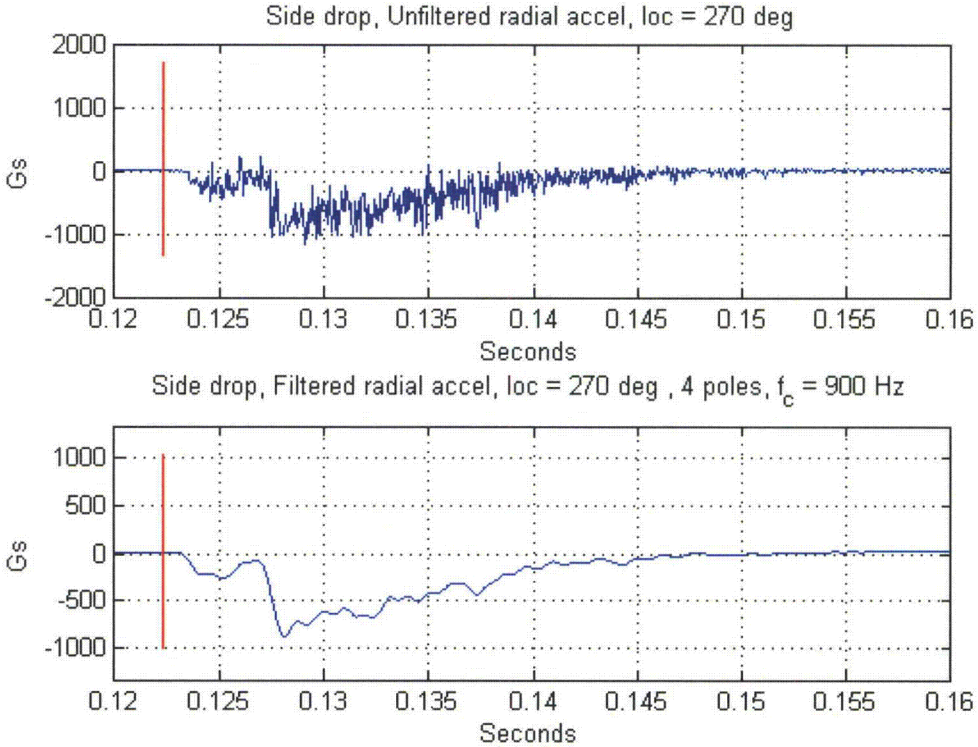

Figure 36 Signal from the radial in-cask accelerometer at 270-degree azimuth for the side drop, unfiltered (top) and low-pass filtered (bottom).

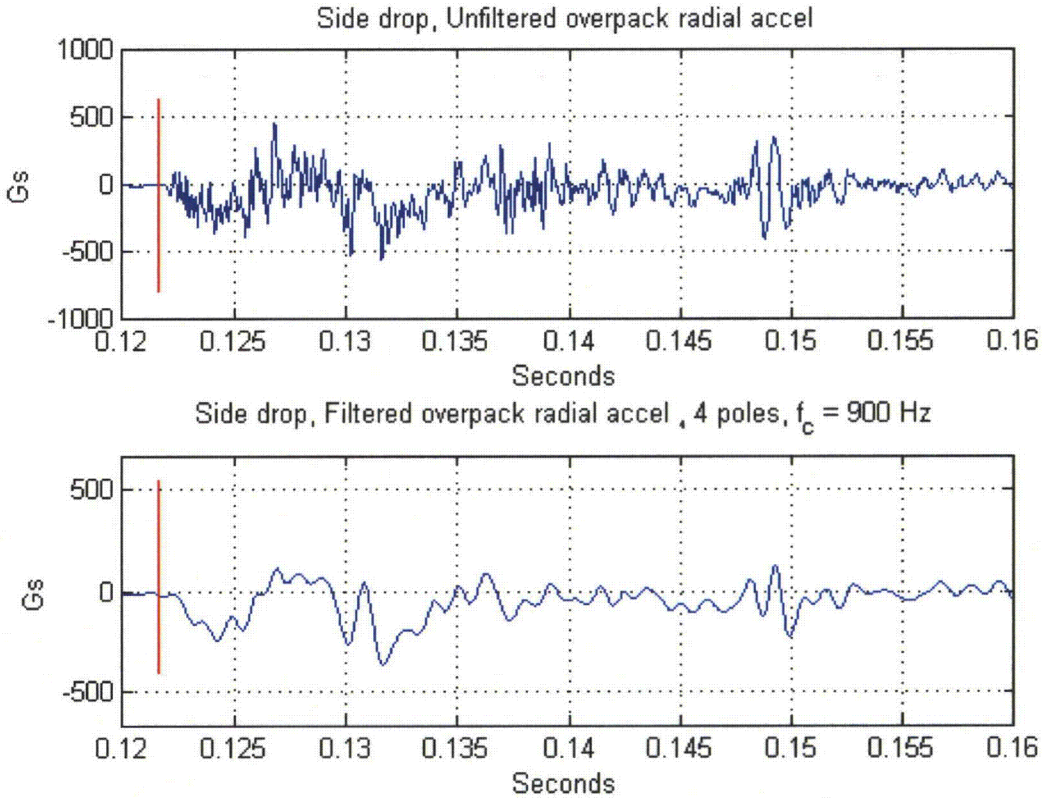

Figure 37 Signal from the radial accelerometer on the impact limiter, unfiltered (top) and low-pass filtered (bottom).

Figure 35, Figure 36, and Figure 37 show unfiltered and filtered signals from the three vertical accelerometers. The most important feature of these signals is that the in-cask accelerometers all over-ranged. They hit their 1000-g limit at time equal to approximately 0.127 seconds when a sudden negative step occurred in the acceleration. Typically with ICP accelerometers, the signal following such an over-range is not valid for a few tenths of a second. Thus, the only thing that can be said with certainty regarding cask acceleration is that it exceeded 1000 g's at the sensor location. This high level was probably caused by the secondary collisions between the heavy tungsten bricks of the shielding layer and the steel body of the cask. It's likely that the steel wool packing did not restrain the tungsten bricks as well in the radial and tangential directions as it did in the axial direction. This would account for the higher peak levels seen in the side drop compared to the end drop.

Referring to Figure 35 and Figure 36, the initial and secondary impacts are clear. The initial impact gives a peak acceleration of about 250 g's and the secondary impact gives over 1000 g's (over-range). However there is one unresolved anomaly in the data. Both radial signals go negative at both initial and secondary impacts. However the two sensors face in opposite directions and thus have signals of opposite polarities relative to upwards. One would expect their signals to be approximately the negatives of each other, at least during the initial smaller impact. At present there is no explanation for this pattern, which also occurred in the slap-down drop.

Figure 38 Cask and impact limiters following the side drop.

Figure 38 shows the cask with impact limiters after the drop. Three of the six heavy steel turnbuckles holding the impact limiters against the cask failed when their clevis pins sheared. This allowed the lower parts of the two impact limiters to move away from each other. This may have caused another secondary impact effect when the impact limiters rotated outwards as far as they could and jammed against the cask outer diameter, thus suddenly stopping the descent of the heavy cask.

7.2 High-speed video

Figure 39 shows frames from one of the three high-speed video cameras. The impact time denoted as t = 0.000 seconds in the video frames corresponds to t = 0.1217 seconds in the acceleration time histories. The video sequence shows clearly how the lower sides of the two impact limiters pulled away from each other at impact, causing the lower turnbuckles to fail. This may have been due to a wedging action of the chamfered ends of the cask against the conical section of the mating recess in the impact limiters. It might also have been caused by the centroid of the impact force against the lowest surface of each impact limiter being outboard of the cask ends, causing a rotational moment on the impact limiters.

Since there is only about ¼ inch of diametral clearance between the cask OD and the impact limiter ID, the outward rotation of the impact limiters would come up against a hard limit, which may have contributed to the secondary impact.

Following the initial impact, the package bounced to a height of about 17 inches, indicating that over 95% of the kinetic energy had been dissipated.

Using the video editing program, the elapsed time was estimated between initial impact and the instant when the cask c.g. reached zero vertical velocity. That time was 0.022 +/-0.004 seconds. The resolution of this measurement (i.e. the time between frames) was 0.002 seconds.

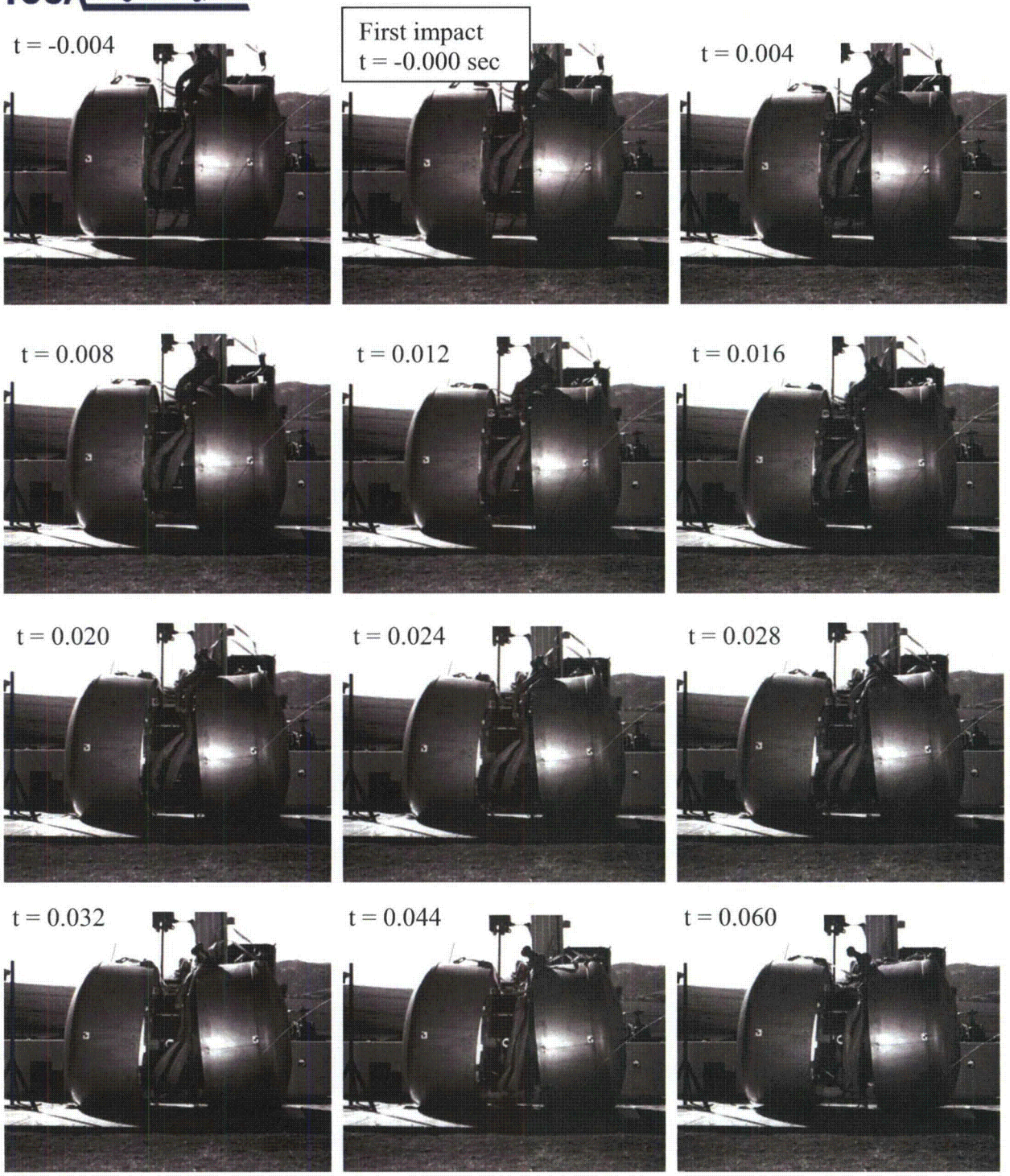

Figure 39 Frames from high-speed video of side drop

7.3 Pressure sensing film

Figure 40 shows the pressure sensing film from the side drop. Most of the impact was taken on the downward-facing part of the cask cylindrical surface (on the right in the photos), and on the

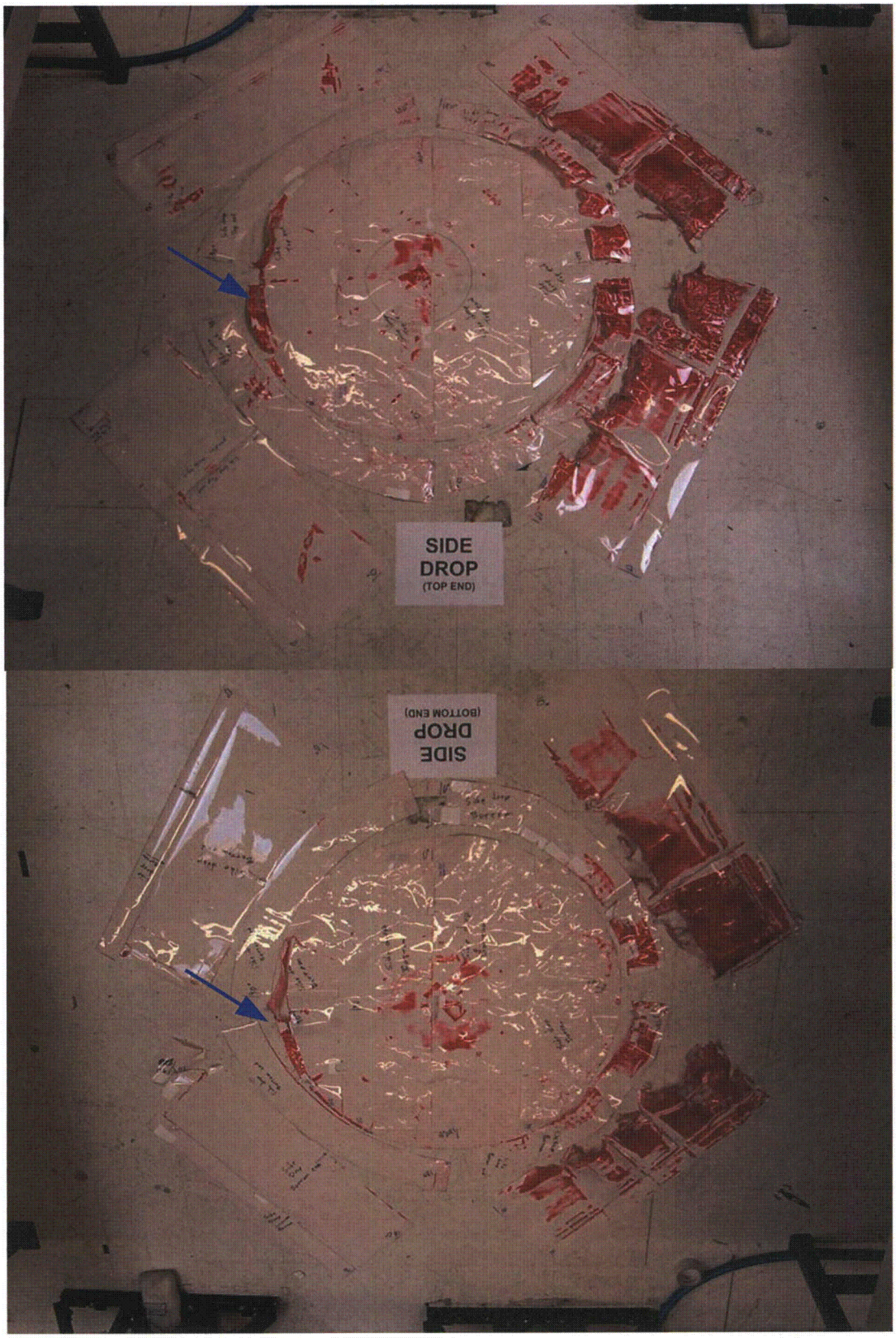

Figure 40 Pressure sensing film removed from the cask after the side drop.

downward facing part of the conical surface, as would be expected. However, there is also a significant amount of red on the paper that was on the uppermost part of the flat, circular end surfaces of the cask (blue arrows in the figure). Pressure against these areas is further evidence of secondary impact after the turnbuckles failed, the impact limiters rotated outwards, and their lower parts moved away from each other.

7.4 Deformation measurements

Table 4 shows the measured cask profile deviation from the design nominal before and after the side drop. The conclusion from these was that no significant damage to the cask had occurred.

Table 4 Measurements of the cask before and after side-drop.

	Cask state at measurement	
	After end drop	After side drop
Deviation	Before side drop	Before slap-down drop
Maximum	0.0046	0.0053
Minimum	-0.0101	-0.0109

Figure 41 shows one of the impact limiters after removal from the cask. One of the welds between the conical and cylindrical sections has split open, revealing the energy absorbing foam within. Figure 42 shows an overlay of the measured impact limiter profiles before and after the side drop.

Figure 41 Damage to impact limiter from side drop.

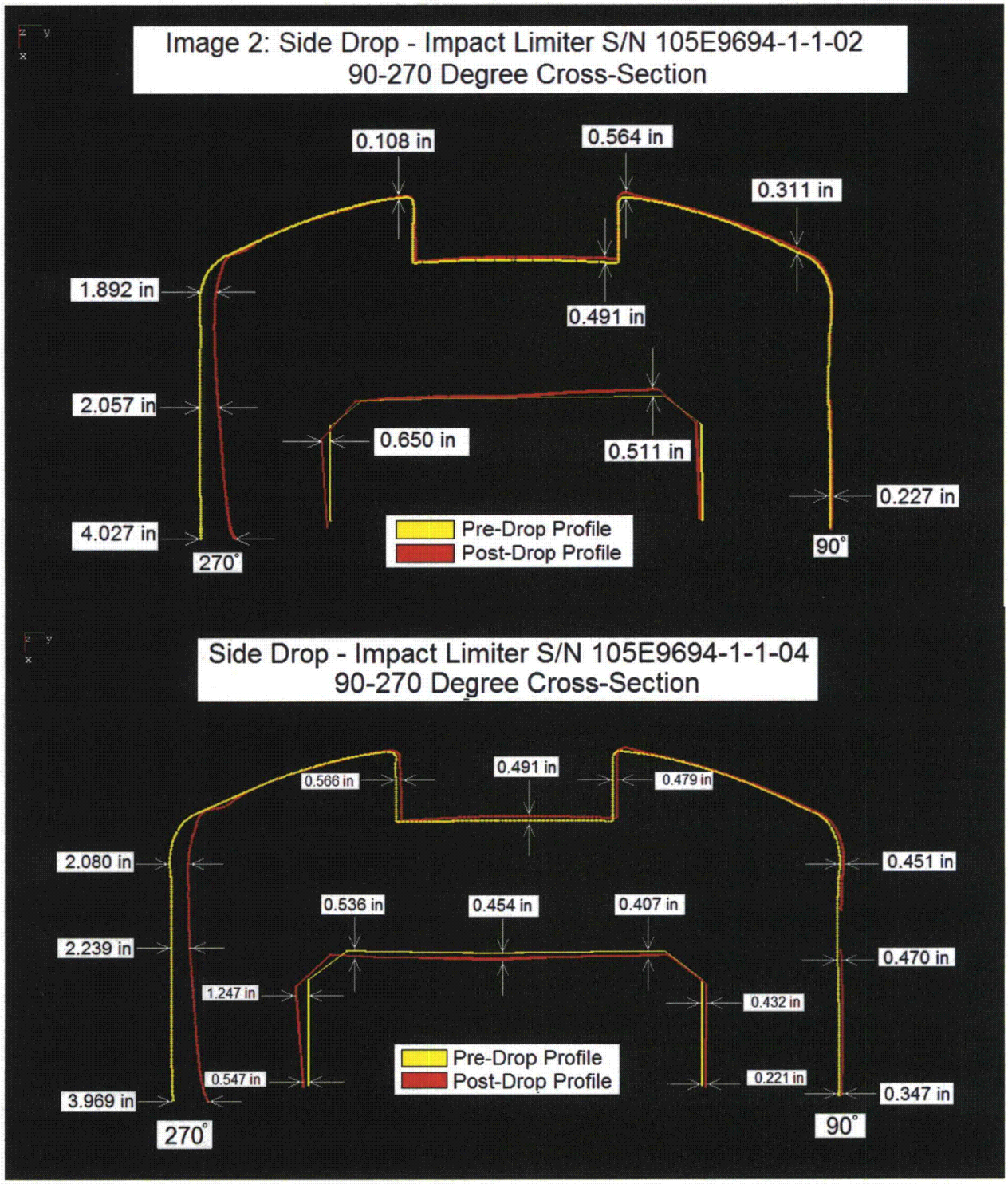

Figure 42 Profiles of the impact limiters before and after the side drop.

7.5 Leak rate test

The cask was leak tested following the side drop and was found to meet specification. It was concluded that no degradation had occurred in the seal integrity of the cask.

8. Results: Slap-down drop

Figure 43 Package rigged for the slap-down drop.

Figure 43 shows the package rigged for the slap-down drop. The weight of the package is held by the brown rigging straps which lift at the cask trunnions. The yellow straps on either side were adjusted to hold the package such that its left end was about 10 inches higher than its right end. This had been determined by analysis to be the worst case. The lid end of the cask is on the left in the photo. The impact limiters on the left and right will be referred to as the "lower" and "higher" respectively.

8.1 Acceleration measurements

For the slap-down drop, the two radial accelerometers inside the cask were oriented 7.7 degrees off the vertical direction, facing in opposite directions. The sensor at 90 degrees azimuth faced

downwards so upwards acceleration gave a negative signal from this sensor. Figure 44 shows the signals from these two sensors.. Initial impact was at time = 0.0746 seconds

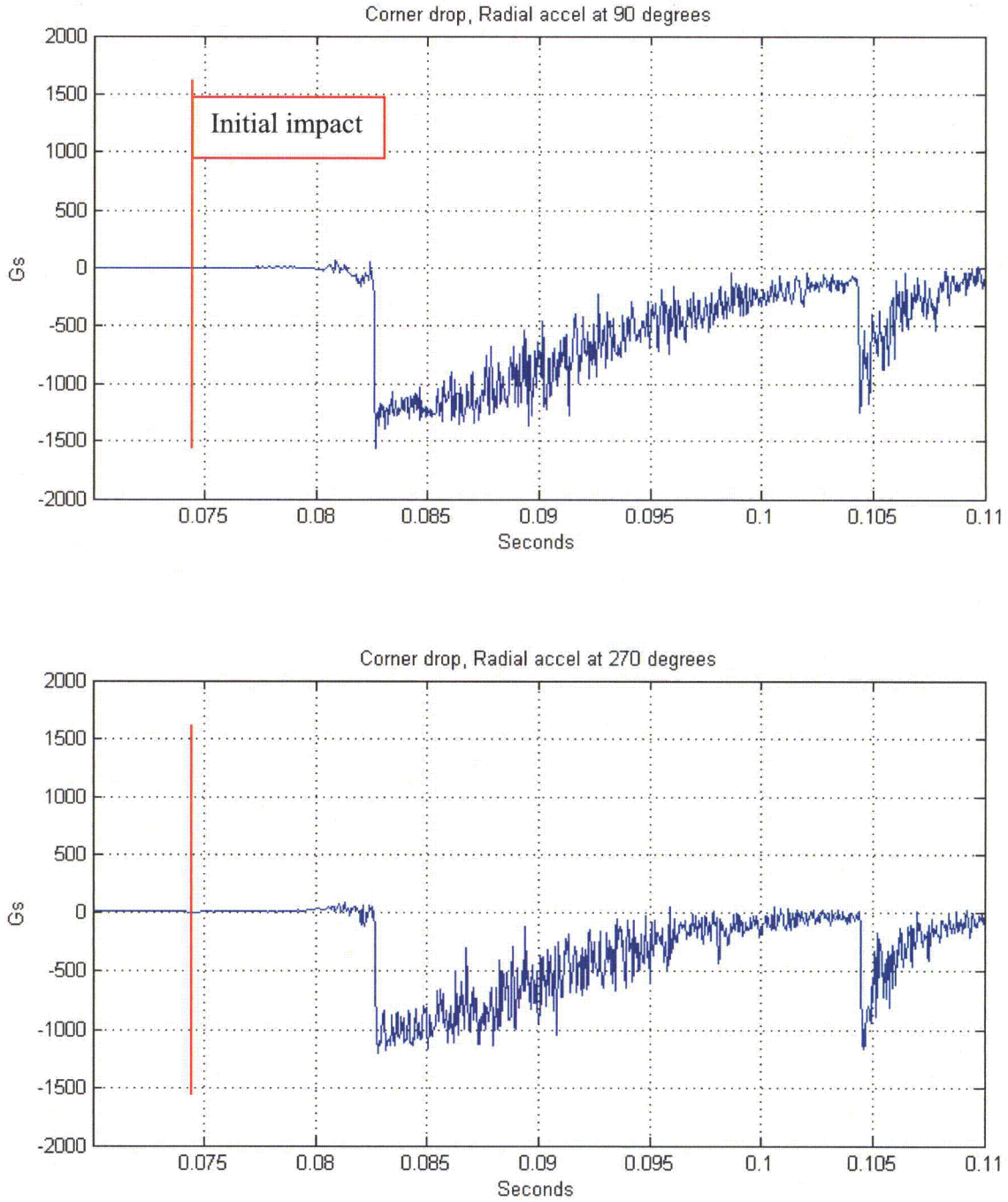

Figure 44 Near-vertical accelerations measured nside the cask for the slap-down drop.

Figure 45 shows the triaxial signals from the sensors on the impact limiter. The radial accelerometer on the impact limiter is again closest to vertical and faces downward. Upwards acceleration gives a negative signal from this sensor.

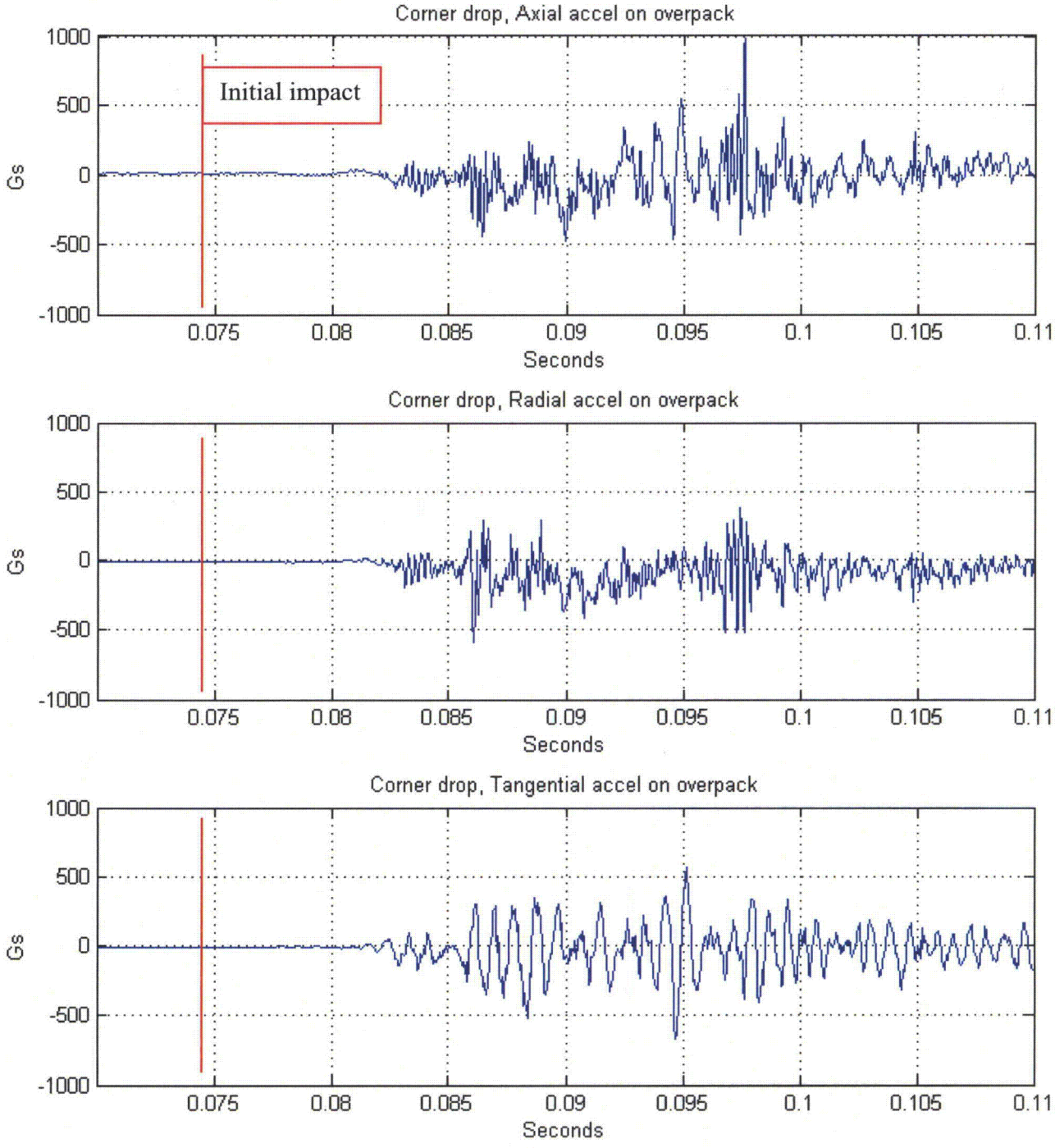

Figure 45 Accelerations measured on the impact limiter during the slap-down drop.

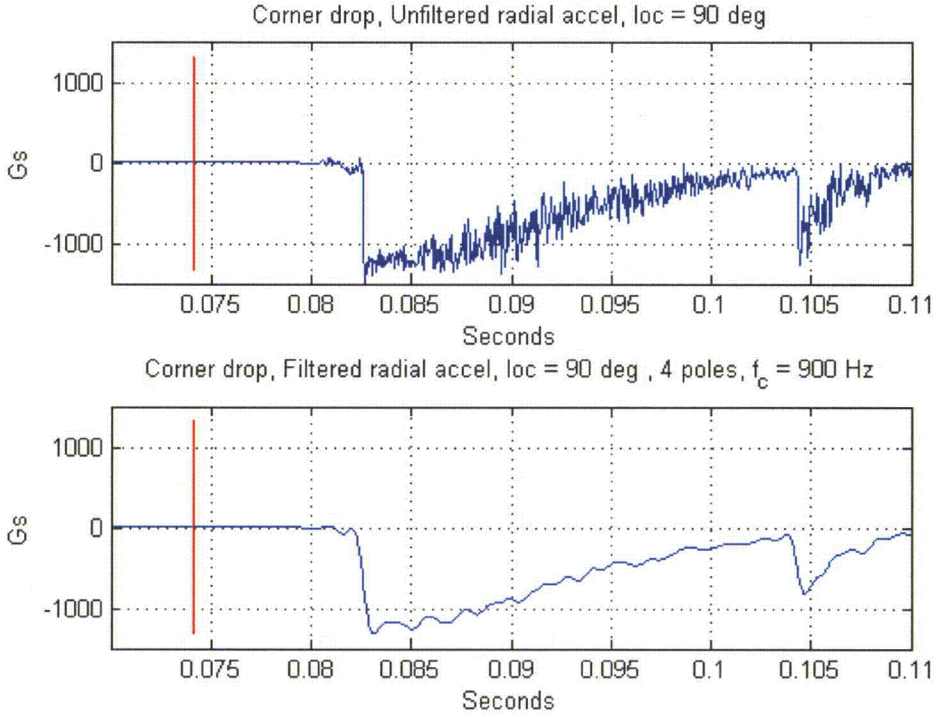

Figure 46 Signal from the radial in-cask accelerometer at 90-degree azimuth for the slap-down drop, unfiltered (top) and low-pass filtered (bottom).

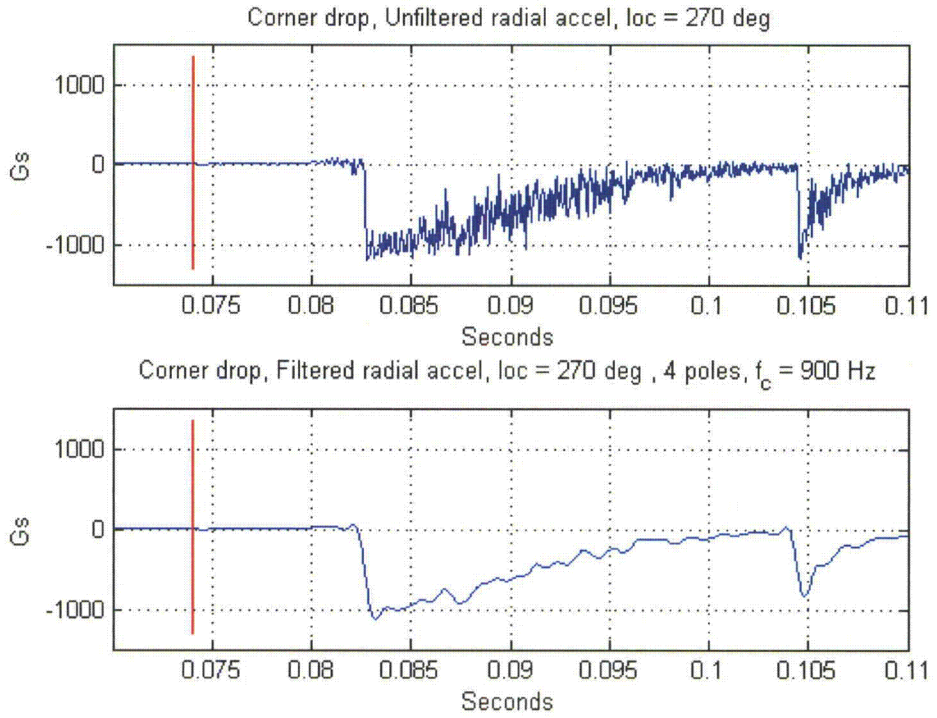

Figure 47 Signal from the radial in-cask accelerometer at 270-degree azimuth for the slap-down drop, unfiltered (top) and low-pass filtered (bottom).

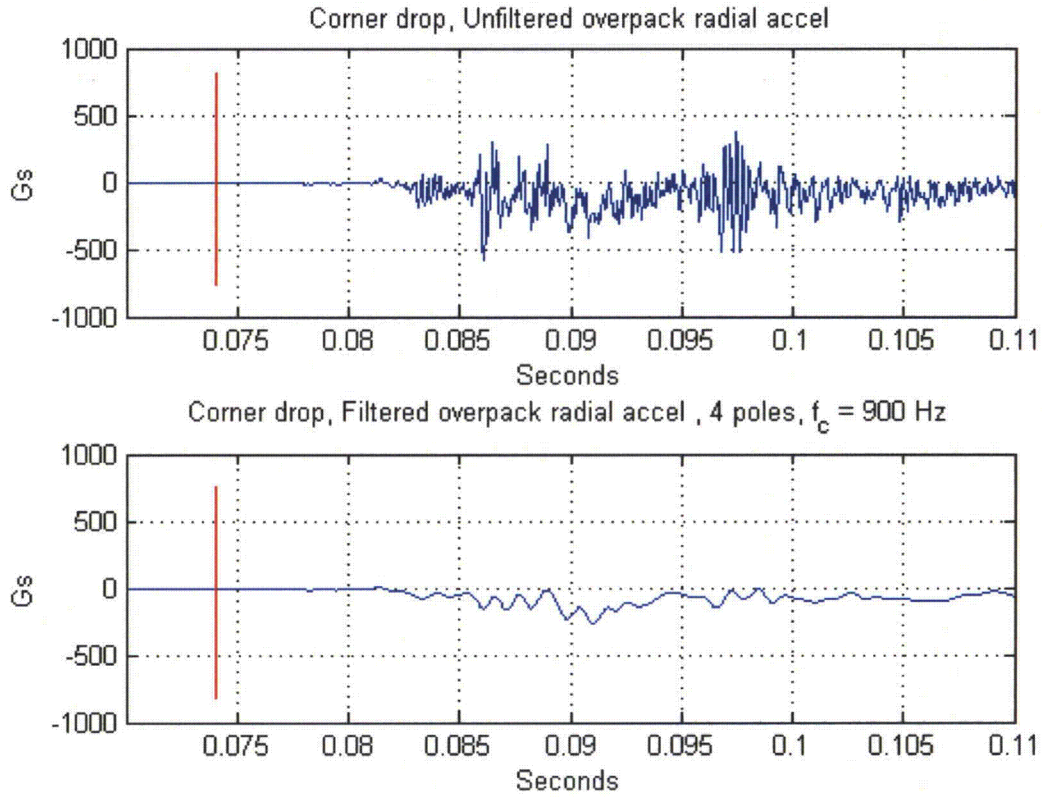

Figure 48 Signal from the radial accelerometer on the impact limiter during the slap-down drop, unfiltered (top) and low-pass filtered (bottom).

Referring to Figure 44, there are two major events, one at 0.0822 seconds and one at 0.1042. seconds. Comparing this time interval to the high-speed video (Figure 49), these two impacts are obviously due to the initial strike of the lower impact limiter (on the left in Figure 49) and the strike of the higher impact limiter (on the right in Figure 49). Like the side drop, the initial impact causes the accelerometers to over-range so the only quantitative conclusion that can be drawn is that the accelerometers saw over 1000 g's. The exact peak level in unknown.

The slap-down drop also produced the same unexplained polarity as the side drop: both in-cask radial accelerometer signals went negative at the major impact events. Taken literally, these signals would indicate that the round cross section of the cask ID was deforming suddenly into an oval, with the 90 and 270-degree azimuthal locations moving away from each other. At present, there is no satisfactory explanation for this phenomenon.

8.2 High-speed video

Figure 49 shows frames from one of the three high-speed video cameras from the slap-down drop. The impact time denoted as t = 0.000 seconds in the figure corresponds to t = 0.0746 seconds in the acceleration time histories. The turnbuckles holding the impact limiters for this

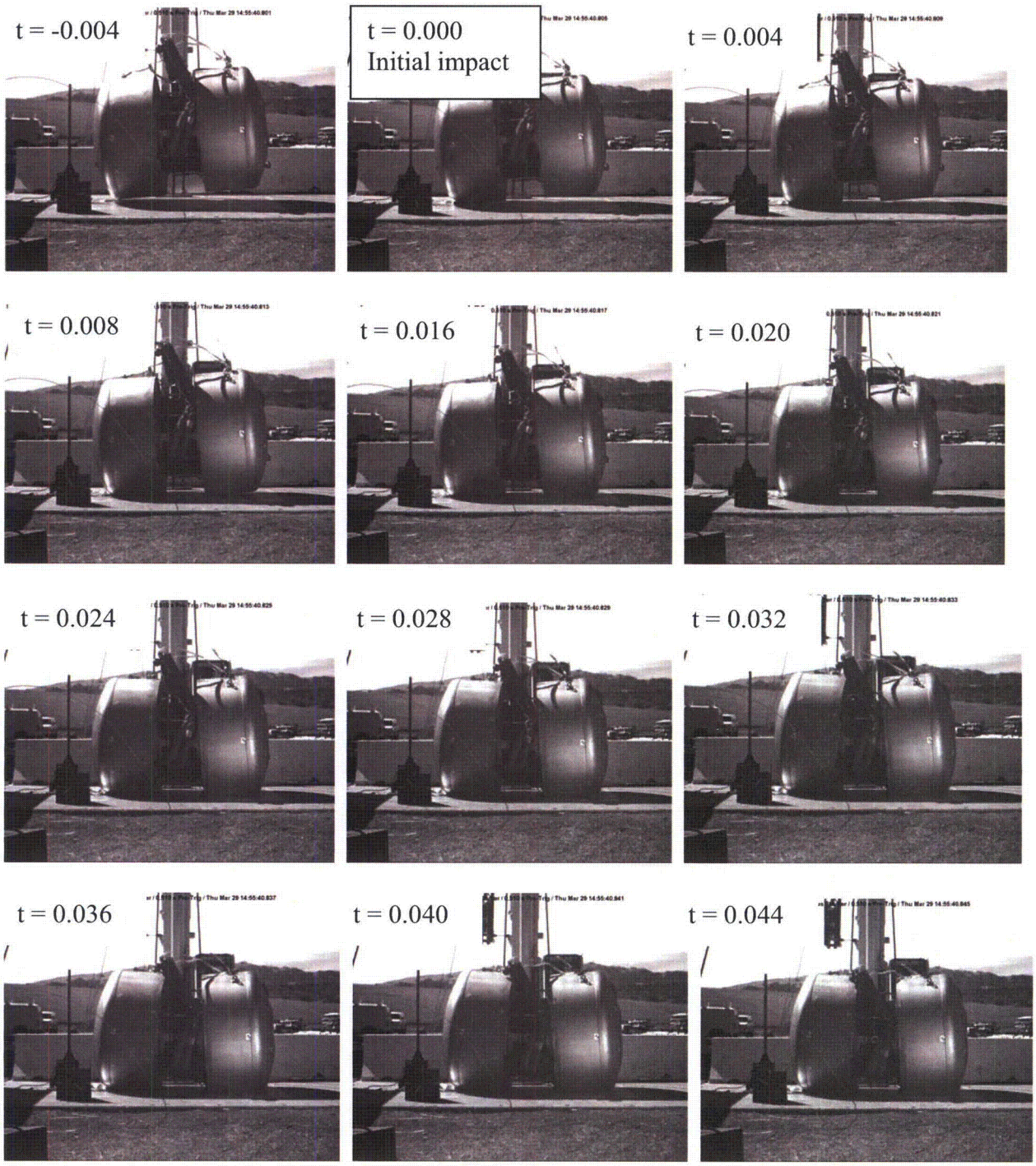

Figure 49 Frames from high-speed video of slap-down drop.

drop used heavier clevis pins which did not break on impact. However the upper turnbuckles buckled which caused them to become shorter so there was still considerable relative rotation between the two impact limiters, as evident in the video frames. Figure 50 shows the uppermost turnbuckle following the drop.

Using the video editing program, the elapsed time was estimated between initial impact and the instant when the cask c.g. reached zero vertical velocity. That time was 0.028 +/-0.004 seconds. Unlike the first two drops, the cask kinetic energy had not been completely dissipated at the zero velocity instant since there was still significant rotational velocity present. The resolution of this measurement (i.e. the time between frames) was 0.002 seconds.

Figure 50 Uppermost turnbuckle after the slap-down drop.

Figure 50 also shows how the wires from the in-cask accelerometers were crushed and cut by being pinched between the impact limiter and the cask. In this case the relative rotation between the impact limiters and the cask was sufficient to pinch the cables, in spite of the 1/8th-inch-diameter protective rods on either side of the cable. Figure 50 shows that the diametral clearance between cask and impact limiter has been increased to well over an inch by deformation of the impact limiter. In an undeformed impact limiter, this clearance is only about 1/4th inch. Fortunately, the cable fault did not occur until about 25 milliseconds after the end of the main acceleration event so the important data was recorded.

Following the impact of the higher impact limiter against the ground, the package rotated counterclockwise (in the view of Figure 49) and its mass center rose approximately 25 inches,

indicating that about 93.3 percent of the kinetic energy was dissipated. Figure 51 shows the highest point in the first bounce.

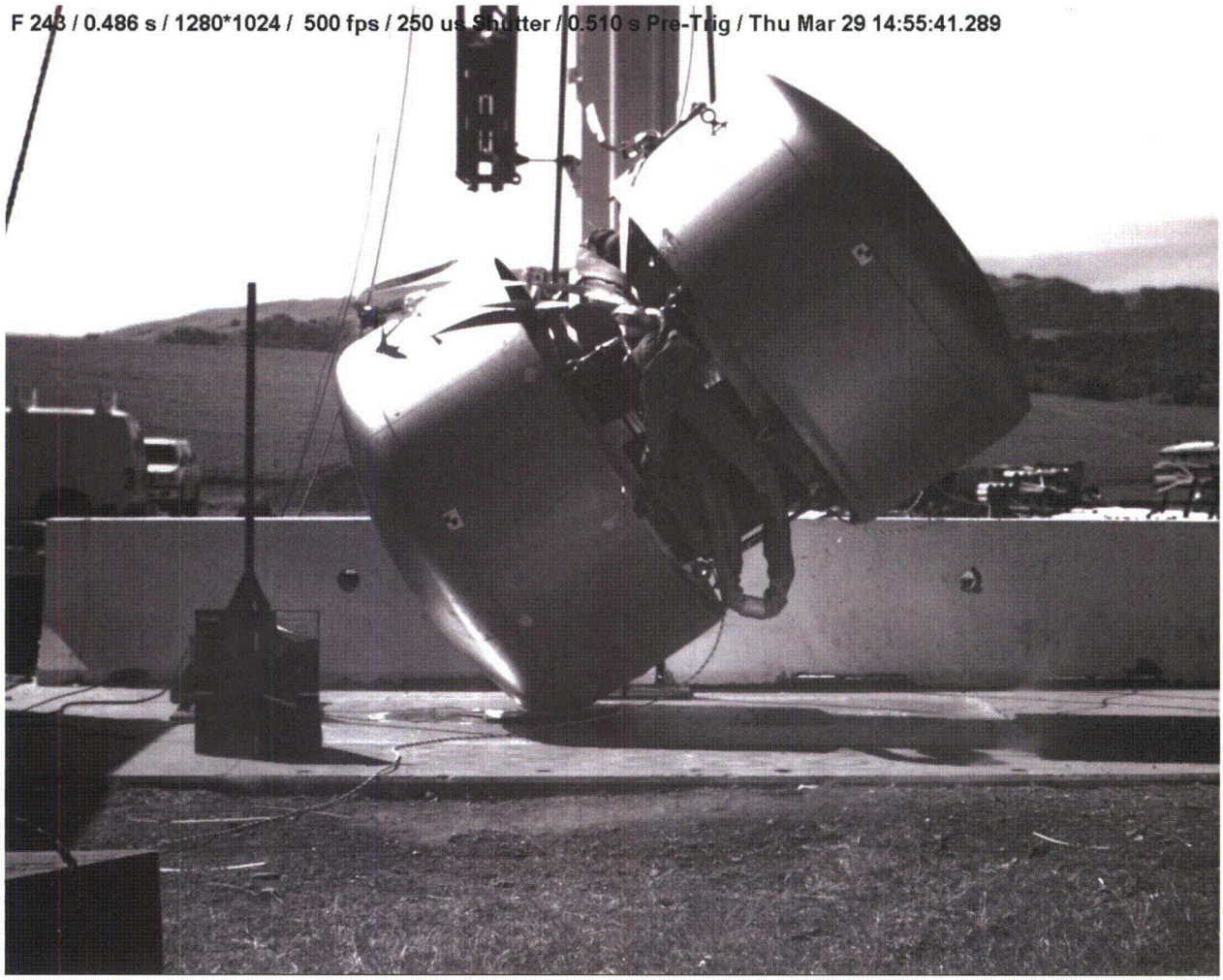

Figure 51 Highest point in the first bounce during the slap-down drop.

8.3 Pressure sensing film

Figure 52 shows the pressure sensing film removed after the slap-down drop. The pattern of pressure between the cask and impact limiter is quite similar to that from the side drop.

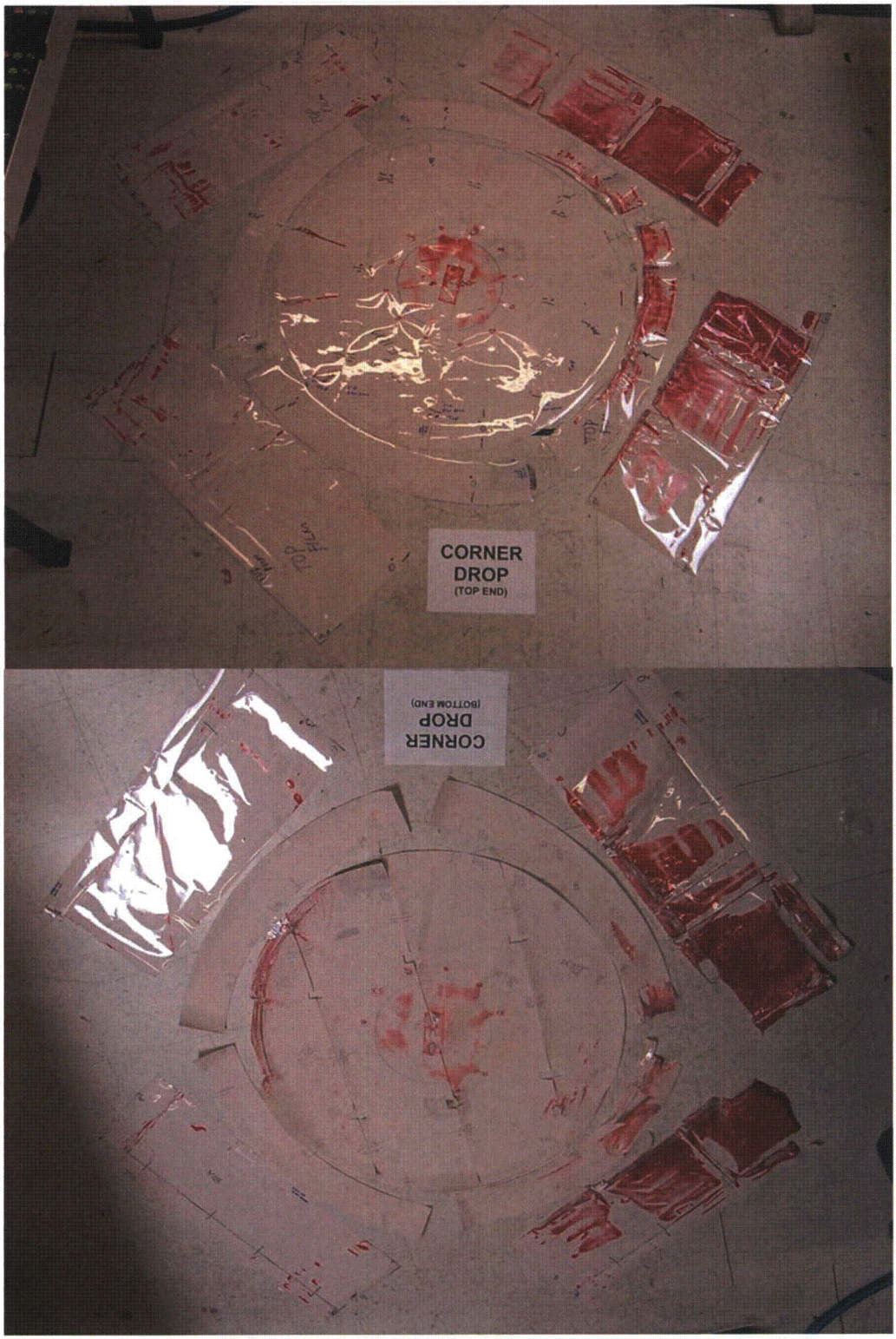

Figure 52 Pressure sensing film removed from the cask and impact limiters after the slap-down drop.

8.4 Deformation measurements

Table 5 shows the measured cask profile deviation from the design nominal before and after the slap-down drop. The conclusion from these was that no significant damage to the cask had occurred.

Table 5 Measurements of cask before and after the slap-down drop.

	Cask state at measurement	
	After side drop	After slap-down drop
Deviation	Before slap-down drop	
Maximum	0.0053	0.0047
Minimum	-0.0109	-0.0105

Figure 53 shows the deformation suffered by the impact limiter that was on the higher end of the cask. Figure 54 shows overlays of the measured impact limiter profiles before and after the slap-down drop. The lower part of the figure shows how much the inner diameter of the impact limiter was deformed when it rotated relative to the cask on impact.

Figure 53 Damage to the impact limiter from the "slap-down" end of the cask.

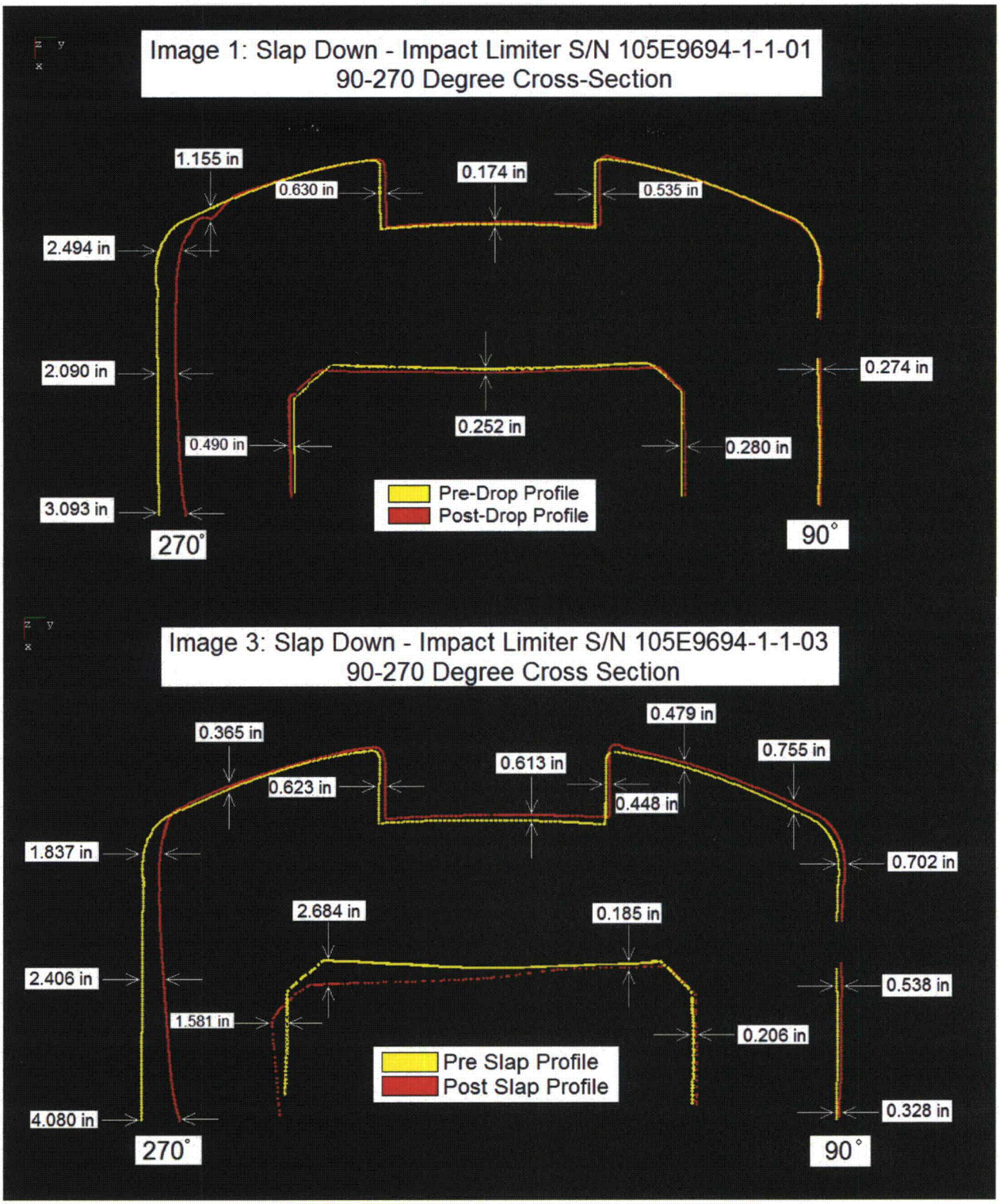

Figure 54 Profiles of the higher (top) and lower (bottom) impact limiters before and after the slap-down drop.

8.5 Leak rate test

The cask was leak tested following the slap-down drop and was found to meet specification. It was concluded that no degradation had occurred in the seal integrity of the cask.

9. Conclusions

The objectives, methods, and results of the drop test have been presented. The primary conclusions are as follows.

1. The cask and impact limiters passed the test. The cask passed its helium leak rate test before the first drop and after each of the three drops. No significant deformation of the cask was measured after any of the drops.

2. Measured peak accelerations are not usable for evaluating the accuracy of analytical predictions of cask and impact limiter behavior. Peak acceleration measured on the cask inner surface appears to be caused by secondary impacts between the internal tungsten shielding blocks and the steel cask body. The response to these impacts is not primarily dependent on impact limiter design.

3. Several measured acceleration time histories contained unexplained features. In particular, they did not exhibit a polarity consistent with the large decrease in downward velocity (i.e. upward acceleration) that had to exist at impact.

4. Two of the three drops caused accelerometers measuring in the vertical or near-vertical direction to exceed their 1000-g range. Therefore the waveform indicated by these accelerometers following the over-range is probably corrupted. The only conclusion that can be drawn from these data is that the peak acceleration exceeded 1000 g's at the sensor location. Acceleration data from the end drop is not over-ranged and should be accurate throughout the transient duration.

5. The high-speed video data allowed a reasonably accurate estimate to be made of the total elapsed time for deceleration of the cask c.g. from its impact velocity to zero. This data may be of use in evaluating the accuracy of the analytical predications.

THIS PAGE INTENTIONALLY LEFT BLANK

2.12.7 Dimensional Inspection Report

THIS PAGE INTENTIONALLY LEFT BLANK

EAST COAST
METROLOGY

461 Boston Street ♦ Topsfield, Massachusetts 01983 ♦ Tel: 978-887-5781 ♦ Fax: 978-887-5782 ♦ www.EastCoastMetrology.com

RANOR / GE Energy / AOS
AOS-165 Cask Drop Test
Dimensional Summary Report No. 109699-01 (4-23-07)

RANOR Purchase Order No.: 109699

Part Names:	AOS-165 Cask Assembly and Impact Limiters
Document References:	Drawing Nos.105E9692 Rev. 2; 105E9694 Rev. 3; Specification No. 22A9418 Rev. 3
Serial Numbers:	AOS-165 105E9693-1 (RANOR S/N 050280-01) AOS-165 105E9694-1-1-01 (RANOR S/N 060452-01) AOS-165 105E9694-1-1-02 (RANOR S/N 060452-02) AOS-165 105E9694-1-1-03 (RANOR S/N 060452-03) AOS-165 105E9694-1-1-04 (RANOR S/N 060452-04) AOS-165 105E9694-1-1-05 (RANOR S/N 060452-05)
Inspection Dates:	March 16-30, 2007
Attachments:	FARO Calibration Certificate No. 4655 (10-19-2006)

Inspection Conditions:

Location:	GE Nuclear Energy Vallecitos Nuclear Center Sunol, CA 95486
Material:	Stainless Steel
Measurement Units:	Inches

East Coast Metrology was contracted by RANOR, Inc. for performance of On-Site Laser Tracker Inspection Services of the AOS-165 Cask Assembly and Impact Limiters fabricated by RANOR. The items were located at GE Nuclear Energy Vallecitos Nuclear Center 6705 Vallecitos Road Sunol, CA 95486.

East Coast Metrology utilized a FARO Laser Tracker Model X System, Serial No. X01000601930 for performing the dimensional inspections. The equipment has been calibrated by the manufacturer - FARO Technologies Kennett Square, PA 19348 on October 18, 2006, calibration due October 18, 2007 (FARO Calibration Certificate Number 4655) using standards traceable to the National Institute of Standards and Technology (NIST).

All dimensional inspection was performed under the direction and observation of GE Nuclear Energy Raul Pomares, Project Manager for the AOS-165 Cask Assembly and components.

The AOS-165 Cask Assembly and accompanying Impact Limiters were inspected by *East Coast Metrology* before and after each drop test to determine the extent of deformation due to each type of drop. Each component was scanned and compared to its corresponding CAD model using a Laser Tracker. See the following for a summary of the inspections and data.

AOS-165 Cask Assembly:

For each set of scan data for the Cask, the 0, 90, 180, and 270 degree profiles were scanned. An alignment using the axis of the cylindrical part of the cask as the controlling datum was used. This axis was then intersected with the "Lid End" of the Cask and a point was constructed. Another point was measured at the 90 degree lifting lug to establish the other axis. This alignment was repeated for each measurement of the Cask.

The table below, *Table 1*, shows the maximum and minimum deviations of the profiles of the Cask when compared to its CAD model for each drop test. The maximum (positive) deviations indicate the profile of the Cask was larger than that of the model. Similarly, the minimum (negative) deviations indicate that the profile of the Cask was smaller than that of the model.

Table 1: Cask Assembly Pre- and Post- Drop Profile Deviations from CAD Model (inches)

Cask Condition	Pre End Drop	Post End Drop	Post Side Drop	Post Slap Down
Maximum Deviation	0.0068	0.0046	0.0053	0.0047
Minimum Deviation	-0.0094	-0.0101	-0.0109	-0.0105

Over the course of all three drop tests, the maximum deviations varied by a total of 0.0022 inches, while the minimum deviations varied by a total of 0.0015 inches. This indicates that the effect of the drop tests had a negligible impact on the profile of the Cask.

Below is a sample of the Cask profile from the Pre- End Drop scan. There are 2 pictures, *Image A* is the 0-180 Cross-Section of the Cask, and *Image B* is the 90-270 Cross-Section. The red areas represent the positive (maximum deviations) and the yellow areas represent the negative (minimum deviations).

EAST COAST METROLOGY
461 Boston Street ♦ Topsfield, Massachusetts 01983 ♦ Tel: 978-887-5781 ♦ Fax: 978-887-5782 ♦ www.EastCoastMetrology.com

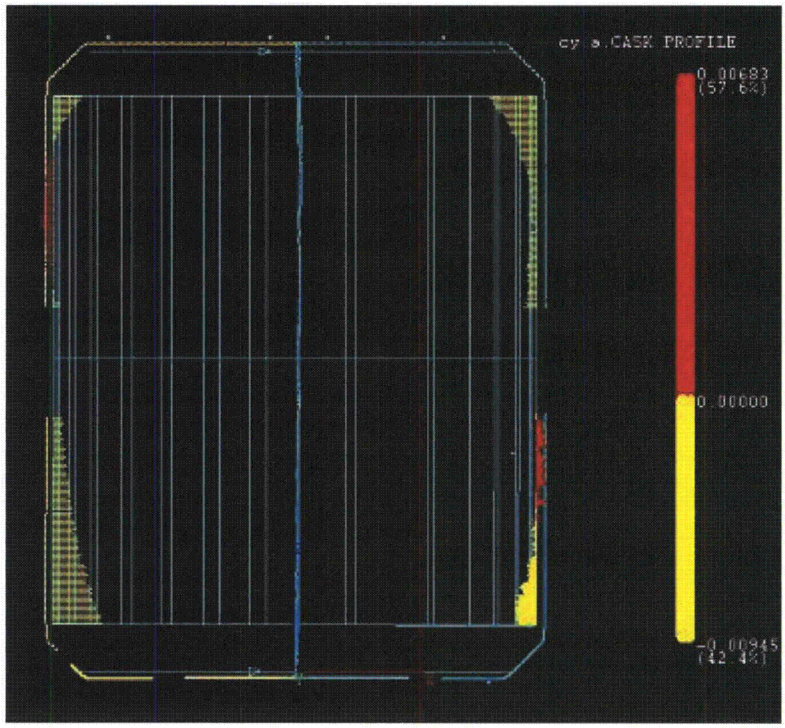

Image A: Cask Assembly Pre-End Drop Scan Data, 0-180 Degree Cross-Section

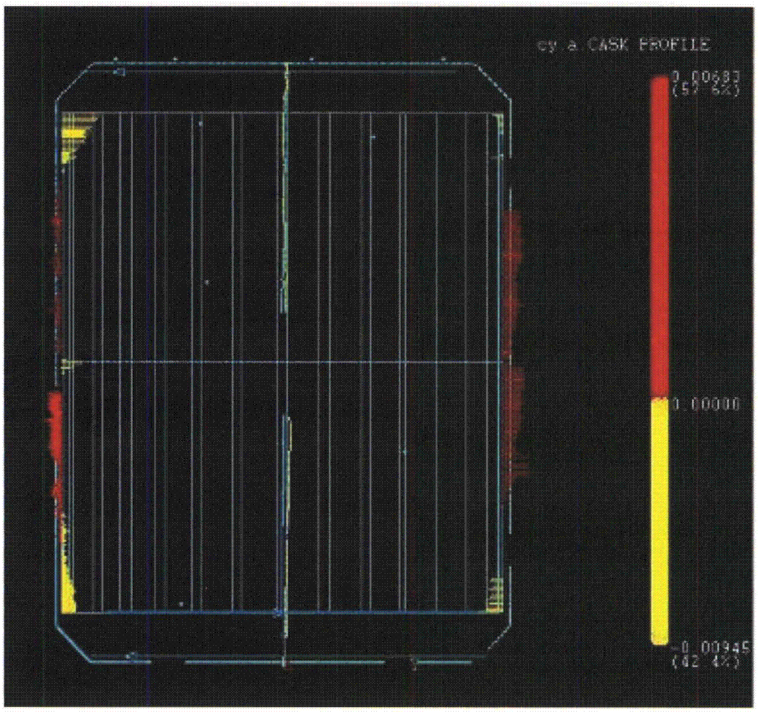

Image B: Cask Assembly Pre-End Drop Scan Data, 90-270 Degree Cross-Section

AOS-165 Cask Impact Limiter Assemblies:

For the Impact Limiters, scan data was taken at the 0, 30, 60, 90, 120, 150, 180, 210, 240, 270, 300 and 330 degree profiles. In order to compare each impact limiter in its pre- and post- drop condition, an alignment using the bottom perimeter (opposite the domed-end), measured as a circle, was used a reference. By measuring it as a circle, the center point and vector of the measured circle were established. The portions of this circle that were deformed due to each drop test were not used in this calculation. The vector of this axis was defined to be the primary datum in this alignment. A point was then measured at the 90 degree lifting lug to establish the second axis in the coordinate system. This process provided the only repeatable means to align each impact limiter and subsequently compare the results.

Once the pre- and post-drop scan data was collected for each Impact Limiter, the 90-270 degree profile cross-sections were overlaid in order to calculate the magnitude of deformation for each drop. In the images below, each Impact Limiter has been analyzed in this manner and the deformations reported. They are listed below in the same order that the drop tests occurred: End Drop (Impact Limiter 5), Side Drop (Impact Limiters 1 & 3) and Slap Down (Impact Limiters 2 & 4).

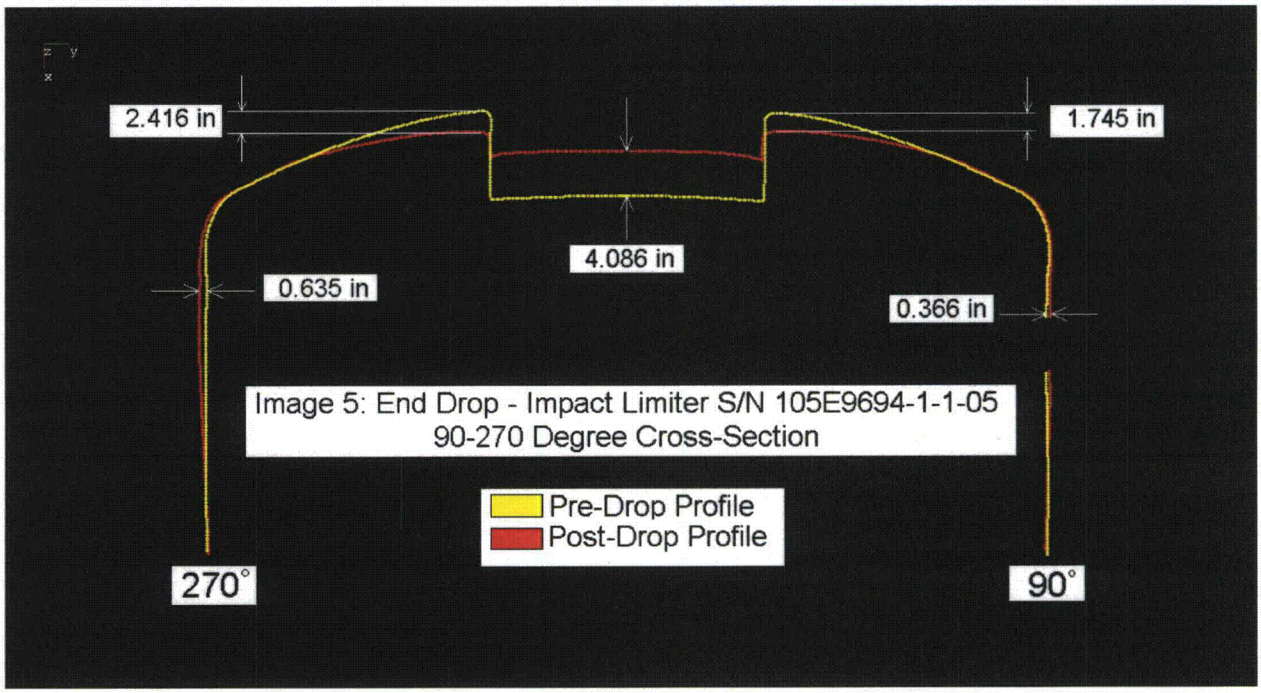

Image 5: Impact Limiter Serial No. 105E9694-1-1-05 - End Drop Cross-Section Overlay

EAST COAST METROLOGY
461 Boston Street ♦ Topsfield, Massachusetts 01983 ♦ Tel: 978-887-5781 ♦ Fax: 978-887-5782 ♦ www.EastCoastMetrology.com

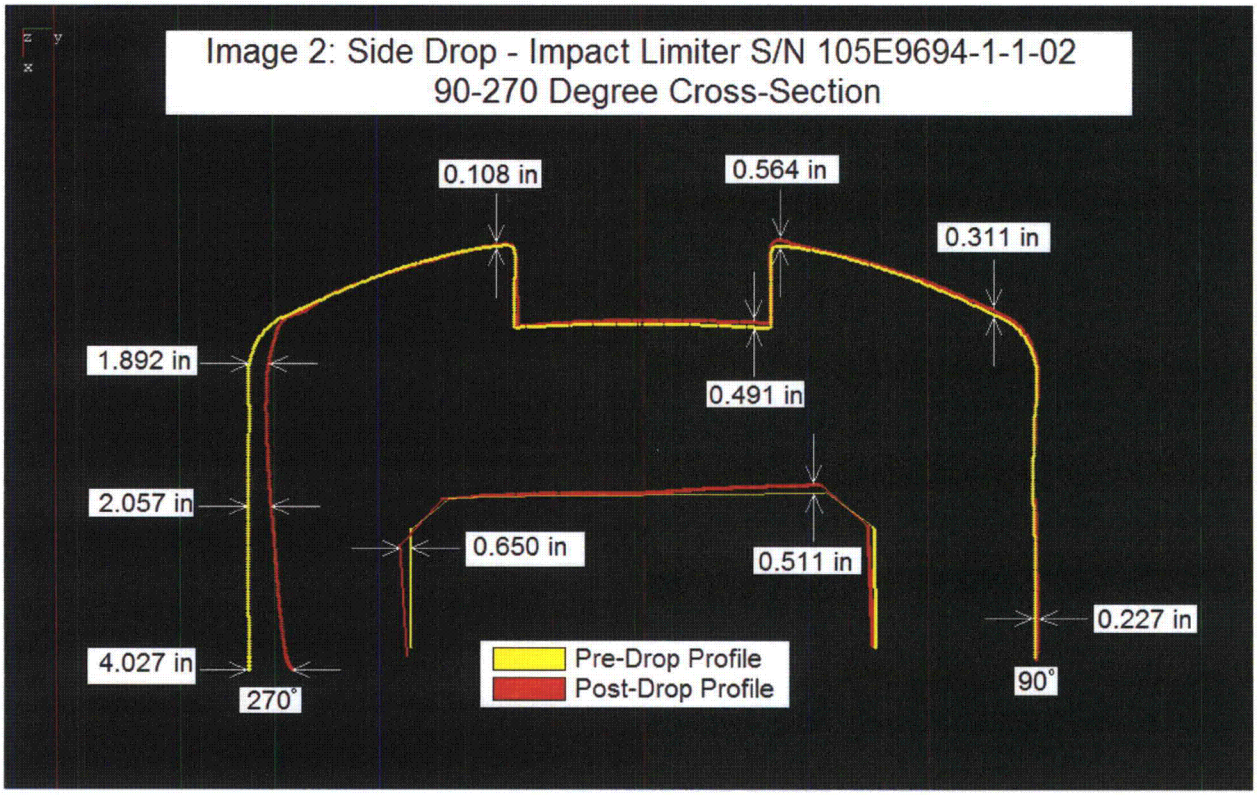

Image 2: Impact Limiter Serial No. 105E9694-1-1-02 - Side Drop Cross-Section Overlay

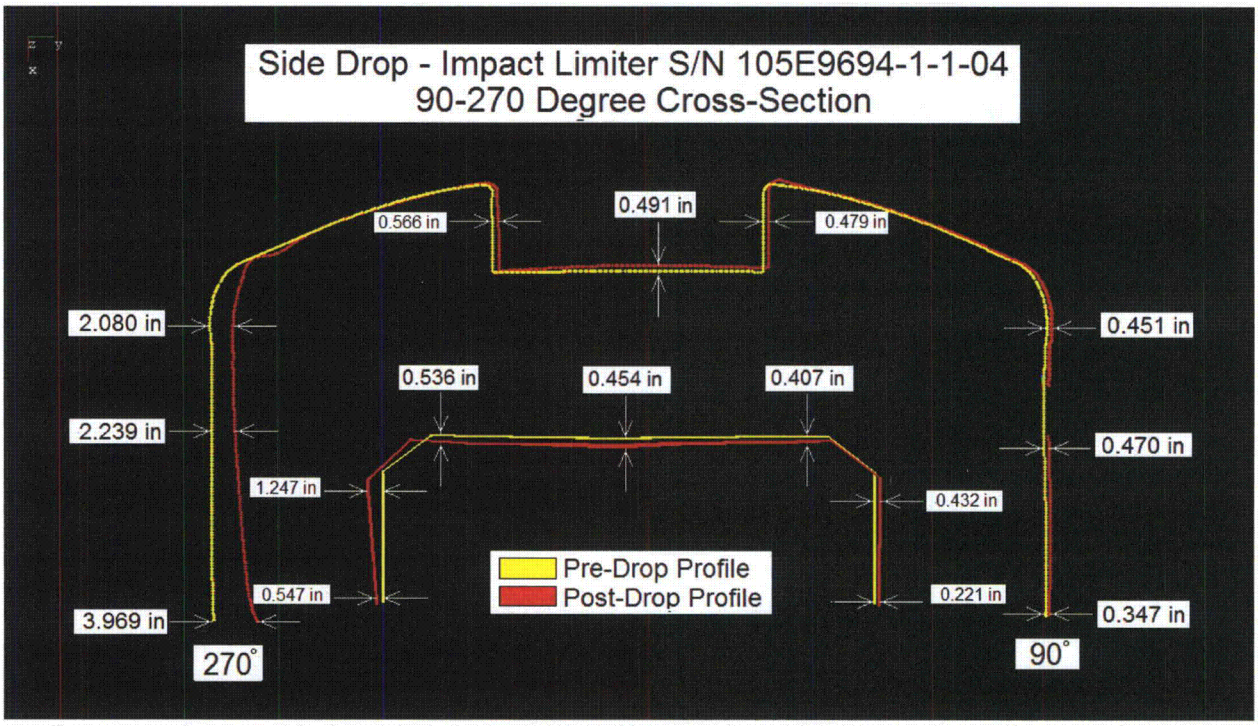

Image 4: Impact Limiter Serial No. 105E9694-1-1-04 - Side Drop Cross-Section Overlay

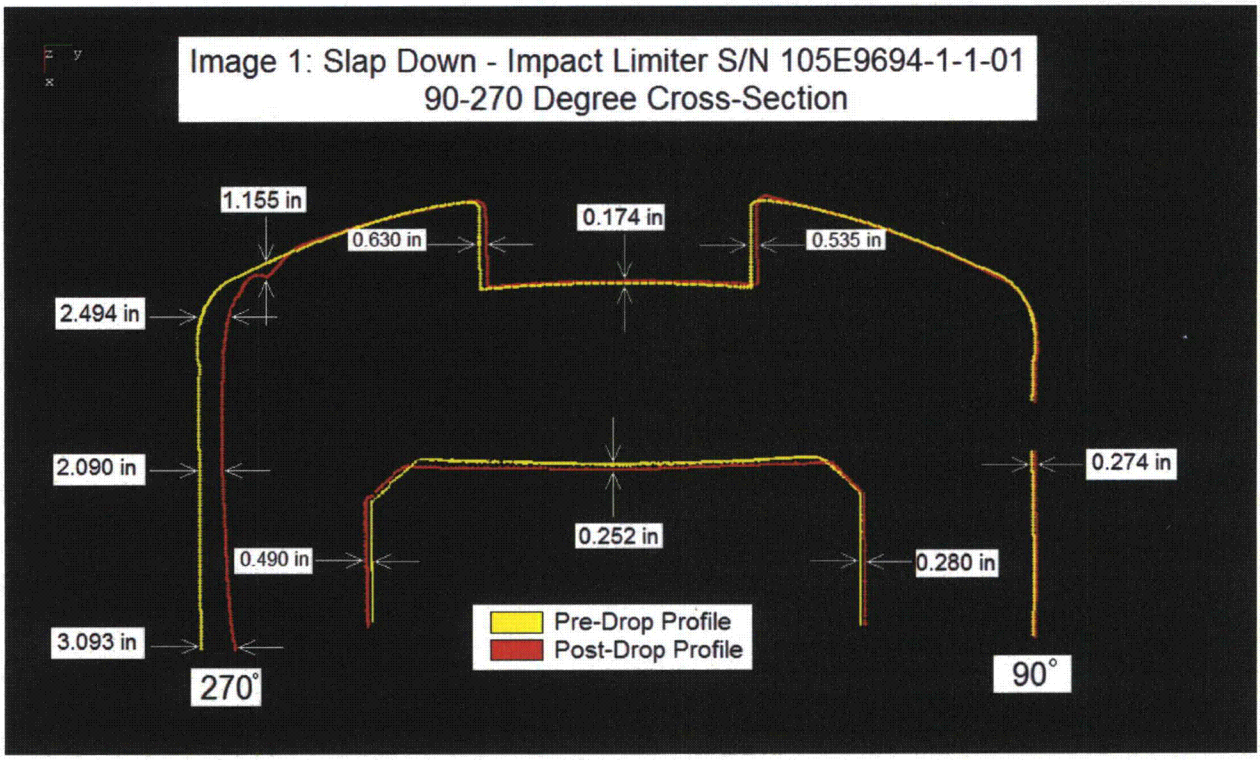

Image 1: Impact Limiter Serial No. 105E9694-1-1-01 - Slap Down Cross-Section Overlay

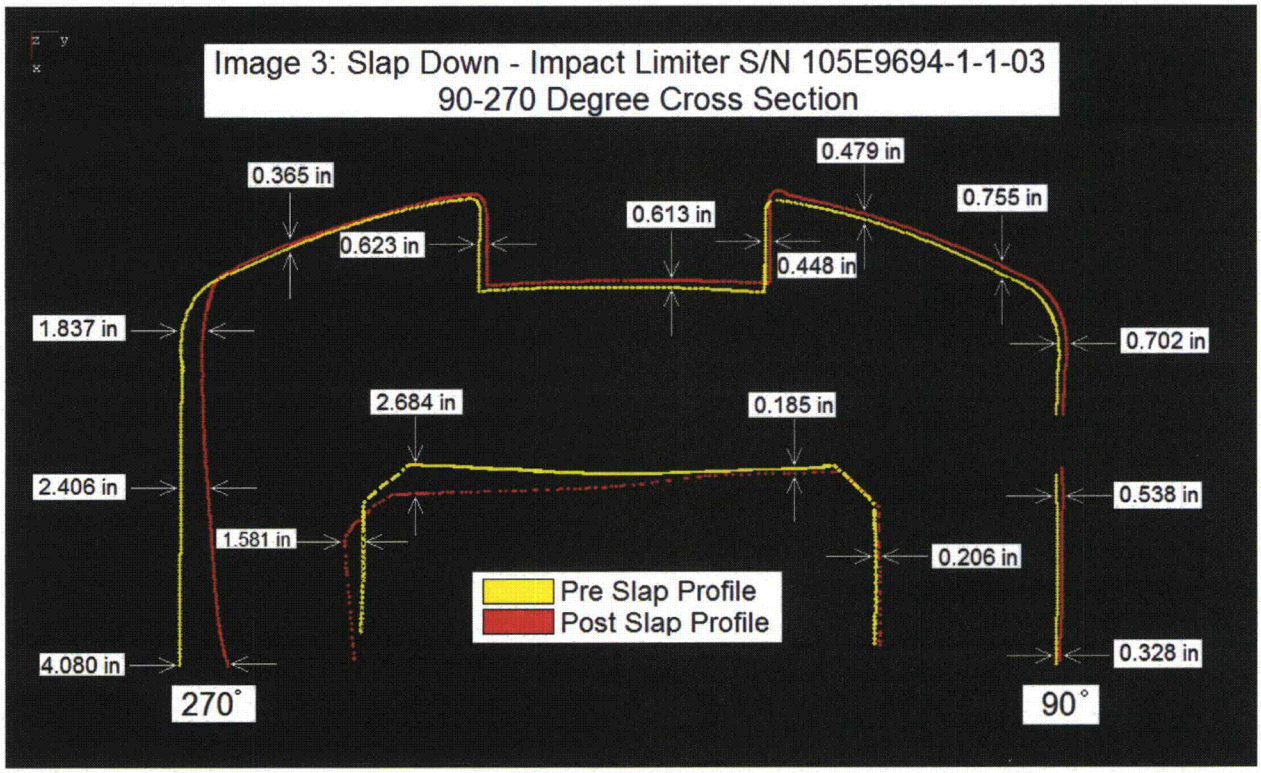

Image 3: Impact Limiter Serial No. 105E9694-1-1-03 - Slap Down Cross-Section Overlay

EAST COAST
METROLOGY

461 Boston Street ♦ Topsfield, Massachusetts 01983 ♦ Tel: 978-887-5781 ♦ Fax: 978-887-5782 ♦ www.EastCoastMetrology.com

Contact Information

As part of this report, *East Coast Metrology* appreciates the request for any additional information, which will help our customers find solutions to their measurement problems.

We proudly consider ourselves as allied partners to our customers, and can assist in the positioning and alignment of features, along with our ability to perform high accuracy measurements.

The key to our success is to be able to provide our customers with complete solutions, and the information that is most valuable to their cause, in a clear and concise manner.

We welcome any questions you may have, and look forward to working together in the near future.

Please feel free to contact us for additional information or concerns that may arise.

David K. Kramer
Project Engineer
East Coast Metrology
461 Boston Street (A4)
Topsfield, Massachusetts 01983
Tel: 503.997.7055
Fax: 603.251.5678
E-mail: dkramer@eastcoastmetrology.com

Attachments:
AOS-165 Cask Assembly Impact limiter, Serial No. 105E9694-1-1-01 Pre- and Post- Slap Down Scan Data (12 pgs)
AOS-165 Cask Assembly Impact limiter, Serial No. 105E9694-1-1-02 Pre- and Post- Side Drop Scan Data (10 pgs)
AOS-165 Cask Assembly Impact limiter, Serial No. 105E9694-1-1-03 Pre- and Post- Slap Down Scan Data (14 pgs)
AOS-165 Cask Assembly Impact limiter, Serial No. 105E9694-1-1-04 Pre- and Post- Side Drop Scan Data (12 pgs)
AOS-165 Cask Assembly Impact limiter, Serial No. 105E9694-1-1-05 Pre- and Post- Head Drop Scan Data (10 pgs)

THIS PAGE INTENTIONALLY LEFT BLANK

2.13 REFERENCES

[2.1] U.S. Nuclear Regulatory Commission (NRC), *Title 10, Code of Federal Regulations, Part 71 (10 CFR 71)*, "Packaging and Transportation of Radioactive Material."

[2.2] *International Atomic Energy Agency (IAEA) Safety Standards Series No. TS-R-1 (IAEA TS-R-1)*, "Regulations for the Safe Transport of Radioactive Material," 1996 Ed. (as amended 2003).

[2.3] U.S. Nuclear Regulatory Commission (NRC), *Regulatory Guide 7.6*, "Design Criteria for the Structural Analysis of Shipping Cask Containment Vessels," Rev. 1, 1978.

[2.4] U.S. Nuclear Regulatory Commission (NRC), *Regulatory Guide 7.8*, "Load Combinations for the Structural Analysis of Shipping Casks," Table 10, Rev. 1, 1989.

[2.5] Holman, W. R. and R. T. Langland, *NUREG/CR-1815, Recommendations for Protecting Against Failure by Brittle Fracture in Ferritic Steel Shipping Containers Up to Four Inches Thick*, Lawrence Livermore Laboratory, Prepared for U.S. Nuclear Regulatory Commission (NRC), Livermore, California, August, 1981.

[2.6] American Society of Mechanical Engineers, *ASME Boiler and Pressure Vessel Code*, Section II, Part D, 2004 Ed., No Addendum.

[2.7] Gerard, George, *Introduction to Structural Stability Theory*, McGraw-Hill, New York, 1962, Equation 8-14, p. 142, and pp 143-146.

[2.8] Kaminski, D. A., Ed., *Heat Transfer Data Book*, General Electric Company, New York, 1981, Section G515/29, p. 5.

[2.9] American Society of Mechanical Engineers, *ASME Boiler and Pressure Vessel Code*, Section II, Part D, Table 3, p. 406, 2004 Ed., No Addendum.

[2.10] D. Perry, *Aircraft Structures*, McGraw-Hill, 1950, pp. 398-400.

[2.11] Metech Welded Mesh, Inc., Online Catalog, accessed June, 2010, http://www.weldedwiremesh.net/.

[2.12] American National Standards Institute, *ANSI N14.5-1997*, "Radioactive Materials – Leakage Tests on Packages for Shipment," February 5, 1998.

[2.13] MIL-STD-883B(3) NOT 2, "Dissimilar Metals," May, 1993.

[2.14] General Plastics Manufacturing Company, *General Plastics LAST-A-FOAM FR-3700 for Crash & Fire Protection of Nuclear Material Shipping Containers*, Tacoma, WA, October, 2003.

[2.15] General Plastics Manufacturing Company, *Design Guide for Use of LAST-A-FOAM FR-3700 for Crash & Fire Protection of Nuclear Material Shipping Containers*, Washington, March, 1998 (revised October, 2003).

[2.16] ASME, Section III, Division 1, Appendices, Figure I-9.4, "Design Fatigue Curves for High Strength Steel Bolting for Temperatures Not Exceeding 700°F," 2004 Ed., No Addendum.

[2.17] Caldwell, S.G., Ph.D., *Tungsten Heavy Alloy Engineering Manual*, ATI Firth Sterling, AL, v4.0.

[2.18] Gibson, Lorna, J. and Michael F. Ashby, *Cellular Solids*, p. 193, Cambridge University Press, New York, NY, 2001.

[2.19] Torrey Hills Technology, LLC, *High Density Tungsten Technical Data*, accessed September 19, 2010, http://www.torreyhillstech.com/hddata.html.

[2.20] Lassner, Erik and Wolf-Dieter Schubert, *Tungsten – Properties, Chemistry, Technology of the Element, Alloys, and Chemical Compounds*, Kluwer Academic/Plenum Publishers, New York, NY, 1999.

[2.21] General Plastics Manufacturing Company, *Interactive Data Sheets*, accessed September 17, 2010, http://www.generalplastics.com/products/idatasheets.php?pfoamname=FR-3700. (Once on the Web page, enter the desired density and the Web site will generate the data sheet.)

[2.22] Communication from ATI Firth Sterling to Alpha-Omega Services, Inc., and GE Energy.

[2.23] Parker O-Ring Division, *Evaluation of Parker Compound S1224-70 to ASTM D2000 7GE705 A19 B37 EA14 EO16 E036 F19 G11 Compound Data Sheet*, Kentucky, June 19, 1996.

[2.24] Fitzroy, Nancy D., Ed., *Heat Transfer Data Book*, General Electric Company, New York, November, 1970 Edition, Section G502.5, p. 7.

[2.25] Touloukian, Y. S., *Thermophysical Properties of Matter, Metallic Elements and Alloys*, 1971.